Astrophysical Signatures of Axion-Like Particles

Francesca Day

Magdalen College

University of Oxford

A thesis submitted for the degree of

Doctor of Philosophy

Trinity 2017

Acknowledgements

First and foremost I thank my supervisor Joe Conlon for his excellent advice and guidance over the past four years, and for his comments on this thesis. I have had interesting and fruitful discussions with too many colleagues to list, but I would like to particularly thank Pedro Alvarez, Stephen Angus, Marcus Berg, James Bonifacio, Esra Bulbul, Malcolm Fairbairn, Pedro Ferreira, Isabel Garcia Garcia, Edward Hughes, Nicholas Jennings, Sven Krippendorf, John March-Russell, David J E Marsh, M C David Marsh, Francesco Muia, Andrew Powell, Stefano Profumo and Markus Rummel. I further thank James Bonifacio for detailed reading of and comments on this thesis. I am funded by an STFC studentship and by Joe Conlon's ERC grant.

This work would not have been possible without the support of my friends and family. Particular thanks go to Ottoline, Joshua, Henrietta, Rosie and Chris. Finally and most importantly, I remember Stephen Day, who will always remain my best friend and greatest teacher.

Statement of Originality

This thesis is wholly my own work, except as indicated in the text. I now summarise my contribution to work done in collaboration. Chapter 1 contains introductory material written solely by me. Chapter 2 is based on [1] and [2] written in collaboration with Marcus Berg, Joseph Conlon, Nicholas Jennings, Sven Krippendorf, Andrew Powell and Markus Rummel. The X-ray data analysis was performed and checked collaboratively by all authors. I devised and coded the bounds setting procedure. Chapter 3 is based on [3], of which I am the sole author. Chapter 4 is based on [4], written in collaboration with Joseph Conlon. I wrote the simulations for this paper, and Joe independently checked most of the results. Section 4.5 is based on material from [5], written in collaboration with Pedro Alvarez, Joseph Conlon, David Marsh and Markus Rummel. The simulations presented in this section are entirely my own work. Chapter 5 is based on [6] written in collaboration with Joseph Conlon, Nicholas Jennings, Sven Krippendorf and Markus Rummel. The calculations in this chapter were performed and checked collaboratively by all authors. Chapter 6 contains concluding material written entirely by me. No part of this thesis has been submitted for any other qualification.

Abstract

The Standard Model of particle physics has enjoyed unprecedented success in predicting experimental results. However, evidence from astrophysical observations points to the existence of a dark sector of particles that interact only very weakly with the Standard Model. In this work, we search for dark sector signatures in X-ray telescope data. Much of this work concerns a class of hypothetical particles, the axion-like particle (ALP). ALPs are a theoretically well-motivated extension of the Standard Model. If ALPs exist, they may lead to intriguing astrophysical signatures: in the presence of a background magnetic field, ALPs and photons can interconvert. We could detect ALPs by searching for photon to ALP conversion. For example, photons produced by point sources in or behind galaxy clusters may convert to ALPs in the cluster's magnetic field. This could lead to observable spectral anomalies. Using this strategy, we place world leading bounds on the ALP-photon coupling.

One potential signal of dark matter is an anomalous line in the spectra of galaxies and galaxy clusters. In 2014, an anomalous line was found at an energy of 3.5 keV. The nature and cause of this line is still under discussion. We analyse a scenario in which the 3.5 keV line arises from dark matter decay to ALPs, which interconvert with 3.5 keV photons in astrophysical magnetic fields. We further report an anomalous deficit at 3.5 keV in the spectrum of the Active Galactic Nucleus at the centre of the Perseus galaxy cluster. This motivates the study of a new model in which both features are caused by fluorescent dark matter which resonantly interacts with 3.5 keV photons. We analyse observations of Perseus at 3.5 keV to date, and show that they are well explained by this model. Further theoretical and experimental work is needed to discover or exclude fundamental physics effects in X-ray spectra.

Contents

Chapter 1

Introduction

The Standard Model (SM) of particle physics has successfully predicted the results of almost every ground-based experiment. In particular, the Large Hadron Collider has found no evidence for physics Beyond the Standard Model (BSM). This places strong constraints on BSM models that interact with the Standard Model.

The Standard Model describes three generations of fermions inhabiting representations of the SM gauge group $SU(3) \times SU(2) \times U(1)_Y$, as well as the corresponding gauge bosons and the Higgs boson. The six quarks occupy the fundamental representation of $SU(3)$, leading to strong force interactions between them. Strong interactions are mediated by the $SU(3)$ gauge bosons, the gluons. The strong force is believed to lead to quark confinement - only $SU(3)$ singlet bound states (hadrons) of quarks have ever been observed. The spectrum of hadrons is consistent with the six quarks of the SM. Furthermore, in high energy collisions hadronic jets are observed in the final state. These originate from quarks produced in the collision, which subsequently hadronise. A key piece of evidence for the $SU(3)$ gauge symmetry was the discovery of three jet final states in e^+e^- collisions at PETRA [7, 8]. These arise when a quark produced in the collision radiates a gluon, leading to a gluon jet. The angular distribution of these jets was later used to verify that the gluon is a vector particle [9, 10].

Further evidence that quarks are charged under three possible colours is provided

by measurements of $R = \frac{\sigma(e^+e^- \to \text{hadrons})}{\sigma(e^+e^- \to \mu^+\mu^-)}$. As leptons are singlets under $SU(3)$, quark final states have an additional factor of the number of colours, N_c, in their density of states. We therefore expect $R \simeq N_c \Sigma_q Q_q^2$, where Q_q are the charges of all kinematically accessible quarks. This is confirmed by results at e^+e^- colliders [11]. Another key property of an unbroken gauge symmetry in four dimensions is that the corresponding gauge bosons are exactly massless. The photon and gluon masses are experimentally bounded to lie below 10^{-18} eV and 1 MeV respectively [11]. Furthermore, we require for a consistent theory that gauge symmetries are not anomalous. This is satisfied in the Standard Model by cancellation of the gauge anomalies within each generation.

The Standard Model's $SU(2) \times U(1)_Y$ gauge symmetry is spontaneously broken to $U(1)_{\text{EM}}$, describing electromagnetism, by the vacuum expectation value (vev) of the Higgs field. This gives a mass to three of the electroweak gauge bosons, the $W^\pm$ and Z bosons. The symmetry breaking pattern is described by the weak mixing angle $\sin\theta_W = \frac{g'}{\sqrt{g^2+g'^2}}$, where g and g' are the $SU(2)$ and $U(1)_Y$ coupling constants respectively. The masses of the $W^\pm$ and Z bosons are also related by $\frac{m_W}{m_Z} = \cos\theta_W$. The massive gauge bosons were discovered at CERN in 1983, and their mass ratio is as predicted by the electroweak theory [12–15]. The structure of electroweak symmetry breaking also implies the absence of tree level flavour changing neutral currents, imposing strong constraints on allowed BSM physics.

The Z boson couples at tree level to every SM fermion. Its decay width therefore receives contributions from every fermion charged under the SM gauge group and lighter than m_Z. Measurements of the Z peak confirm that there are only 3 generations of SM particles lighter than m_Z. In particular, the width of the Z boson peak confirms that there are exactly three generations of light left-handed neutrinos [16].

The Higgs vev generates a mass term for the SM fermions. Left-handed fermions

inhabit the fundamental representation of the $SU(2)$ gauge symmetry, while right-handed fermions are $SU(2)$ singlets. Therefore a fundamental Dirac mass term would violate the gauge symmetry, and so the Higgs mechanism is required to produce the observed masses. The discovery of the Higgs boson at the Large Hadron Collider in 2012 completed the experimental confirmation of the SM particles [17, 18].

Despite its many successes, the Standard Model fails unequivocally in describing results from astrophysics. In particular, it contains no viable candidate for dark matter - matter inferred to exist from observing its myriad gravitational effects, but so far not observed in any other way. Observations of the anisotropies of the Cosmic Microwave Background [19], of the velocities of stars in galaxies [20, 21] and galaxies in galaxy clusters [22, 23], and of gravitational lensing [24, 25] are most straightforwardly explained by an additional degree of freedom that redshifts like matter and that interacts only weakly with the Standard Model. These requirements allow scope for a vast range of dark matter models. The most popular candidates include Weakly Interacting Massive Particles (WIMPs) found in supersymmetric models [26], and the axions or axion-like particles described in this thesis [27, 28]. Numerous searches to detect non-gravitational interactions of dark matter through its scattering off [29] or annihilation to [30] Standard Model particles, or through its direct production in particle colliders [31, 32] have returned null results. Furthermore, the accelerating expansion of the universe suggests the existence of an additional dark energy component, making up $\sim 70\%$ of the universe's energy content [19, 33]. More broadly, we may consider a dark sector of particles that interact only very weakly with the Standard Model. In this thesis, we use astrophysical observations to further efforts to search for signatures from the dark sector.

The overwhelming evidence for BSM physics in the form of dark matter and dark energy is currently entirely derived from their gravitational interactions. As-

trophysical observations allow us probe sufficiently large distances to observe the gravitational effects of the dark sector. It is also well-motivated to search for further, non-gravitational evidence for new physics in the extreme conditions provided by astrophysical systems as well as in particle colliders on Earth. In this thesis, we search for evidence of axion-like particles (ALPs). As described below, ALPs are well motivated extensions of the Standard Model, in particular arising in string theory and providing a dark matter candidate. Furthermore, ALPs and photons interconvert in an external magnetic field, providing a wide range of astrophysical phenomenology to search for ALPs and place bounds on the ALP parameter space.

1.1 Axion-Like Particles

1.1.1 Motivations

The QCD axion arises as a solution to the strong CP problem. The CP violating term

$$\mathcal{L} \supset \theta \frac{g^2}{32\pi^2} G^{\mu\nu} \tilde{G}_{\mu\nu}, \tag{1.1}$$

is permitted by the symmetries of the Standard Model. $G^{\mu\nu}$ is the gluon field strength tensor and g the strong coupling constant. The dual field strength tensor is given by $\tilde{G}_{\mu\nu} = \frac{1}{2}\epsilon_{\mu\nu\rho\sigma}G^{\rho\sigma}$ and we trace over colour indices. However, null measurements of the neutron electric dipole moment constrain $\theta \lesssim 10^{-10}$ [11]. Furthermore, weak interactions modify the CP violating parameter as $\theta \to \theta + \arg\det M$, where M is the quark Yukawa matrix. We would therefore require precise cancellations between seemingly unrelated Standard Model parameters to explain the small observed value of θ in the absence of new physics.

A solution to the strong CP problem is provided by the Vafa-Witten Theorem: in parity-conserving vector-like theories such as QCD, parity conservation is not sponta-

neously broken [34]. Equivalently, in such theories, dynamical parity violating terms have zero vacuum expectation value. We may therefore solve the strong CP problem if we promote the total CP violating parameter (which is also P violating) to a dynamical variable:

$$\mathcal{L} \supset (\theta + \frac{\xi a}{f_a}) \frac{g^2}{32\pi^2} G^{\mu\nu} \tilde{G}_{\mu\nu}, \tag{1.2}$$

where a is the QCD axion field, f_a is a dimension one constant and ξ is a dimensionless constant [35]. With this addition, the Vafa-Witten Theorem guarantees that the total CP violating term is zero in the ground state. A potential is generated for the axion such that the total coefficient of $G^{\mu\nu}\tilde{G}_{\mu\nu}$ is zero at the potential minimum. Strictly speaking, the Vafa-Witten theorem cannot be fully applied to the strong CP problem, as the left handed quarks are also charged under the weak interaction, which is not vector-like. Indeed, $SU(2)$ instantons lead to a very small shift in the minimum of the axion potential away from the CP conserving value [36].

The θ term arises because the global $U(1)_A$ symmetry in QCD is anomalous (the chiral anomaly). To make θ dynamical, we introduce an additional global chiral symmetry $U(1)_{PQ}$, which is spontaneously broken. The axion is the Goldstone boson of $U(1)_{PQ}$. The QCD chiral anomaly causes a non-perturbative explicit breaking of $U(1)_{PQ}$, generating a potential for the axion. The axion is therefore a naturally light pseudo-Goldstone boson.

In this work I consider more general axion-like particles (ALPs), arising in extensions of the Standard Model as pseudo-Goldstone bosons of chiral $U(1)$ symmetries. As in the case of the QCD axion, the global $U(1)$ symmetry is both spontaneously broken and explicitly broken by non-perturbative effects. An ALP is a naturally light pseudo-scalar singlet under the Standard Model gauge group. In a theory with multiple ALP fields, I will assume that we may express these fields in a basis such that there

is one QCD axion, and the other ALPs have no tree level coupling to gluons. This work instead considers the phenomenology of the ALP coupling to electromagnetism:

$$\mathcal{L} \supset \frac{a}{4M} F^{\mu\nu} \tilde{F}_{\mu\nu}, \tag{1.3}$$

where $F^{\mu\nu}$ is the electromagnetic field strength tensor and $\tilde{F}_{\mu\nu} = \frac{1}{2}\epsilon_{\mu\nu\rho\sigma}F^{\rho\sigma}$ is its dual. This term leads to ALP-photon interconversion in the presence of a background magnetic field, providing a potential window to observing ALPs. Although not required to solve the strong CP problem, ALPs are well motivated in string theory models. String compactifications typically give rise to many ALP fields, populating many decades in mass [37]. Furthermore, ALPs can act as both dark matter and dark energy, depending on their mass.

1.1.2 ALP cosmology

As the Goldstone boson of a $U(1)$ symmetry, the ALP represents a complex phase, and so retains a discrete shift symmetry $a \to a + 2\pi f_a$ even after explicit breaking. The ALP potential takes the form:

$$V(a) = \Lambda_a^4 \left(1 - \cos\left(\frac{a}{f_a}\right)\right), \tag{1.4}$$

where the scales f_a and Λ_a are model dependent. For string axions, f_a typically takes a value near the GUT scale, $f_a \sim 10^{16}$ GeV. However, f_a may also be several orders of magnitude smaller in some models [38]. The value of Λ_a is typically $\Lambda_a^4 \sim m_{\mathrm{SUSY}}^2 M_{\mathrm{pl}}^2 \mathrm{e}^{-S}$ [39], where m_{SUSY} and M_{pl} are the supersymmetry breaking and Planck scales respectively, and S is the action of the relevant non-perturbative effects. For example, a string axion that solves the strong CP problem requires $S \gtrsim 200$ [39]. We note that Λ_a is exponentially sensitive to S, and so may take a very large range of

values.

To first order in $\frac{1}{f_a}$, $V(a)$ represents a mass term for the ALP:

$$V(a) \simeq \frac{\Lambda_a^4}{2f_a^2}a^2 = \frac{1}{2}m_a^2 a^2. \tag{1.5}$$

In a generic ALP model, the mass m_a and coupling to electromagnetism $1/M$ are independent.

Cold ALPs may be produced in the early universe through misalignment production. After the corresponding $U(1)$ is spontaneously broken, but before it is non-perturbatively broken, the ALP field is massless. After non-perturbative breaking, the field is displaced from its minimum and follows the classical equation of motion:

$$\ddot{a} + 3H\dot{a} + m_a^2 a = 0, \tag{1.6}$$

where H is the Hubble parameter and we have assumed an FLRW background. For $m_a \gg H$, the ALP field performs damped coherent oscillations about its potential minimum. In an FRW cosmology, the energy density ρ_z in these oscillations redshifts as $\rho_z \propto R^{-3}$, where R is the scale factor, and so the oscillations act as dark matter. If non-perturbative breaking occurs after inflation, topological defects between patches of different initial field value are also relevant. The decay of these defects is a further source of non-relativistic ALPs that contribute to dark matter. For $m_a \ll H$, the ALP field is overdamped by the expansion of the universe, and instead acts as quintessent dark energy, with an energy density that changes very slowly compared to the Hubble time. ALP cosmology is reviewed in [28]. In this thesis I consider instead ALPs produced by the decay of heavy particles or by photon to axion conversion. Such ALPs are relativistic and so act as dark radiation. Dark radiation is not required to explain current observations, but a dark radiation component is also

not ruled out.

1.1.3 ALP-photon interconversion

We expect non-renormalizable couplings between the ALP and the Standard Model suppressed by some high scale M. In this thesis I explore the phenomenology of the dimension five $a\gamma\gamma$ coupling. The parity violating term $\mathcal{L} \supset \frac{1}{4M'} a F_{\mu\nu} F^{\mu\nu}$ is heavily constrained by equivalence principle tests [40]. We therefore focus on the parity conserving interaction $\mathcal{L} \supset \frac{1}{4M} a F_{\mu\nu} \tilde{F}^{\mu\nu}$, which leads to ALP-photon interconversion in a background magnetic field [41]. In particular, I will consider this process in astrophysical environments.

The Lagrangian describing this ALP-photon interaction is:

$$\mathcal{L}_{\mathrm{ALP}} = \frac{1}{2}\partial_\mu a \partial^\mu a - \frac{1}{2} m_a^2 a^2 - \frac{1}{4} F_{\mu\nu} F^{\mu\nu} + \frac{1}{4M} a F_{\mu\nu} \tilde{F}^{\mu\nu}, \tag{1.7}$$

where we have used the mostly minus metric convention. The ALP-photon coupling is suppressed by an energy scale M much larger than the physical energies involved. It is therefore sufficient to simulate ALP-photon conversion using the classical equation of motion derived from equation (1.7), and neglecting higher dimension terms. We will now derive the linearised equation of motion for the ALP-photon interaction in an external magnetic field B_0. We roughly follow the treatment in [42], although we use a different normalisation for M. Varying with respect to the ALP field, we obtain the Euler-Lagrange equation:

$$(\Box + m_a^2) a = \frac{1}{4M} F_{\mu\nu} \tilde{F}^{\mu\nu} = \frac{1}{M} \mathbf{E} \cdot \mathbf{B}. \tag{1.8}$$

We introduce the spatial orthonormal basis vectors $\mathbf{e}_1 = \frac{\mathbf{B}_{0,n}}{B_{0,n}}$, $\mathbf{e}_2$, $\mathbf{e}_3 = \frac{\mathbf{k}}{k}$, where $\mathbf{k}$ is the direction of travel of the ALP/photon, $\mathbf{B}_{0,n}$ is the component of the external

magnetic field perpendicular to $\mathbf{k}$ and $\mathbf{e}_2$ is defined by orthonormality. We consider a flux of particles of energy ω. We use Lorenz gauge for the photon's vector potential, choosing $\mathbf{A}_\gamma = i(A_\parallel(z), A_\perp(z), 0)\mathrm{e}^{i\omega t}$, with the scalar potential $\phi = 0$, where z parameterises the direction of travel of the ALP or photon. The corresponding electric field is $\mathbf{E} = \omega(A_\parallel, A_\perp, 0)\mathrm{e}^{i\omega t}$. Neglecting the magnetic field associated with the photon flux, we have $\mathbf{E}\cdot\mathbf{B} = B_{0,n}A_\parallel\omega\mathrm{e}^{i\omega t}$. Equation 1.8 therefore becomes

$$(\Box + m_a^2)a = \frac{B_{0,n}A_\parallel}{M}\omega\mathrm{e}^{i\omega t}. \tag{1.9}$$

Varying with respect to the four-vector potential we obtain:

$$\partial_\mu F^{\mu\nu} = \frac{a}{M}\partial_\mu\tilde{F}^{\mu\nu} + \frac{\partial_\mu a}{M}\tilde{F}^{\mu\nu} \tag{1.10}$$

We first note that $\partial_\mu\tilde{F}^{\mu\nu} = 0$ by symmetry. The four-vector potential A is the sum of that of the background magnetic field and that of the photon travelling through it: $A = A_b + A_\gamma$, where A_γ is defined above. We treat the ALP and photon fields as a perturbation on the background magnetic field. We therefore require that the background field alone satisfies the equation of motion: $\partial_\mu F_b^{\mu\nu} = 0$. Neglecting terms that are 2nd order in the ALP and photon fields, we obtain:

$$\Box A_\gamma^\nu - \partial^\nu\partial_\mu A_\gamma^\mu = \frac{\partial_\mu a}{M}\tilde{F}_b^{\mu\nu} \tag{1.11}$$

By the Lorenz gauge condition, $\partial_\mu A_\gamma^\mu = 0$. There are only two non-zero components of A_γ^ν to consider: $\nu = 1$, parallel to $\mathbf{B}_{0,n}$, and $\nu = 2$, perpendicular to $\mathbf{B}_{0,n}$. We neglect any variation of a perpendicular to the direction of travel, and take $\partial_t a = i\omega a$ to conclude:

$$\Box(A_{\parallel}(z)\mathrm{e}^{i\omega t}) = \frac{B_{0,n}}{M}\omega a, \tag{1.12}$$

$$\Box(A_{\perp}(z)\mathrm{e}^{i\omega t}) = 0, \tag{1.13}$$

where $\parallel$ and $\perp$ are the polarizations parallel and perpendicular to $\mathbf{B}_{0,n}$, and we have assumed $\mathbf{B}_{0,n}$ varies slowly compared to ω.

We neglect any variation of a and $\mathbf{A}$ perpendicular to the direction of travel, such that $\Box a = -(\omega^2 + \partial_z^2)a$, and similarly for $\mathbf{A}$. We now assume that the ALP/photon wavelength is much shorter than the scale over which its environment changes. This condition is abundantly satisfied for X-ray energy ALPs in astrophysical environments, as considered in this thesis. We may then perform a WKB approximation $\omega^2 + \partial_z^2 \simeq (\omega + k)(\omega - i\partial_z) \simeq 2\omega(\omega - i\partial_z)$, assuming a near-vacuum dispersion relation and a relativistic axion.

The ALP-photon equations of motion are conveniently described by combining the ALP with the two photon polarizations in an ALP-photon vector. Substituting our WKB approximation into equations 1.9 and 1.12, we obtain:

$$\left(\omega + \begin{pmatrix} \Delta_\gamma & 0 & 0 \\ 0 & \Delta_\gamma & \Delta_{\gamma a} \\ 0 & \Delta_{\gamma a} & \Delta_a \end{pmatrix} - i\partial_z\right)\begin{pmatrix} \mid A_\perp\rangle \\ \mid A_\parallel\rangle \\ \mid a\rangle \end{pmatrix} = 0, \tag{1.14}$$

where $\Delta_{\gamma a} = \frac{B_{0,n}}{2M}$ and $\Delta_a = \frac{-m_a^2}{2\omega}$. We have also introduced a photon mass term.The photon components are given an effective mass by their interactions with free electrons in the surrounding medium. This effective photon mass is equal to the plasma frequency - the frequency of charge density oscillations in the surrounding plasma. This is given by $\omega_{pl} = \left(4\pi\alpha\frac{n_e}{m_e}\right)^{\frac{1}{2}}$, where n_e is the free electron density. We then have:

$$\Delta_\gamma = \frac{-\omega_{pl}^2}{2\omega} = -\frac{4\pi\alpha n_e}{2\omega m_e}. \tag{1.15}$$

We also note that we have neglected Faraday rotation between the two photon polarizations. All the results we consider are insensitive to photon polarization, and so this term is not relevant. Furthermore, the magnitude of Faraday rotation is proportional to λ^2, and is negligible at X-ray energies. On the other hand, it is important to note that only the magnetic field component perpendicular to the ALP/photon flux leads to mixing between the ALP and photon components. For the remainder of this work, we will neglect the ALP mass and take $m_a = 0$. This will be valid for $m_a \lesssim 10^{-12}\,\text{eV}$, such that the ALP is lighter than the effective photon mass in galaxies and galaxy clusters. This simplification in particular neglects resonant effects that may occur when $m_a = \omega_{pl}$ for some region on the ALP/photon's path [41].

When considering ALP to photon conversion, we do not measure the photon polarization and so we simply add the conversion probabilities for each polarization. For example, for an initially pure ALP state, the probability of observing a photon after a distance L is:

$$P_{a\to\gamma}(L) = |\,\langle 1,0,0|f(L)\rangle\,|^2 + |\,\langle 0,1,0|f(L)\rangle\,|^2, \tag{1.16}$$

where $|f(L)\rangle$ is the final state after a distance L as determined by equation (1.14). The ALP to photon conversion probability $P_{a\to\gamma}$ is proportional to $\frac{B_{0,n}^2}{M^2}$ in the limit $\frac{B_{0,n}}{M} \ll 1$. A non-zero electron density in the propagation environment gives an effective mass to the photon, causing decoherence between the ALP and photon components and hence suppressing $P_{a\to\gamma}$.

For constant electron density and magnetic field, there is an analytic solution for

the conversion probability. We identify two angles associated with the propagation:

$$\tan(2\theta) = 2.8 \times 10^{-3} \times \left(\frac{10^{-3}\,\mathrm{cm}^{-3}}{n_e}\right)\left(\frac{B_{0,n}}{1\,\mu\mathrm{G}}\right)\left(\frac{\omega}{1\,\mathrm{keV}}\right)\left(\frac{10^{13}\,\mathrm{GeV}}{M}\right), \quad (1.17)$$

$$\Delta = 0.053 \times \left(\frac{n_e}{10^{-3}\,\mathrm{cm}^{-3}}\right)\left(\frac{1\,\mathrm{keV}}{\omega}\right)\left(\frac{L}{1\,\mathrm{kpc}}\right). \quad (1.18)$$

For a single domain of length L, the conversion probability is then

$$P(a \to \gamma) = \sin^2(2\theta)\sin^2\left(\frac{\Delta}{\cos 2\theta}\right). \quad (1.19)$$

In a more general case, for $P_{a\to\gamma} \ll 1$, we find:

$$P_{a\to\gamma}(L) = \left|\int_0^L dz e^{i\varphi(z)}\Delta_{\gamma a}(z)\right|^2, \quad (1.20)$$

where,

$$\varphi(z) = \int_0^z dz'\Delta_\gamma(z') = -\frac{1}{2\omega}\int_0^z dz'\omega_{pl}^2(z'). \quad (1.21)$$

As shown in equation (1.15), $\Delta_\gamma(z) \propto n_e$, and so the electron density has the effect of rotating the probability amplitudes $\langle 1,0,0|f(L)\rangle$ and $\langle 0,1,0|f(L)\rangle$ in the complex plane as L increases, suppressing the efficacy of the magnetic field in increasing the conversion probability over increasing distances. Analogous results apply to photon to ALP conversion.

Some astrophysical environments, such as the Milky Way, are almost opaque to low energy X-rays due to photoelectric absorption from the warm neutral medium. We capture this effect in our equation of motion for the ALP-photon vector by including a damping parameter $\Gamma(z)$ that describes the attenuation of the photon components. The new equation of motion no longer describes a closed quantum system - the Hamiltonian for the ALP-photon vector alone is no longer Hermitian. In this situation, we must therefore use a density matrix formalism:

$$H = \begin{pmatrix} \Delta_\gamma & 0 & 0 \\ 0 & \Delta_\gamma & \Delta_{\gamma a} \\ 0 & \Delta_{\gamma a} & 0 \end{pmatrix} - \begin{pmatrix} i\frac{\Gamma}{2} & 0 & 0 \\ 0 & i\frac{\Gamma}{2} & 0 \\ 0 & 0 & 0 \end{pmatrix}, \tag{1.22}$$

$$\rho = \begin{pmatrix} \mid \gamma_x \rangle \\ \mid \gamma_y \rangle \\ \mid a \rangle \end{pmatrix} \otimes \begin{pmatrix} \mid \gamma_x \rangle & \mid \gamma_y \rangle & \mid a \rangle \end{pmatrix}^*, \tag{1.23}$$

$$\rho(z) = e^{-iHz}\rho(0)e^{iH^\dagger z}. \tag{1.24}$$

1.1.4 Bounds on M

The probability of ALP-photon interconversion depends crucially on the mass scale M, which is model dependent and so is a priori undetermined. So far, no conclusive evidence for the existence of ALPs has been found. Instead, empirical limits on M (or equivalently on $G_{a\gamma\gamma} = 1/M$) have been derived from astrophysical observations and from ALP search experiments, as reviewed in [43]. These are shown in Figure 1.1, reproduced from [11]. The yellow region shows the parameter range of the QCD axion. We will now briefly summarise the bounds on the ALP-photon coupling displayed in Figure 1.1:

- For higher mass ALPs ($m_a \gtrsim 10^{-7}$ eV), the dominant bound is from the effect of the ALP degree of freedom on stellar evolution [44]. The existence of an ALP provides an additional cooling mechanism to the star, and is expected to alter the ratios of the number stars in different evolutionary phases. Values of the ALP-photon coupling $G_{A\gamma\gamma} = 1/M$ above the horizontal grey line in Figure 1.1 are excluded.

- Helioscopes search for ALPs produced in the sun by the Primakoff process $\gamma + Ze \to Ze + a$, detecting them on Earth using ALP to photon conversion in a large magnetic field [45]. Null results from helioscope searches rule out the blue region in Figure 1.1.

- Light shining through walls (LSW) experiments search for photons passing through opaque material through conversion to an ALP and subsequent re-conversion to a photon in an external magnetic field [46]. The probability for this process is $\sim G_{A\gamma\gamma}^4$, and this strategy currently has weaker sensitivity than searches based on astrophysical production.

- As photon to ALP conversion is polarization dependent, the ALP field induces additional vacuum birefringence in the presence of an external magnetic field. This effect is used by the PVLAS collaboration to place bounds on $G_{A\gamma\gamma}$ [47].

- Haloscopes search for ALP to photon conversion in a resonant cavity [48] - these bounds assume that coherent oscillations of the ALP field comprise all the local dark matter density.

- The grey exclusion in Figure 1.1 labeled 'telescopes' arises from the non-observation of the ALP decay line with optical telescopes [49–51]. This argument assumes the ALP is a QCD axion, with a thermal relic density set by hadronic interactions.

- For low mass ALPs ($m_a \lesssim 10^{-10}\,\mathrm{eV}$), the strongest bounds on M arise from observations of the SN1987a supernova in the Large Magellanic Cloud. ALPs would be produced in a supernova via the Primakoff process. We would therefore expect an ALP burst coincident with the neutrino burst. This ALP burst would be observable as a gamma ray flux following ALP-photon conversion in the Milky Way magnetic field. The non-observation of such a gamma ray flux

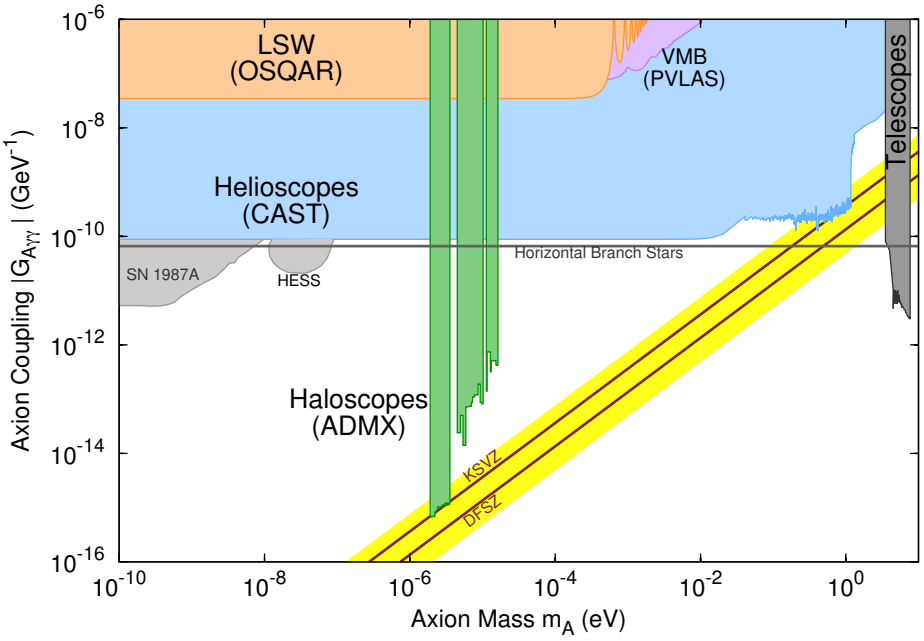

Figure 1.1: Empirical bounds on the ALP-photon coupling $G_{A\gamma\gamma} = 1/M$, as described in the text. Reproduced from [11].

leads to the bound $M \gtrsim 2 \times 10^{11}\,\mathrm{GeV}$ [52–54].

- The exclusion labeled 'HESS' in Figure 1.1 arises from non-observation modulations in the gamma-ray spectrum of the point source PKS 2155-304, as observed by the *HESS* telescope [55]. Such modulations would be expected from photon to ALP interconversion in the magnetic field of the surrounding galaxy cluster. In Chapter 2, we use a similar method at X-ray energies to obtain improved bounds on low mass ALPs.

Several possible anomalies that could be explained by the existence of ALPs have also been observed. The spectra of distant blazars suggest that intergalactic space is more transparent to gamma rays than predicted - this could be explained by these photons mixing with ALPs in the intergalactic magnetic field [56]. Hints of an exotic cooling mechanism in stars could also be explained by energy loss to an additional ALP degree of freedom [57]. The distribution of dark matter in galaxies, and in

particular the observation of caustic rings of dark matter are more easily explained with ALP dark matter, which behaves to a first approximation as a classical field, than with particle dark matter [58]. Finally, in this thesis we consider three anomalies in X-ray observations that could point to ALPs - the soft X-ray excess in galaxy clusters (Chapter 3), the anomalous 3.5 keV line (Chapters 4 and 5), and an anomalous 3.5 keV dip we observed in the AGN at the centre of the Perseus galaxy cluster (Chapters 2 and 5).

1.2 Astrophysical Observations and ALP Physics

Astrophysical environments provide extreme conditions that we could not hope to replicate on Earth, such as magnetic fields over kilo- or even mega-parsec scales and dark matter column densities exceeding those on Earth by many orders of magnitude. The dark matter column density $\mathcal{S}_{\rm DM}$ is of particular importance when seeking signals from dark matter. We define $\mathcal{S}_{\rm DM} = \int_0^L \rho_{\rm DM}(l)dl$, where $\rho_{\rm DM}$ is the dark matter density and the integral is performed along the line of sight to the object of interest. In this work I analyse X-ray telescope observations through a lens of ALP phenomenology, and more broadly with a view to constraining or discovering the physics of the dark sector. In particular, the large scale magnetic fields present in galaxy clusters, and to a lesser extent galaxies, make them excellent ALP-photon mixers. The origin of these magnetic fields is unknown, but radio observations demonstrate that fields of 1 - 10 μG are generically present in both galaxies and clusters. X-rays are the ideal wavelength to search for ALP-photon conversion, as for ultra-light ALPs propagating through an interstellar plasma it is at X-ray energies that distinctive oscillations are seen in the conversion probability.

Galaxy clusters are the largest gravitationally bound structures in the Universe.

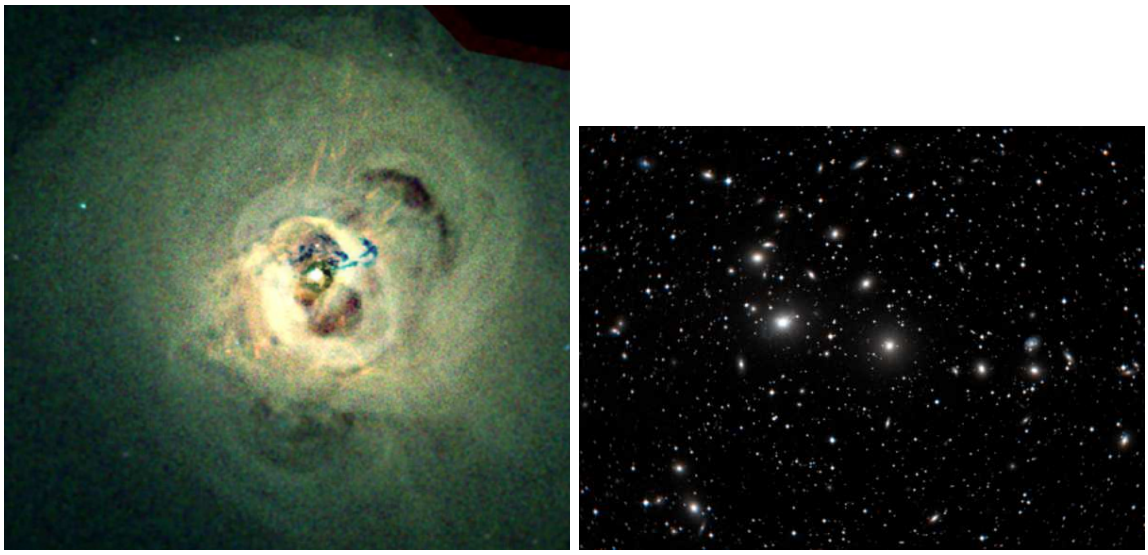

Figure 1.2: Left: The X-Ray emission from the intra-cluster medium in the Perseus galaxy cluster, as observed with the *Chandra* X-ray telescope. Right: An optical image of the Perseus galaxy cluster showing emission from the component galaxies, from the ESO Online Digitized Sky Survey.

By far the largest component of a galaxy cluster is its dark matter, accounting for around 90% of the cluster mass. 9% of the mass is in the intracluster medium (ICM), a magnetized plasma suffusing the entire cluster. The component galaxies make up the remaining 1%. The two baryonic components are show in Figure 1.2, as seen in the X-ray and optical bands respectively. Galaxy clusters extend over Mpc distances - their extreme size provides an ideal test bed for new physics. For example, their large dark matter column densities make them ideal targets in searches for weak interactions between the dark sector and the Standard Model.

The intracluster medium (ICM) is a multi-temperature plasma of baryons that have fallen into the gravitational well of the cluster. Its physics has been the subject of extensive observational and theoretical research, as reviewed in [59]. The ICM may be modeled by components with temperatures $T \sim \mathcal{O}(1 - 10\,\mathrm{keV})$, and emits in X-rays via thermal bremsstrahlung. The ICM also contains heavy ions formed in the supernovae of the cluster's galaxies, whose atomic lines are observed in X-ray observations. These ions populate the ICM at about $\frac{1}{3} - \frac{1}{2}$ of their solar abundance.

Of crucial importance to ALP-photon interconversion is the electron density and magnetic field of the ICM. Magnetic fields in galaxy clusters are observationally determined through Faraday rotation - the rotation of the plane of polarization of light passing through a magnetic field. We define the rotation measure:

$$\mathrm{RM} = \frac{e^3}{2\pi m_e^2} \int_0^L n_e(z) B_\parallel(z) dz, \tag{1.25}$$

where $n_e(l)$ is the electron density, $B_\parallel(l)$ is the magnetic field parallel to the photon's direction of travel, and the integral is performed along the line of sight. The observed polarization angle is then given by:

$$\theta = \theta_0 + \mathrm{RM}\,\lambda^2, \tag{1.26}$$

where θ_0 is the polarization angle of the source. As the effect is proportional to λ^2, polarized radio sources passing through the region of interest are required for this method of magnetic field determination.

By measuring θ at a number of different wavelengths, the magnitude of the rotation measure towards a particular source is estimated. By assuming spherical symmetry, the electron density profile may be determined from observations of the cluster's X-ray surface brightness, allowing us to estimate $B_\parallel(l)$. The coherence lengths of the magnetic field can then be inferred from the statistics of the rotation measure across the cluster.

Complimentary information about the cluster magnetic field is provided by the synchrotron emission emitted by relativistic charged particles whose acceleration has a component perpendicular to their velocity, such as is provided by a magnetic field. Many clusters show diffuse synchrotron emission at radio frequencies. The total synchrotron flux is proportion to both the magnetic field strength and the number densities of relativistic electrons. As the latter cannot be reliably determined, this method

cannot be used to directly estimate the magnetic field strength. However, rough estimates can be obtained by assuming that the energy in the relativistic electrons and the magnetic field is distributed such that the total energy is minimised.

Synchrotron emission is highly polarized in the plane of motion of the emitting particle, which is determined by the direction of the magnetic field. The polarization angle will subsequently undergo Faraday rotation. The degree and uniformity of the synchrotron polarization therefore provides information as to the spatial structure and coherence length of the magnetic field. The radio emission and magnetic fields of galaxy clusters are reviewed in [60].

Typical cluster electron densities are $\mathcal{O}(10^{-3}\,\mathrm{cm}^{-3})$. As described above, magnetic field determination is often more difficult. Nevertheless, magnetic fields of a few μG have been measured in many clusters, and coherence length measurements of a handful of clusters suggest structure on a scale of 10s of kpc. A subset of galaxy clusters exhibit very dense cores (the central ~ 20 kpc), such that the core gas' cooling time is less than the age of the universe [61]. The X-ray temperature is observed to decrease towards the cluster centre, although the observed cooling rate is lower than predicted. An additional heat source driven by feedback with the cool core is required to explain these observations - the nature of this feedback is currently unknown. Cool core clusters have particularly high magnetic fields (a few tens of μG) and electron densities in the central cool core region.

We also study ALP phenomenology in individual galaxies, particularly in the Milky Way. The Milky Way's magnetic field is very well determined based on over 40,000 extra-galactic rotation measures [62, 63]. Furthermore, the Milky Way electron density may be inferred from pulsar dispersion and emission measures. Pulsar radiation is highly spatially coherent, and so is significantly perturbed by scattering

from free electrons along the line of sight. Radio observations of pulsars allow us to infer the spatial distribution the electron density n_e [64]. This interaction slows the photon's propagation. Lower energy photons are slowed more than higher energy photons, leading to a temporal broadening to the pulsar's emission. We define the dispersion measure as the line of sight integral of the electron density:

$$\mathrm{DM} = \int_0^D dz\, n_e(z). \tag{1.27}$$

Due to the pulse broadening described above, we find:

$$\mathrm{DM} \propto \frac{t_2 - t_1}{\nu_1 - \nu_2}, \tag{1.28}$$

where t_1 and t_2 are the arrival times of frequency components ν_1 and ν_2 from the pulsar. The emission measure is the line of sight integral of n_e^2:

$$\mathrm{EM} = \int_0^D dz\, n_e(z)^2. \tag{1.29}$$

Emission measures are calculated based on the $H\alpha$ line intensity from recombination of electrons and protons in the interstellar plasma. Combining the emission and dispersion measures gives information about the structure of the Milky Way's electron density, which is described in Chapter 3. In general, galaxies host similar magnetic field strengths and electron densities to clusters, but are two orders of magnitude smaller. They are therefore typically much poorer ALP-photon converters.

We analyse the extensive X-ray data archive to search for and constrain new fundamental physics that could operate in galaxies and galaxy clusters. We use analyses and observations from several X-ray telescopes, including *XMM-Newton*, *Chandra* and *Hitomi*. *XMM-Newton* and *Chandra* make use of charge coupled device (CCD) technology to detect the electrical charge produced by the absorption of an X-ray

photon. This provides an energy resolution of $\mathcal{O}(100)$ eV. *Hitomi* was the first X-ray telescope to offer microcalorimeter technology, providing an energy resolution of $\mathcal{O}(5)$ eV. This vast improvement in spectral resolution would allow a far better characterization of the ICM through precise resolution of atomic lines. It would also greatly improve the reach of X-ray observations in detecting new physics. For example, this finer energy resolution allows rapid ALP-photon oscillations to be resolved, and allows us to distinguish baryonic from dark matter line features by their line width. Sadly, *Hitomi* was lost in March 2016, 37 days after launch. However, it returned high resolution images of the centre of Perseus, which can be applied to study both the ICM and Beyond the Standard Model physics.

This thesis is structured as follows. In Chapter 2, we place bounds on the ALP-photon coupling from the non-observation of spectral modulation in point sources passing through galaxy clusters. In Chapter 3, we study the physics of a Cosmic Axion Background and make predictions for its (non-)observation in galaxies. In Chapter 4 we review the anomalous 3.5 keV line observed in galaxy clusters, and discuss a model for the line in which 7 keV dark matter decays to an ALP which subsequently converts to a photon in the cluster magnetic field. This model reproduces the line's morphology and predicts that it is not observed in most galaxies. In Chapter 5 we propose an alternative model for the 3.5 keV line, motivated by our observation of a dip at 3.5 keV in the AGN at the centre of the Perseus galaxy cluster, and in Chapter 6 we conclude.

Chapter 2

Constraints on ALP-Photon Mixing from X-ray Point Sources

This chapter is based on [1] and [2] written in collaboration with Marcus Berg, Joseph Conlon, Nicholas Jennings, Sven Krippendorf, Andrew Powell and Markus Rummel.

2.1 Introduction

If ALPs exist, $\gamma \leftrightarrow a$ interconversion results in energy-dependent modulations of an initially pure photon spectrum passing through a magnetic field. Galaxy clusters are particularly efficient photon-ALP converters [65, 66], and so we might hope to observe this effect in observations of bright point sources in or behind galaxy clusters. For typical cluster electron densities and magnetic fields, interconversion between X-ray photons and very low mass ALPs is quasi-sinusoidal in energy space [66–69]. Compared to the source spectrum, the spectrum of arriving photons then has these quasi-sinusoidal oscillations imprinted on it. By searching for such modulations, we can place constraints on the coupling parameter M.

For this purpose, quasars or active galactic nuclei (AGNs) that are either behind or embedded in galaxy clusters provide attractive sources. The original photon spectrum

is reasonably well described by an absorbed power-law, and all photons arise from a single sightline passing through the cluster. This ensures that all photons experience the same magnetic field, and so the same survival probability. As bright sources, AGNs can also provide the large number of counts necessary for statistical leverage in searching for oscillatory modulations of the photon spectrum. This method has also been used to constrain ALP-photon mixing in [67, 70–72]. In this chapter we place constraints on M using the spectra of several point sources shining through galaxy clusters. We use archival data from the *Chandra* X-Ray telescope, which offers a largely untapped archive of observations potentially sensitive to ALP-photon mixing.

The chapter is organised as follows. Section 2.2 provides further details on the attractiveness of bright quasars or AGNs for searching for ALPs. In section 2.3 we describe the point sources we have used to place limits on M. Section 2.4 describes our analysis method and results. We describe the magnetic fields and electron density models used in section 2.5. In section 2.6 we describe bounds on the ALP-photon coupling, and we conclude in section 2.7.

2.2 Point Sources and ALP Physics

Observations of galaxy clusters at X-ray energies sit at a sweet spot for photon-ALP physics. This is due to two key results. First, galaxy clusters are *particularly efficient* environments for photon-ALP interconversion. The electron densities are relatively low. Clusters have magnetic fields that are not significantly smaller than in galaxies, but in which the **B**-field extends over megaparsec scales, far greater than the tens of kiloparsecs applicable for galactic magnetic fields. The magnetic field coherence lengths in clusters are also larger than in galaxies, comfortably reaching tens of kiloparsecs. For massless ALPs, this feature singles out galaxy clusters as providing the most suitable environment in the universe for ALP-photon interconversion.

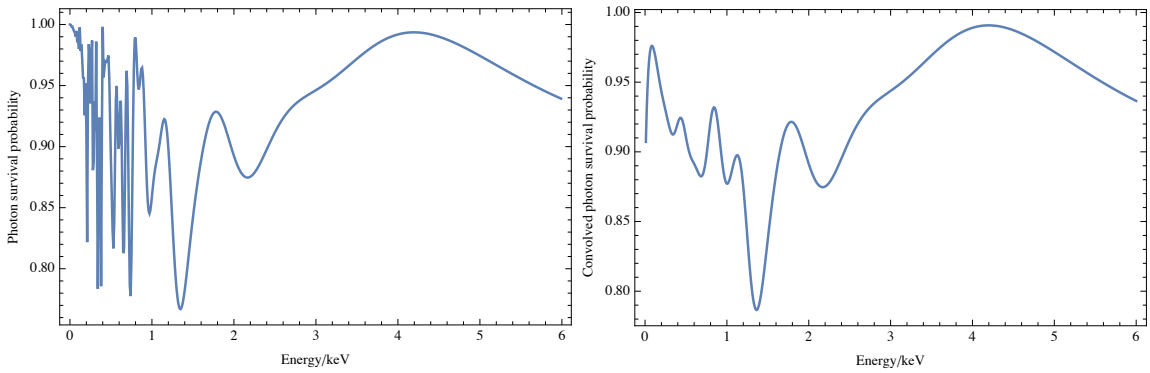

Figure 2.1: Left - The photon survival probability for a photon propagating from NGC3862 in A1367 (see below) to us. The ALP-photon coupling is $M = 5\times10^{11}$ GeV. Note that the precise form of the survival probability depends on the unknown configuration of the magnetic field along the line of sight. However, the oscillatory structure is generic. Right - The photon survival probability for the same magnetic field convolved with a Gaussian with FWHM of 150 eV, the energy resolution of *Chandra*.

The second key result is that, for the electron densities and magnetic field structures present within galaxy clusters, the photon-ALP conversion probability is energy-dependent, with a quasi-sinusoidal oscillatory structure at X-ray energies. This provides distinctive spectral features to search for. We illustrate this in Figure 2.1, where we plot a typical photon survival probability as a function of energy, along a single line of sight modeled on that from the AGN NGC3862 through the galaxy cluster A1367 to us.

The precise form of the survival probability is not predictable. It depends on the actual magnetic field structure along the line of sight, and so differs for each line of sight. Faraday rotation measures can give statistical information about the strength and extent of magnetic fields, as for the Coma cluster in [73], but the actual magnetic field along any one line of sight is unknown. However the form shown in Figure 2.1 – a quasi-sinusoidal structure with a period that increases with energy – is generic, and arises for any reasonable choice of central magnetic field value or range of coherence lengths. The inefficiency of conversion at energies $E \lesssim 0.2\,\mathrm{keV}$ is also generic, implying that effects of photon-ALP conversion are not visible in the

optical (and below) range. At higher energies $E \gtrsim 5\,\mathrm{keV}$, conversion is efficient but not strongly dependent on energy, and therefore not detectable without knowing the original luminosity of the source.

Figure 2.1 (right) also shows the same survival probability convolved with a Gaussian with full width at half maximum (FWHM) of 150eV, representing the approximate energy resolution of the CCD detectors present on *Chandra* (the precise Figure of 150eV is taken from the in-orbit performance of the ACIS-I detectors on *Chandra*, see table 6.4 of the *Chandra* proposer's guide[1]). While at the lowest the energies the oscillations are too rapid to be resolved by CCD detectors, and would require microcalorimeters such as those that were present on *Hitomi*, in general it is fortuitous that the scales of the oscillations match those of the X-ray telescopes extensively used to observe galaxy clusters.

If ALPs exist, then for photons arriving from a single location, this conversion imprints a particular quasi-sinusoidal modulation on the actual photon spectrum. There is also an overall reduction in luminosity, but this can be absorbed into the overall normalisation of the spectrum. For unpolarised light the $\gamma \to a$ conversion probability cannot exceed fifty per cent, and in the limit of strong coupling saturates at an average value of $\langle P(\gamma \to a) \rangle = 1/3$, as expected from considering the degrees of freedom (for example, see [70]). It therefore follows that, expressed as a ratio of data to model, the maximal allowed range of ALP-induced modulations is approximately $\pm 30\%$.

There are three effects that can wash out these modulations. The first is the finite energy resolution of the telescope; as shown in Figure 2.1, this removes any structure present at the lowest energies. The second is when emission arises from an extended source, involving many different lines of sight. In this case the peaks and troughs from different lines of sight average out, reducing any signal. The third is insufficient

[1] `http://cxc.harvard.edu/proposer/POG/html/chap6.html`

photon statistics, when localised oscillations become indistinguishable from Poisson fluctuations.

Bright point-like sources either behind or embedded in a galaxy cluster are particularly attractive for searching for ALP-induced modulations. The galaxy cluster provides a good environment for ALP-photon conversion; the bright point source ensures there are many photons, all passing along the same line of sight.

These factors make quasar or AGN spectra attractive for searching for ALPs. Emission from an AGN arises from matter accreting onto the central black hole. As evidenced by the rapid time variability of AGN luminosities, the physical region sourcing the X-ray AGN emission is tiny – of order a few Schwarzschild radii of the central black hole. As cluster magnetic fields are ordered on kiloparsec scales, this implies that for all practical purposes every photon arising from the AGN has experienced an identical magnetic field structure during its passage to us.

To first approximation, at X-ray energies an AGN spectrum can be described as a power law spectrum absorbed by neutral hydrogen. The effect of ALPs is then to imprint a quasi-sinusoidal modulation on this power law, of relative amplitude at most $\mathcal{O}(30\%)$ and with a modulation period of order a few hundred eV. As the fractional Poisson error on N counts is $\frac{1}{\sqrt{N}}$, and CCD detectors such as those on *Chandra* have intrinsic energy resolutions of around $\mathcal{O}(150\text{eV})$, it therefore requires large numbers of counts to be able to distinguish any ALP-induced modulations from normal statistical fluctuations.

2.3 The Observations

We place bounds on M using the following sources:

- The AGN NGC1275 at the centre of the Perseus galaxy cluster
- The quasar B1256+281 behind the Coma galaxy cluster

Source	Exposure [ks]	Projected offset from cluster centre [kpc]	LOS offset from cluster
NGC1275	200	0	0
B1256+281	493	232	Behind cluster
NGC3862	75	186	Unknown
2E3140	660	456	Unknown

Table 2.1: The sources used to place bounds on M

- The AGN NGC3862 in the cluster A1367
- The Seyfert galaxy 2E3140 in the cluster A1795

Table 2.1 lists the observation time available from *Chandra* for each source. The magnetic field experienced by photons travelling from a source to us depends on the source's position relative to the galaxy cluster. Table 2.1 lists the projected offset from the cluster centre in the plane of the sky, as well as each source's position with respect to the cluster centre along the line of sight (LOS). The line of sight positions of two of the sources - NGC3862 and 2E3140 - with respect to their host clusters are not known. Based on the redshifts of these point sources, we know that they lie within the cluster. However, they could be near the back of the cluster (from our point of view), shining through the entire cluster magnetic field, or near the front of the cluster, shining through only a very small region of the cluster's magnetic field. It is not possible to distinguish between these possibilities observationally. We therefore assume that these sources are in the middle of the cluster along the line of sight, and take 1 Mpc for the propagation length of their spectra through the cluster magnetic field. We note that, in the unlucky event that NGC3862 and/or 2E3140 were actually located near the front of the cluster, their bounds on $g_{a\gamma\gamma}$ would be much weaker than presented here.

The data from NGC1275 is contaminated by pile-up. (The other sources are sufficiently dim that pile-up is negligible.) The energy recorded on the individual ACIS pixels (each approximately 0.5 arcseconds square) is read out approximately

every three seconds (one frame time) in these observations. Based on groupings of 3×3 pixels, events are assigned a grade, representing the likelihood that the event arises from a real photon. Pile-up refers to the arrival of more than one photon in this grouping within the same readout frame. This can lead to the energy of the two (or more) incident photons being summed, and either treated incorrectly as a single photon event of higher energy, or assigned a bad grade (grade migration). For an on-axis bright source, the level of pile-up can be high, and the resulting spectrum contains events with two, three (and more) photons. As pile-up is a statistical feature of the number of arriving photons, some level of pile-up is inevitable in any observation. The question is always whether the magnitude of pile-up is sufficient to corrupt the science analysis being undertaken.

In terms of the measured photon distribution, the general effect of pile-up is to cause a hardening of the spectrum: two or more lower-energy photons are misidentified as a single higher-energy photon. This implies that for a fit of a single power-law to a photon distribution, as pile-up increases the best-fit power-law index will decrease. In a spectrum contaminated by pile-up, this makes it harder to determine the correct original power-law index.

What about searches for and constraints on ALPs? As we have seen in Section 2.2, the distinct signal of ALPs is a quasi-sinusoidal modulation in the spectrum – a local excess or deficit in the photon count rate compared to the nearby continuum. For sufficiently small levels of pile-up, localised modulations will remain localised modulations, as an overall global continuum redistribution of photons is unable to create or remove localised spikes (or dips) relative to the continuum.[2] However, for sufficiently heavy pile-up, the majority of photons will be redistributed and such local features will be lost.

While pile-up is always a contaminant on the spectrum, what this implies is that

[2]In the case of a strong low-energy emission line, this is not true, as its pile-up may result in spikes at integer multiples of the original line.

a search for localised spectral irregularities is more robust against pile-up than, for example, a measurement of the overall power-law spectral index of a source. While some movement of counts from low to high energies will reduce the number of low-energy photons compared to high energy photons, it will be less likely to affect the presence or absence of sharp localised features.

This robustness is more applicable at low energies. The effective area of the *Chandra* telescopes starts falling rapidly above around 5 keV.[3] As at higher energies a power-law distribution also produces intrinsically fewer photons, it only requires a small amount of pile-up of lower-energy photons into the $E > 5$ keV region to cause a significant distortion of the spectrum there.

In contrast, at lower energies the effective area is larger and there are far more photons, so small amounts of pile-up will not affect any spectral features. For observations towards Perseus, there is an additional benefit: the high galactic absorbing column density ($n_H = 1.5 \times 10^{21}\,\mathrm{cm}^{-2}$) removes the lowest-energy photons, resulting in an effective minimal value for a piled-up energy $E_1 + E_2$.

There is an important caveat to this which requires careful treatment. In the presence of rapid variations in the effective area, a failure to account for pile-up can result in significant spectral distortion. This is because the distribution of pile-up photons around $E_1 + E_2$ does not respect the behaviour of the effective area at $E_1 + E_2$, but instead only the effective areas near E_1 and E_2. If the effective area is rapidly varying near $E_1 + E_2$, and pile-up photons make up a large fraction of the total photon count at $E_1 + E_2$, then a fitted spectrum will introduce unphysical features at $E_1 + E_2$. In the case of *Chandra*, there is a sharp dip in the effective area at around 2 keV arising from an Iridium edge, and the effective area also falls off rapidly for energies above 5 keV. Between 2.5 and 5 keV the effective area is relatively constant and smoothly varying.

[3] cf. `cxc.harvard.edu/proposer/POG/html/ACIS.html`

In placing bounds on ALPs, we mitigate the effect of pile-up by using only the observations of NGC1275 in which it is on the edge of the chip. In this location, the point spread function (PSF) is larger and so the AGN emission is spread over more pixels, and therefore pileup is minimized [74]. Several effects contribute to the higher off-axis PSF. Notably, the focal plane of *Chandra*'s mirrors is curved whereas the detector is flat. The error introduced by this mismatch increases as we move further off-axis. We also focus only on the energy range 1 - 4 keV when setting limits on M with NGC1275. We also note that the overall effect of pileup is to make a no-ALP model a worse fit to the data, thus making our inferred bounds on the ALP-photon coupling more conservative.

In addition to the sources listed in Table 2.1, we analysed the quasar SDSS J130001.47+275120.6 behind Coma; the AGN IC4374 in A3581; the quasar CXOUJ134905.8+263752 behind A1795, and the AGN UGC9799 in A2052. However, we found that, with the data currently available, these sources could not exclude any value of M at the 95% confidence level.

We used `CIAO 4.7` [75] to analyse the NGC1275 spectra and `CIAO 4.8` for the other spectra. [4] We used `Sherpa` [76] and `HEASOFT 6.17` to fit the functional form of the spectra. After the data is reprocessed using `CALDB`, it is cleaned from time periods that are polluted by flares using the program `chips`. Spectra and responses were created using `specextract` for each observation. Where multiple observations of the same source are available, we stack these observations using `combine_spectra`. We extract the background emission from a region near the source, and subtract this from the spectrum before fitting.

[4]The update to `CIAO 4.8` affects data taken in Continuous Clocking mode, which does not apply to these observations.

2.4 Results

We fit each spectrum with a power law absorbed by neutral hydrogen:

$$F(E) = AE^{-\gamma} \times e^{-n_H \sigma(E)} \,. \tag{2.1}$$

Here A denotes the normalisation of the power-law, γ the power-law index, and n_H the effective Hydrogen column density. In some cases we find that the spectrum is well fit with no absorption. We also include a soft thermal component and the 6.4 keV Fe Kα line where necessary.

2.4.1 NGC1275 in Perseus

The resulting stacked spectrum contains around 266000 counts, reducing to 230000 after background subtraction, giving a ratio of 6.5:1 for the AGN against the cluster emission. The resulting spectrum was binned to ensure a minimum of 2000 counts per bin, and fitted between 0.8 and 5 keV with an absorbed power law `xswabs` × `powlaw1d`.

The resulting fit is shown in Figure 2.2, together with the fractional ratio of data to model. The best-fit value of n_H is $2.3 \times 10^{21}\mathrm{cm}^{-2}$ and the power-law index is $\gamma = 1.83 \pm 0.01$. While the absorbed power-law is a reasonable characterisation of the data, there are two large localised residuals: one positive between 2–2.2 keV and one negative around 3.4–3.6 keV. There is an upward trend at 5 keV. As the effective area of *Chandra* begins to fall off rapidly here, and there are also intrinsically fewer photons expected, pile-up plays a proportionately more important role. This rising trend continues beyond 5 keV and we attribute this to the effects of pile-up. The feature at 2-2.2keV is at the same location as a sharp effective area edge from the Iridium coating of the mirrors. As pile-up arising from high flux levels can generate fake excesses at the location of such edges, we associate the feature with this edge

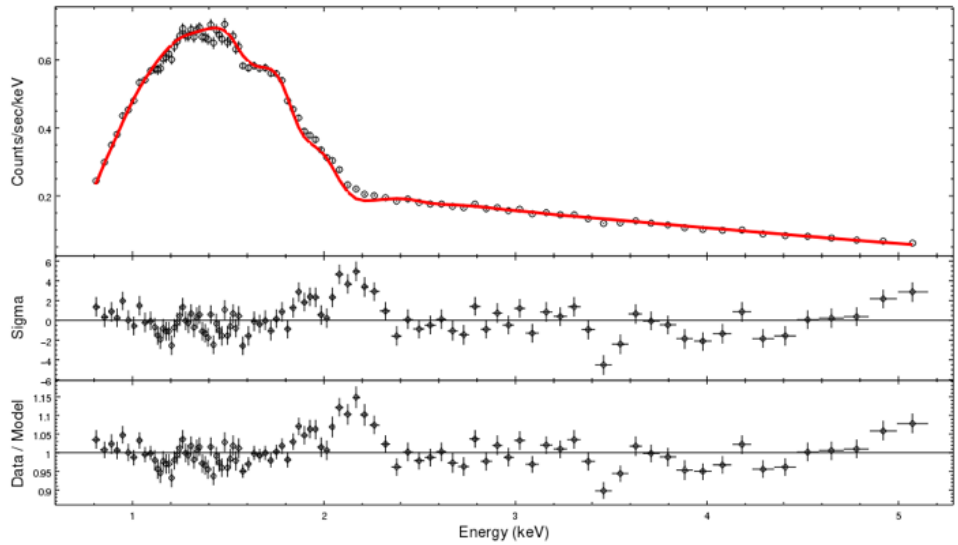

Figure 2.2: The complete stacked spectrum of the ACIS-I edge observations, involving 230000 counts after background subtraction. The fit is to an absorbed power law, and results in $n_H = 2.3 \times 10^{21}\text{cm}^{-2}$ and a spectral index of $\gamma = 1.83$. σ refers to the standard deviation from the model expectation for a Poissonian count rate.

and do not discuss it further. The residual at 3.4–3.6 keV does not coincide with an effective area feature, and so cannot be easily explained as an instrumental effect. We could in theory interpret this feature as arsing from the ALP-photon conversion we are seeking in this chapter. However, we note that it is at the same energy as the unidentified 3.5 keV line observed in galaxy clusters discussed in chapter 4. In chapter 5, we consider a dark matter model in which the two anomalies are caused by the same new physics. ALP-photon conversion cannot easily explain their coincidence in energy, so we do not consider this to be the most promising new physics explanation.

2.4.2 Quasar B1256+281 behind Coma

This quasar is located behind the Coma cluster at a redshift of $z = 0.38$. Its sight-line passes through the entirety of the Coma intra-cluster medium (ICM). There are around 5000 counts from the source, of which around 10% can be attributed to the ICM (as the source is always off-axis, the *Chandra* Point Spread Function is degraded

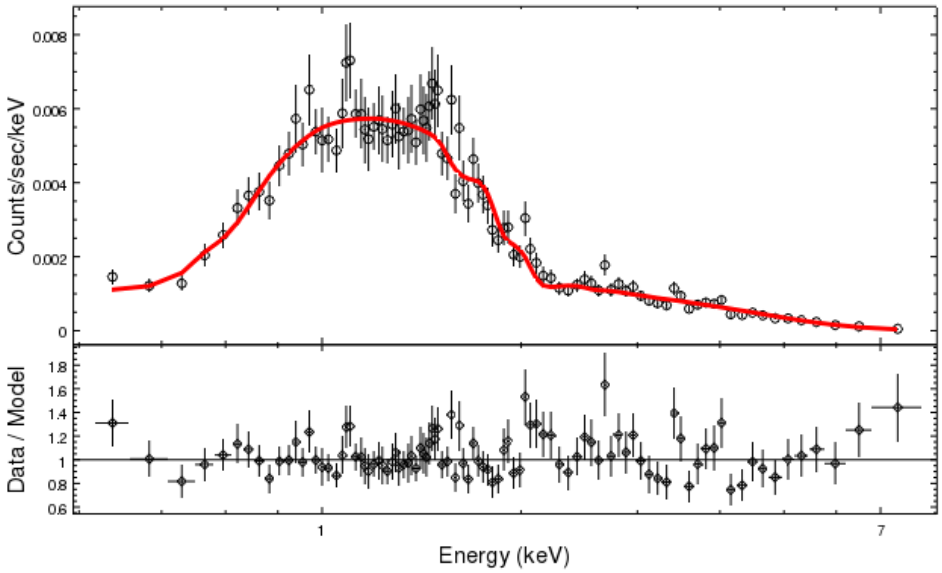

Figure 2.3: The stacked spectrum of the quasar B1256+281 behind Coma. The fit is an unabsorbed power law of index $\gamma = (1.75 \pm 0.03)$.

compared to an on-axis observation, increasing the level of contamination from thermal cluster emission).

Grouping counts so that there are at least 40 counts per bin, the quasar spectrum from 0.5 to 7 keV is well-fit by an unabsorbed power-law with index 1.75 ± 0.04 (a reduced χ^2 of 0.88 for 96 degrees of freedom). There is no requirement for an Fe Kα line. The spectrum is plotted in Figure 2.3. No significant residuals are observed, and we can say that there are no ALP-induced modulations in the spectrum beyond the 20% level.

2.4.3 NGC3862 within A1367

The AGN NGC3862 within the cluster A1367 is characterised by a very soft power-law (index 2.30 ± 0.03) absorbed by a column density of $n_H = 5 \times 10^{20} \mathrm{cm}^{-2}$, supplemented by a soft thermal component $T \sim 0.3$keV. Grouping counts so that there are at least 50 counts per bin, the reduced χ^2 is 0.83 for 144 degrees of freedom, with a total of

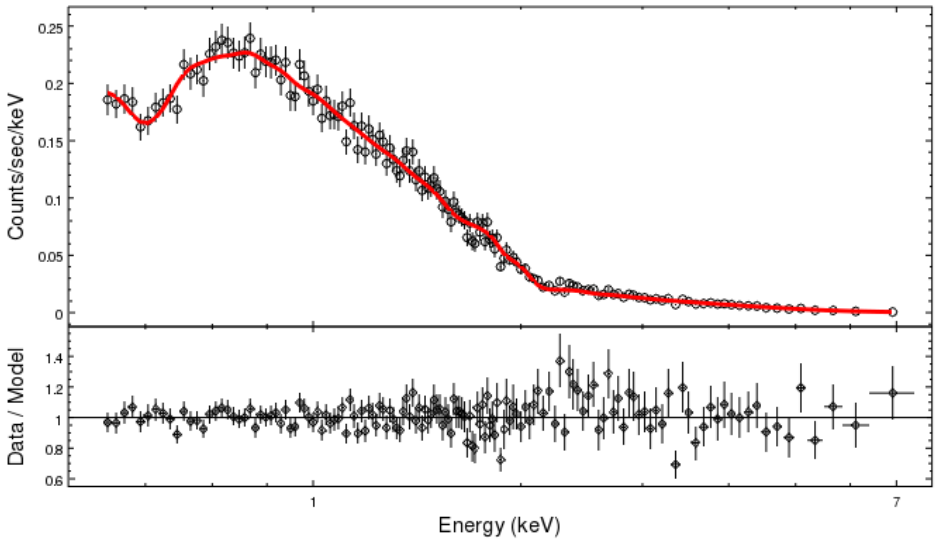

Figure 2.4: The stacked spectrum of the AGN NGC3862 in A1367. The fit is the sum of a power law of index $\gamma = (2.30 \pm 0.05)$ plus a soft thermal component with temperature 0.3 keV, absorbed by a column density of $n_H = 5 \times 10^{20}\mathrm{cm}^{-2}$.

21000 counts after background subtraction. The spectrum is plotted in Figure 2.4 and the resulting fit shows no sign of any significant spectral irregularities.

2.4.4 Seyfert galaxy 2E3140 in A1795

This is a bright unobscured AGN. Its redshift is 0.059, compared to a cluster redshift of 0.062. The radial velocity difference is $1000\,\mathrm{kms}^{-1}$, which is within the range of the A1795 velocity dispersion, and is consistent with 2E3140 being a bound member of the cluster A1795, with a sightline that passes through the intracluster medium.

However, we do not know the precise 3D location within the intracluster medium, and therefore whether the line of sight passes through most or only small amounts of the ICM. We assume a midway position.[5] The extracted spectrum contains around 78000 counts (of which around 1000 are ICM background). The spectrum from 0.5

[5]This is perhaps supported by the large velocity relative to the cluster centre, as an object undergoing harmonic motion about a central source has maximal relative velocity at the midpoint of its oscillation.

to 6 keV is very well fit by the sum of a power-law with index $\gamma = 2.11 \pm 0.01$, a soft thermal component with $T \sim 0.1$keV and a weak Fe Kα line at 6.4 keV in the rest frame (the Sherpa model `powlaw1d` + `xsapec` + `xszgauss`). Consistent with the galactic n_H column density in this direction, no absorption is required in the fit. Grouping counts so that there are at least 500 in each bin, the overall fit is excellent with a reduced χ^2 of 0.98 for 103 degrees of freedom. The spectrum is plotted in Figure 2.5.

2.4.5 Summary of fits for ALP constraints

To constrain the ALP-photon coupling, we note that the fit to the spectrum of NGC1275 contains no residuals above the 10% level, and fits to the other sources show no significant residuals. If they exist with strong enough coupling, ALPs can induce fractional modulations of up to 50% in the spectrum. The fact that no modulations of this size are observed can be used to constrain ALP parameter space.

2.5 The Cluster Environment

Magnetic fields in galaxy clusters are described by a turbulent power spectrum with structure across a range of scales. The exact configuration of the field along the line of sight is not known, and in practice we randomly generate many instances of the field from a given power spectrum. The parameter most relevant to ALP-photon conversion is the central magnetic field strength B_0. Based on results for the Coma cluster [73], we assume that B decreases with radius as $B \propto n_e^{0.7}$ for each cluster. We simulate each field by drawing domains from a power law distribution. The magnetic field and electron density are constant in each domain, with $B(r)$ and $n_e(r)$ evaluated at the centre of the domain and the direction of $\mathbf{B}$ chosen at random. The length l of each domain is between L_{min} and L_{max}, randomly drawn from a power

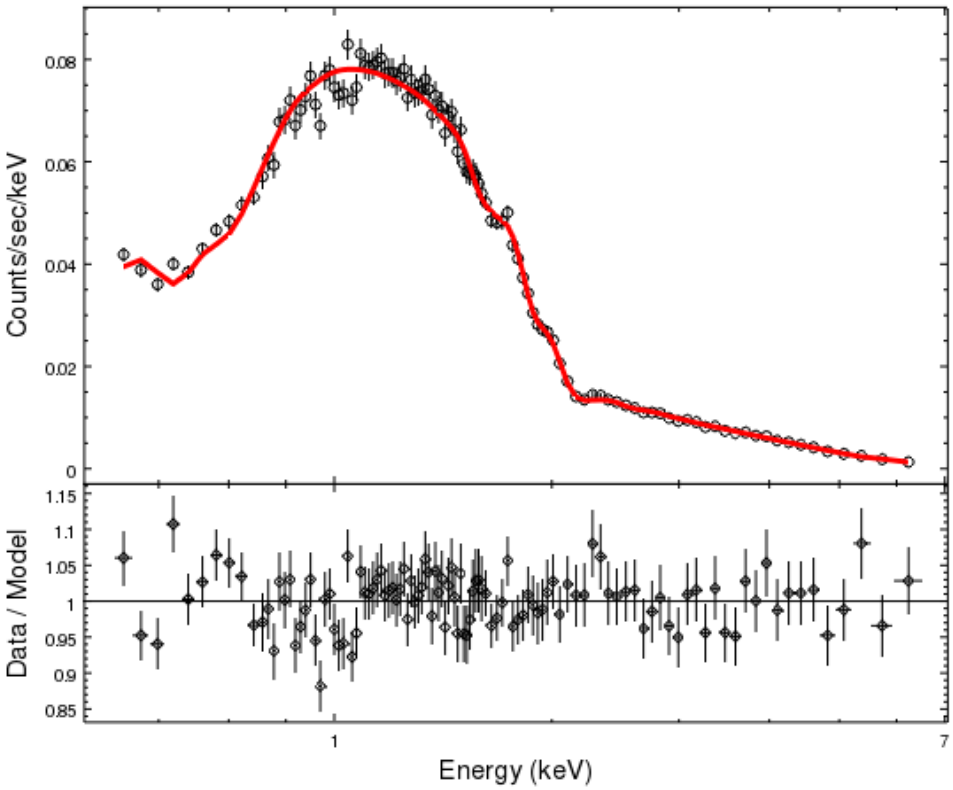

Figure 2.5: The stacked spectrum of the bright Seyfert 1 galaxy 2E3140 located in A1795. The fit is the sum of a power-law with $\gamma = 2.11 \pm 0.01$, a soft thermal component with $T \sim 0.1$keV and a weak Fe Kα line at 6.4 keV in the rest frame (`powlaw1d` + `xsapec` + `xszgauss`). Grouping counts so that there are at least 500 in each bin, the overall fit is excellent with a reduced χ^2 of 0.98 for 103 degrees of freedom.

law distribution with index n. We therefore have:

$$P(l=x) = N \begin{cases} 0 & \text{for } x > L_{max} \ , \\ x^{-n} & \text{for } L_{min} < x < L_{max} \ , \\ 0 & \text{for } x < L_{min} \ , \end{cases} \tag{2.2}$$

with normalisation constant N.

The cluster electron density is typically described by a β-model:

$$n_e(r) = n_0 \left(1 + \frac{r^2}{r_c^2}\right)^{-3\beta/2} . \tag{2.3}$$

2.5.1 Perseus

The central field in Perseus is estimated as $B_0 = 25\,\mu$G in [77]. The electron density is described by a double β-model [78]:

$$n_e(r) = \left(\frac{3.9 \times 10^{-2}}{[1 + (\frac{r}{80\,\mathrm{kpc}})^2]^{1.8}} + \frac{4.05 \times 10^{-3}}{[1 + (\frac{r}{280\,\mathrm{kpc}})^2]^{0.87}} \right) \mathrm{cm}^{-3} .$$

The coherence length and power spectrum of the magnetic field in the centre of Perseus is not observationally determined. Instead, we choose parameters motivated by those found for the cool core cluster A2199 [79], taking a conservative value for the magnetic field radial scaling. We take $L_{min} = 3.5$ kpc, $L_{max} = 10$ kpc and $n = 1.2$. As NGC1275 is situated at the centre of Perseus, we use a total propagation length of ~ 1 Mpc. (In this work we will take 1 Mpc as a standard value for the radius of a galaxy cluster.)

2.5.2 Coma

The magnetic field and electron density of Coma are estimated in [73]. The parameters are $B_0 = 4.7\,\mu G$, $L_{min} = 1$ kpc, $L_{max} = 17$ kpc and $n = \frac{1}{3}$. The electron density is given by a β-model with $n_0 = 3.44 \times 10^{-3}\,\mathrm{cm}^{-3}$, $r_c = 291$ kpc and $\beta = 0.75$. As the quasar studied is located behind Coma, we use a propagation length of ~ 2 Mpc.

2.5.3 A1367

We take the electron density from [80] and the central magnetic field is estimated in the article by M. Henriksen in [81]. This gives us $B_0 = 3.25\,\mu G$, $n_0 = 1.15 \times 10^{-3}\,\mathrm{cm}^{-3}$, $r_c = 308$ kpc and $\beta = 0.52$. In the absence of other estimates, we take the same values of n, L_{min} and L_{max} as for Coma. The 3-dimensional location of NGC3862 within the cluster is unknown, and therefore we take the median value of ~ 1 Mpc for the propagation length.

2.5.4 A1795

For A1795 the central magnetic field is taken from [82], the β-model parameters from [83] and the central electron density from [84]. These are $B_0 = 20\,\mu G$, $n_0 = 50 \times 10^{-3}\,\mathrm{cm}^{-3}$, $r_c = 146$ kpc and $\beta = 0.631$. Again, we take the same values of n, L_{min} and L_{max} as for Coma and ~ 1 Mpc for the propagation length.

2.6 Bounds on ALPs

We use the absence of significant residuals in the spectra (or in the case of NGC1275 residuals larger than 10%) to place bounds on the ALP-photon coupling. To obtain approximate bounds on M, we compare two models for the flux $F(E)$ observed from each source:

- Model 0: The no-ALP fit to each source described above. For example, an absorbed power law $F_0(E) = AE^{-\gamma} \times e^{-n_H \sigma(E)}$, as described in Equation (2.1).

- Model 1: An absorbed power law multiplied by the photon survival probability assuming the existence of ALPs with coupling M. In this case the predicted flux also depends upon the magnetic field $\mathbf{B}$ along the line of sight. We have, for example, $F_1(E, \mathbf{B}) = AE^{-\gamma} \times e^{-n_H \sigma(E)} \times P_{\gamma\to\gamma}(E(1+z), \mathbf{B}, M)$.

We compute 95% confidence limits on M by generating fake data from Model 1 and assessing how well it is fit by Model 0 i.e. how well the oscillations due to ALP-photon conversion can hide in the Poisson noise. For NGC1275, we fit the spectrum between 1 and 4 keV (a region largely unaffected by pile-up) and bin such that there are 1000 counts in each energy bin. For the other sources, we fit between 1 and 5 keV, and use the same binning as for the no-ALP fits described above. We use `Sherpa`'s Levenberg-Marquardt fitting method with Poisson errors derived from the value of the data in each bin. Our procedure to determine whether ALPs with coupling M are excluded at the 95% confidence level is as follows:

1. Fit Model 0 to the real data and find the corresponding reduced χ^2, $\chi^2_{\rm data}$.

2. Randomly generate 50 different magnetic field realisations $\mathbf{B}_i$ for the line of sight to the source.

3. For each $\mathbf{B}_i$, compute $P_{\gamma\to\gamma}(E, \mathbf{B}_i, M)$ by numerically propagating photons at different energies through $\mathbf{B}_i$, as described in chapter 1. We take 400 photon energies equally spaced between 1 and 5 keV. In the case of NGC1275, we take 300 photon energies equally spaced between 1 and 4 keV, in order to avoid the region contaminated by pileup.

4. For each $\mathbf{B}_i$, generate 10 fake data sets from Model 1, using `Sherpa`'s fake pha method.

5. Fit Model 0 to each of the 500 fake data sets and find the corresponding reduced χ^2, χ^2_i for each.

6. If fewer than 5% of the χ^2_i are lower than $\chi^2_{\rm data}$, $g_{a\gamma\gamma}$ is excluded at the 95% confidence level. If $\chi^2_{\rm data} < 1$, we instead require that fewer than 5% of the χ^2_i are less than 1 for the corresponding value of M to be excluded at the 95% confidence level.

The 95% confidence level lower limits on M obtained in this way from NGC1275, B1256+281, NGC3862 and 2E3140 are 6.7×10^{11} GeV, 1.7×10^{11} GeV, 3.4×10^{11} GeV and 6.7×10^{11} GeV respectively. One of the best bounds arises from NGC1275, despite the residuals in the no-ALP fit to this source. This is because of the very large number of counts available, and the high magnetic field of Perseus. If we exclude the 1.8 - 2.3 keV region from the NGC1275 spectrum, we would obtain an improved bound $M \gtrsim 9.1 \times 10^{11}$ GeV.

Each bound is affected by the fact that we do not know the precise magnetic field structure along the line of sight to the source. Therefore our limit setting procedure takes into account the fact that the field might be unfortunately good at hiding ALPs. However, it is unlikely that the fields for each of our four sources are well above average at hiding ALPs. This is not taken into account in our bounds, which are therefore in this sense very conservative. Conversely, our bounds could be systematically affected by incorrect estimates of the cluster magnetic fields. This is less likely to have occurred for four separate clusters, but remains a possibility. As shown in Figure 2.6, these bounds are world leading.

2.7 Conclusions

The most basic point of this chapter is that X-ray observations of bright point sources in and behind galaxy clusters are a superb way to search for ALPs. If ALPs exist, they

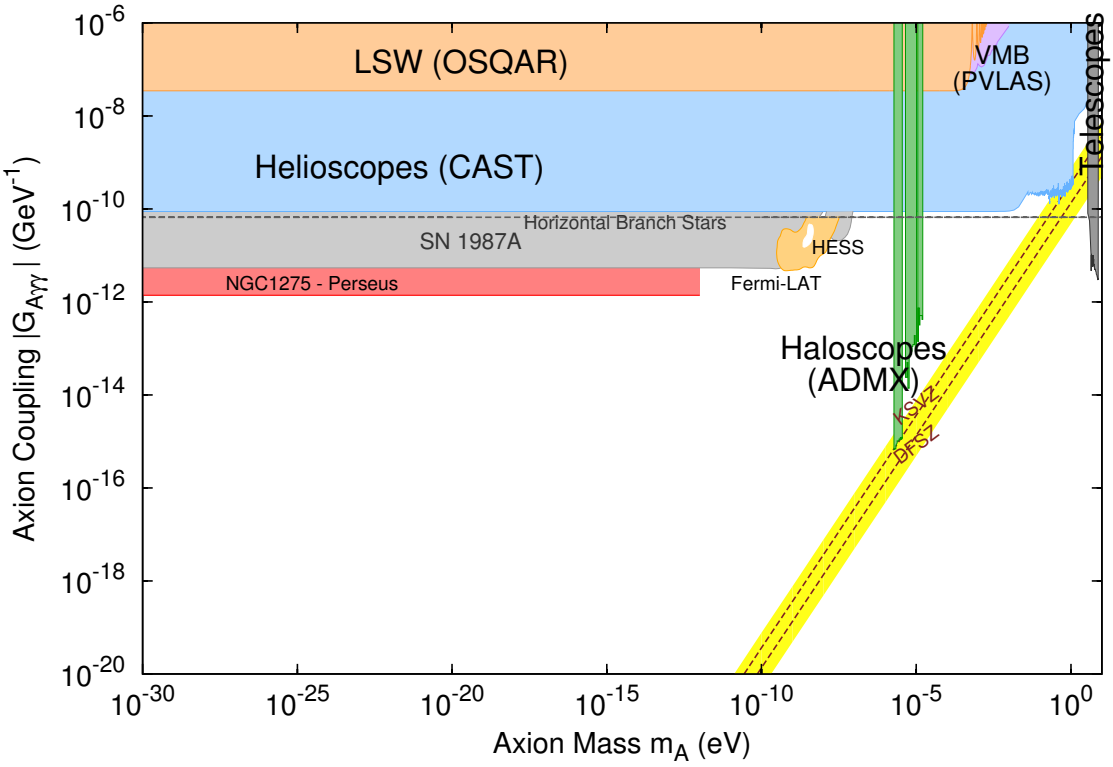

Figure 2.6: We show our bounds from NGC1275 and 2E3140 in comparison to previously obtained bounds on ALPs.

can lead to oscillatory modulations within the energy ranges probed by *Chandra* and *XMM-Newton*. Although there is uncertainty on the precise magnetic field structure along the line of sight to these sources, it is almost certainly the case that current and future X-ray observations provide a greater reach in searches for light ALPs with $m_a \lesssim 10^{-12}$eV than even the proposed dedicated experiment IAXO [85].

Previous *Chandra* observations of NGC1275 in particular already provide a dataset of extraordinary quality. Three factors contribute to this. First, *Chandra*'s angular resolution allows a large contrast between the AGN emission and cluster. Second, the existing observations are very deep, and include three independent locations of NGC1275 on the telescope. Third, it is a fortuitous fact that in one set of observations, NGC1275 was located on the edge of the chip, thereby providing a clean observation which minimises pile-up.

In this chapter we have used all observations of four point sources in or behind galaxy clusters with *Chandra* to search for spectral modulations induced by ALPs. We have used the absence of such modulations at the $\mathcal{O}(30\%)$ level to place leading bounds on ALP-photon couplings. We have placed bounds on M using four different point sources, meaning that our bounds are robust against any particular point source having a line of sight magnetic field that is abnormally good at hiding ALPs, or having an incorrectly estimated magnetic field.

At the $\mathcal{O}(10\%)$ level, there are two main modulations in the NGC1275 spectrum – one upward around 2–2.2 keV, and one downward around 3.4–3.5 keV. In this chapter, we have focused on constraints that can be placed on ALP parameter space. In chapter 5, we further discuss the dip at 3.4–3.5 keV.

The existing datasets already place powerful constraints on ALPs. Nonetheless, from the perspective of ALP physics the dataset could be substantially improved with even relatively modest further observations. NGC1275 is now brighter than it was in 2009 by a factor of two. Observations with either *XMM-Newton* in Small

Window mode or *Chandra* off-axis and in reduced frame time (to reduce pile-up) could give both a larger and cleaner dataset than the best used in this chapter, the 2009 ACIS-I edge observations. X-ray observations of galaxy clusters therefore provide an outstanding way to look for new physics beyond the Standard Model.

Chapter 3

Cosmic ALP Background Propagation in Galaxies

This chapter is based on [3].

3.1 Introduction

A primordially generated, thermally produced cosmic ALP background (CAB), analogous to the CMB, is a natural prediction of string theory models of inflation [86]. The CAB has a quasi-thermal energy spectrum that is red shifted to soft X-ray energies today. The constituent ALPs act as dark radiation - extra relativistic degrees of freedom conventionally parametrised by the equivalent excess in the number of neutrino species $\Delta N_{\rm eff}$. Current measurements of $\Delta N_{\rm eff}$ are consistent both with zero and with a significant dark radiation component [19]. The ALP number density in the CAB between energies E and $E + dE$ is:

$$dN\left(E\right) = AX\left(E\right)dE, \tag{3.1}$$

where $X(E)$ is the shape of the CAB energy spectrum and A its normalisation. The spectral shape is predicted by the general string inflation scenario described in [86], and may be found by numerically solving the Friedmann equations for ALP production and redshift. The resulting spectrum is fit well by the function

$$X(E) = E^q e^{-aE^r}. \tag{3.2}$$

The constants q, a and r are found by fitting equation (3.2) to a numerical solution of the equations of motion, and in general depend on the mean ALP energy E_{CAB}. In a typical string inflation model, $E_{\mathrm{CAB}} \sim \mathcal{O}(100\,\mathrm{eV})$. The overall normalisation of the spectrum is model dependent but may be measured by its contribution to ΔN_{eff}. We will therefore find the normalisation constant A by setting the CAB contribution to ΔN_{eff}. This is related to the CAB energy density by:

$$\rho_{\mathrm{CAB}} = \Delta N_{\mathrm{eff}} \frac{7}{8} \left(\frac{4}{11}\right)^{\frac{4}{3}} \rho_{\mathrm{CMB}}. \tag{3.3}$$

The flux $d\Phi_a(E)$ of ALPs with energies between E and $E + dE$ is then:

$$d\Phi_a(E) = dN(E)\frac{c}{4}, \tag{3.4}$$

so,

$$\frac{d\Phi_a}{dE} = AX(E)\frac{c}{4}. \tag{3.5}$$

The predicted spectrum of the CAB background for $E_{\mathrm{CAB}} = 200\,\mathrm{eV}$ and $\Delta N_{\mathrm{eff}} = 0.5$ is shown in Figure 3.1. In this case, the parameters in equation (3.2) are found to be $q = 0.62$, $r = 1.5$, $a = 2.6 \times 10^{-4}\,\mathrm{eV}^{-1.5}$.

For sufficiently large $\frac{1}{M}$ and CAB flux, ALP-photon conversion offers the possibility of detecting a CAB as an excess of soft X-ray photons from environments with a sufficiently strong and coherent magnetic field [66]. A natural place to search

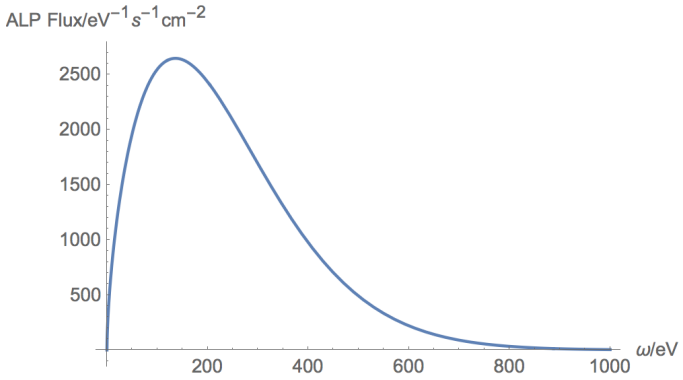

Figure 3.1: The predicted ALP flux $\frac{d\Phi_a}{dE}$ for $E_{\rm CAB} = 200\,\text{eV}$ and $\Delta N_{\rm eff} = 0.5$

for this effect is in galaxy clusters, which host $1 - 10\,\mu$G fields over Mpc distances. Furthermore, there is a long-standing excess in the soft X-ray ($E \lesssim 400\,\text{eV}$) flux observed from galaxy clusters, above the predicted thermal emission from the intra-cluster medium. It was suggested in [66] that CAB to photon conversion in galaxy clusters could be the source of this soft X-ray excess. Detailed simulations of this process have been carried out for the Coma [68, 87], A665, A2199 and A2255 [88] galaxy clusters. These show that CAB to photon conversion can consistently explain the observed excess in Coma, A2199 and A2255 as well as the non-observation of an excess in A665, within astrophysical uncertainties.

While by no means conclusive, this hint of new physics motivates studying the consequences of a CAB in other astrophysical systems. Galaxies also host magnetic fields and are therefore potential ALP to photon converters, as discussed in [4, 5, 52, 54, 56, 89–92]. ALPs from a CAB may convert to X-ray photons in the Milky Way. This would contribute to the unresolved cosmic X-ray background - the diffuse X-ray intensity observed across the sky after subtracting the integrated emission from all detected point sources. Within standard physics, the unresolved cosmic X-ray background could arise from the Local Bubble and the warm-hot intergalactic medium [93, 94]. There is also room for more exotic contributions, such as decaying dark matter or the CAB considered here. However, unlike in the case of the galaxy

cluster soft X-ray excess, there is no problem explaining the cosmic X-ray background within the framework of standard physics. The possibility that the cosmic X-ray background is related to conversion of a CAB to photons in the Milky Way's magnetic field was first considered in [66, 92].

The magnetic field in a starburst galaxy (a galaxy with a very high rate of star formation) is typically an order of magnitude higher than that in the Milky Way, suggesting a substantially higher rate of ALP-photon conversion. We therefore also estimate the ALP to photon conversion probability in starburst galaxies. In both cases, the warm ionized and neutral gas in the galaxy also plays a significant role in determining the ALP to photon conversion probability, as discussed in sections 3.2 and 3.5.

In this chapter, we will discuss the phenomenology and potential observational consequences of a CAB's passage through the Milky Way. We will also consider ALP to photon conversion in the high magnetic field, high plasma density environment of starburst galaxies. In section 3.2, we describe our model of the Milky Way environment. In section 3.3, we present and discuss our results for ALP-photon conversion in the Milky Way. In section 3.4, we discuss some caveats and additional relevant effects. In particular we derive the conditions under which the clumpiness of the warm ionized gas in galaxies becomes relevant for ALP-photon conversion. In section 3.5 we apply this to estimate the ALP-photon conversion probability in starburst galaxies. We conclude in section 3.6.

3.2 The Milky Way Environment

We simulate the ALP to photon conversion probability using the density matrix formalism described in equations (1.22), (1.23) and (1.24). We discretize each line of

sight into domains of length δz:

$$\rho_k = e^{-iH_k\delta z}\rho_{k-1}e^{iH_k^\dagger\delta z}, \tag{3.6}$$

where ρ_k is the density matrix in the kth domain and H_k is the Hamiltonian defined using the magnetic field, electron density and neutral hydrogen density in the centre of the kth domain.

Three properties of the Milky Way's interstellar medium are relevant to ALP-photon conversion - the magnetic field, the free electron density provided by the warm ionized medium and the opacity to X-rays provided by the warm neutral medium. In this section, we describe our model for each of these components. We leave a discussion of various caveats to and justifications of this model, in particular the clumpiness of the electron density, to section 3.4.

3.2.1 Magnetic field

We use the recent model by Jansson and Farrar [62,63], based on 40,000 extra-galactic Faraday rotation measures. The magnetic field is the sum of three components - the coherent field, the random field and the striated field. The coherent field has large scale structure on the scale of the Milky Way with typical field strengths of a few μG. The origin of such large scale fields in galaxies is not well understood. They may be generated when a small seed field, for example from plasma fluctuations, is amplified and ordered by the dynamo mechanism [95]. In this scenario, large scale rotation or turbulent motion of the plasma are transferred into magnetic energy. The coherent field is modeled as the sum of a disc field, which follows the spiral arms of the Milky Way; a halo field above and below the disc; and an 'X field' which points out of the plane of the Milky Way. The radial extent of the halo field is much greater in the

South of the galaxy than in the North. The coherent field model in [62] artificially excludes the central 1 kpc of the Milky Way. We therefore augment the model with a 5 μG radially constant poloidal field with vertical scale height 1 kpc in the central 1 kpc only. A full sky map of the average coherent field is shown in Figure 3.2.

The random field has a set magnitude with a disc and halo component, but its direction is randomized with a coherence length of $\mathcal{O}(100\,\mathrm{pc})$. Randomly directed magnetic fields arise in galaxies from supernovae outflows and hydrodynamic turbulence. The magnitude of the random field is typically a few times higher than that of the coherent field. The striated field has a magnitude 1.2 times that of the coherent field with its sign randomized on coherence scales of $\mathcal{O}(100\,\mathrm{pc})$. This field structure is generated when magnetized gas is subject to shear and compression [96]. We see from equation (1.20) that the conversion probability increases with the coherence length of the magnetic field. Indeed, for the majority of the Milky Way the coherent field gives the dominant contribution to ALP-photon conversion. The exception to this is in the disc of the Milky Way, where the random field is $\mathcal{O}(10\,\mu\mathrm{G})$ whereas the coherent field is $\mathcal{O}(1\,\mu\mathrm{G})$. Additionally, the coherent field often reverses sign between the spiral arms, decreasing its coherence length in the disc. We therefore use all three field components in modeling ALP-photon conversion in the Milky Way. The random and striated fields are implemented with respect to each line of sight - the direction and sign respectively are randomised every 100 pc along each ALP-photon path separately. This simple implementation clearly does not give a realistic picture of the random and striated fields across the Milky Way, but is adequate for modeling their effects on ALP-photon conversion.

3.2.2 Electron density

As described above, the photon gains an effective mass through interactions with surrounding free electrons. This mass suppresses ALP-photon conversion, as shown

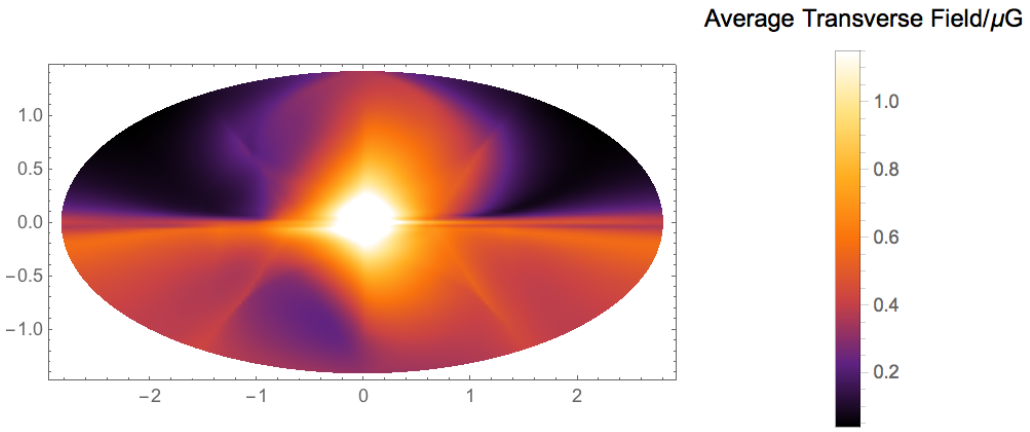

Figure 3.2: The average coherent transverse magnetic field for lines of sight starting 20 kpc from the Earth. Galactic latitude increases vertically in the plot, while galactic longitude increases to the right. The centre of the plot corresponds to a line of sight in the direction of the galactic centre.

in equations (1.15) and (1.20). We use the thin and thick disc components of the NE2001 [64] model of the Milky Way electron density:

$$\begin{aligned} g_{\text{thick}}(r) &= \frac{\cos\left(\frac{\pi r}{34\,\text{kpc}}\right)}{\cos\left(\frac{\pi R_\odot}{34\,\text{kpc}}\right)} H(17\,\text{kpc} - r), \\ g_{\text{thin}}(r) &= \text{e}^{-\left(\frac{r-3.7\,\text{kpc}}{1.8\,\text{kpc}}\right)^2}, \\ n_{\text{thick}}(r,z) &= 0.035\,\text{cm}^{-3} g_{\text{thick}}(r)\,\text{sech}^2\left(\frac{z}{0.95\,\text{kpc}}\right), \\ n_{\text{thin}}(r,z) &= 0.09\,\text{cm}^{-3} g_{\text{thin}}(r)\,\text{sech}^2\left(\frac{z}{0.14\,\text{kpc}}\right), \\ n_e(r,z) &= n_{\text{thick}}(r,z) + n_{\text{thin}}(r,z), \end{aligned} \tag{3.7}$$

where (r, z) are cylindrical polar coordinates centred at the galactic centre, $R_\odot = 8.5\,\text{kpc}$ is the distance to the Sun and $H(x)$ is the Heaviside step function. This model predicts unphysically low electron densities at large radii. While this is not important for many astrophysical phenomena, which depend only on line of sight integrals of n_e, it can have a large effect on $P_{a\to\gamma}$. We therefore enforce a minimum electron density of $n_{\text{min}} = 10^{-7}\,\text{cm}^{-3}$, approximately the electron density of inter-

galactic space.

3.2.3 Photoelectric absorption by the warm neutral medium

As explained in chapter 1, we model photoelectric absorption with the damping parameter Γ, which describes the attenuation of the photon component of the ALP-photon vector. This is conventionally parameterzied by the effective cross section with respect to neutral hydrogen, so that $\Gamma(\omega) = \sigma_{\text{eff}}(\omega)(n_{HI} + 2n_{H_2})$, where $n_{HI} + 2n_{H_2}$ is the density of neutral hydrogen. (HI refers to atomic hydrogen and H_2 to molecular hydrogen.) Photoelectric absorption by heavier elements (which is dominant for $\omega \gtrsim 1\,\text{keV}$) is included in the effective cross section $\sigma_{\text{eff}}(\omega)$ by assuming solar abundances for the relative densities of hydrogen and heavier elements. We use effective cross section values from [97] - we note in particular that $\sigma_{\text{eff}}(\omega)$ is highly energy dependent, ranging from $\sigma_{\text{eff}}(100\,\text{eV}) = 5.7\times10^{-20}\,\text{cm}^2$ to $\sigma_{\text{eff}}(2\,\text{keV}) = 4.3\times10^{-23}\,\text{cm}^2$. We use the neutral hydrogen densities given in [98]:

$$n_{HI} = \begin{cases} 0.32\,\text{cm}^{-3}\text{exp}\left(-\frac{r}{18.24\,\text{kpc}} - \frac{|z|}{0.52\,\text{kpc}}\right), & \text{if } r \geq 2.75\,\text{kpc} \\ 0, & \text{otherwise} \end{cases} \tag{3.8}$$

$$n_{H_2} = 4.06\,\text{cm}^{-3}\text{exp}\left(-\frac{r}{2.57\,\text{kpc}} - \frac{|\,z\,|}{0.08\,\text{kpc}}\right). \tag{3.9}$$

3.3 The Milky Way: Results and Discussion

We now apply equations (1.22) and (3.6) to the conversion of a cosmic ALP background to photons in the Milky Way.

3.3.1 Conversion probabilities

The Milky Way ALP to photon conversion probability at a range of soft X-ray energies is shown in Figures 3.3, 3.4 and 3.5. We use a fiducial value of $M = 10^{13}\,\text{GeV}$. We see that at $\omega = 200\,\text{eV}$, $P_{a\to\gamma}$ is heavily suppressed by photoelectric absorption but this suppression is not significant at $\omega = 500\,\text{eV}$ and $\omega = 1500\,\text{eV}$, where $P_{a\to\gamma}$ inherits the geometry of the galactic magnetic field.

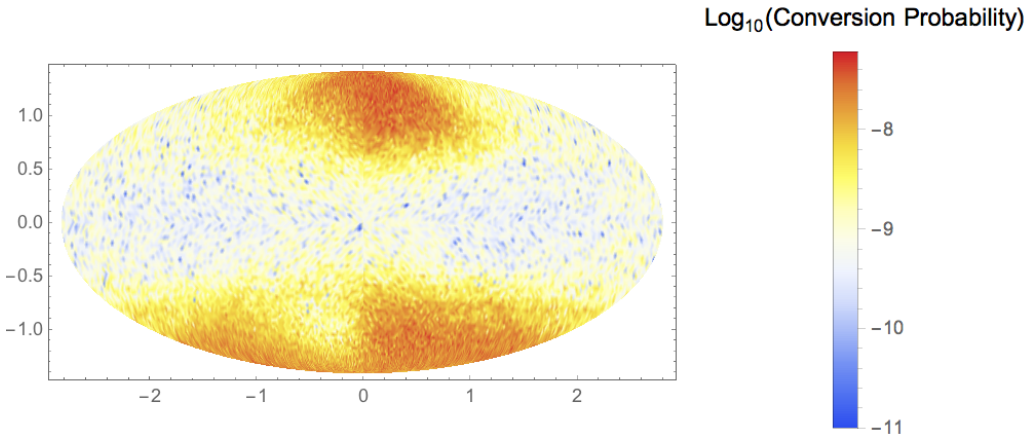

Figure 3.3: The ALP to photon conversion probability in the Milky Way for ALP energy $\omega = 200\,\text{eV}$ and $M = 10^{13}\,\text{GeV}$.

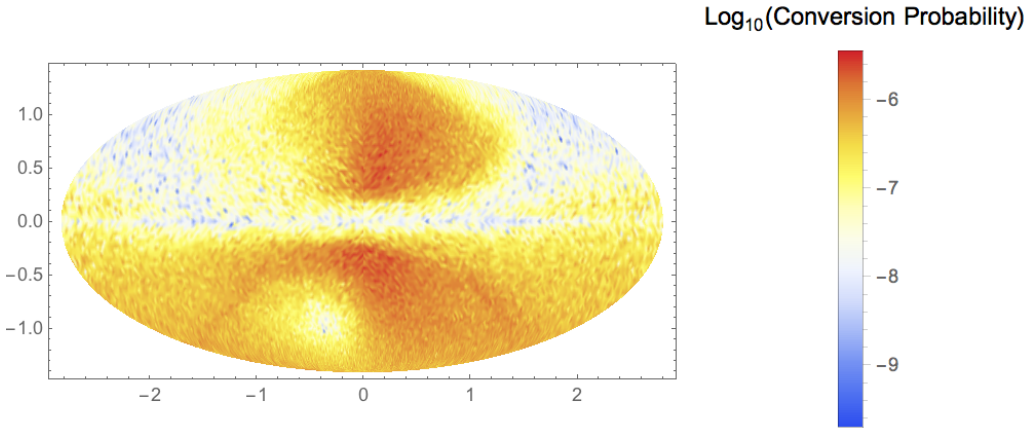

Figure 3.4: The ALP to photon conversion probability in the Milky Way for ALP energy $\omega = 500\,\text{eV}$ and $M = 10^{13}\,\text{GeV}$.

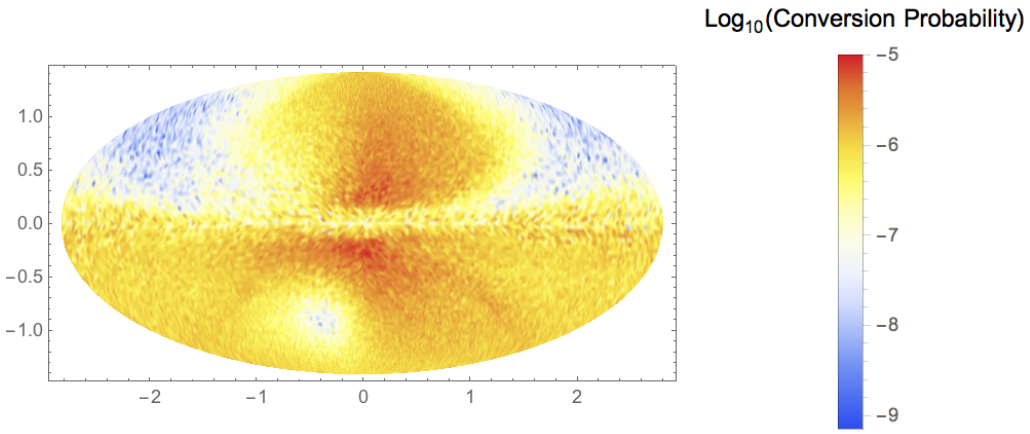

Figure 3.5: The ALP to photon conversion probability in the Milky Way for ALP energy $\omega = 1500\,\text{eV}$ and $M = 10^{13}\,\text{GeV}$.

3.3.2 Application to a cosmic ALP background

A cosmic ALP background would convert to photons in astrophysical magnetic fields leading to a potentially observable soft X-ray flux. This effect has been suggested as the source of the soft X-ray excess in galaxy clusters. The ALP to photon conversion probability in the Milky Way is around 3 orders of magnitude lower than that in galaxy clusters, primarily due to the Milky Way's smaller size. We therefore do not expect such a strong signal from CAB to photon conversion in the Milky Way. Any extra soft X-ray photons generated from a CAB's passage through the Milky Way would contribute to the unresolved cosmic X-ray background - the diffuse soft X-ray flux remaining after subtracting the flux from known point sources.

The photon flux from a CAB in a solid angle Ω is given by:

$$\frac{d\Phi_\Omega}{dE} = \frac{1}{2\pi}\int_\Omega d\Omega' P\left(\Omega', E\right) AX\left(E\right)\frac{c}{4}. \tag{3.10}$$

For example, for a central energy $E_{\text{CAB}} = 200\,\text{eV}$, the predicted photon fluxes for disc and halo pointings are shown in Figures 3.6 and 3.7. We normalise to $\Delta N_{\text{eff}} = 0.5$ to allow easy comparison with the galaxy cluster fluxes simulated in [68]. The predicted

CAB signal scales linearly with the CAB contribution to $\Delta N_{\rm eff}$. We notice that the shape of the spectrum is dramatically altered from the CAB spectrum shown in Figure 3.1, as the conversion probability at low energies is dramatically suppressed by photo-electric absorption. The spectrum is further influenced by the energy dependence of the conversion probability even in the absence of absorption. For example, for both pointings we see oscillations in the predicted flux on top of the overall shape of the spectrum. These can be understood by considering the analytic solution in equation (1.19), which approximates the qualitative features of the solution in the non-homogeneous case simulated here. In particular, we expect to see local maxima in the conversion probability whenever $\Delta = 0.053 \times \left(\frac{n_e}{10^{-3}\,\mathrm{cm}^{-3}}\right)\left(\frac{1\,\mathrm{keV}}{\omega}\right)\left(\frac{L}{1\,\mathrm{kpc}}\right) = \frac{N\pi}{2}$ for odd integer N. These correspond to the oscillations seen in Figures 3.6 and 3.7 and are a distinctive feature of a photon flux arising from ALP to photon conversion in a sufficiently high electron density environment (so that $\Delta > 1$). The flux from the Milky Way centre (Figure 3.6) is lower and peaks at higher energies that that from due Galactic North (Figure 3.7) due to the higher warm neutral medium column density towards the Galactic centre, leading to a greater effect from photo-electric absorption. Note that the detailed shape of the Milky Way centre spectrum is highly dependent on the realisation of the strong random magnetic field in the disc.

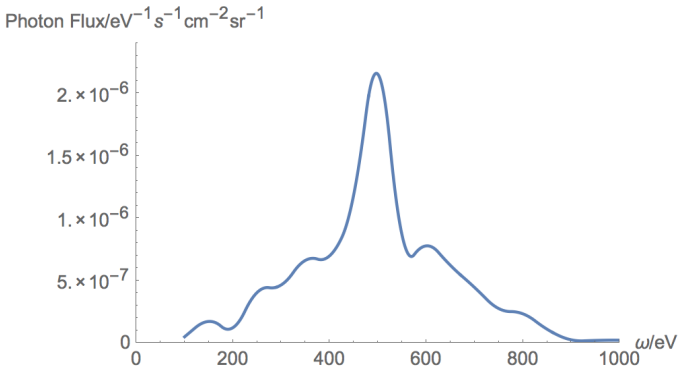

Figure 3.6: The predicted photon flux from the Milky Way centre from CAB to photon conversion with $E_{\rm CAB} = 200\,\mathrm{eV}$ and $M = 10^{13}\,\mathrm{GeV}$

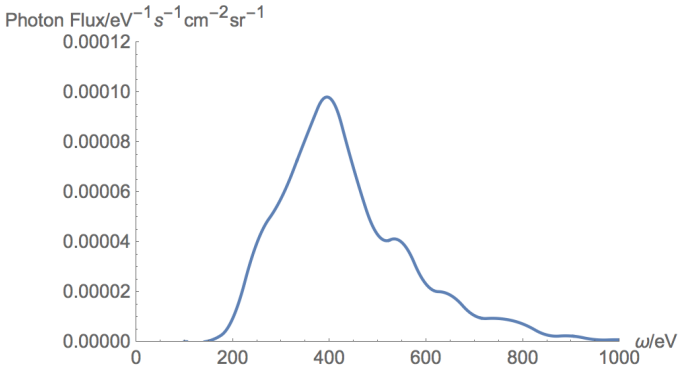

Figure 3.7: The predicted photon flux from due Galactic North from CAB to photon conversion with $E_{\mathrm{CAB}} = 200\,\mathrm{eV}$ and $M = 10^{13}\,\mathrm{GeV}$

Full sky maps of the cosmic X-ray background were observed by the ROSAT satellite [99]. We now calculate the predicted flux from a CAB in the ROSAT 1/4 keV and 3/4 keV bands. We use equation (3.10) with the conversion probabilities calculated using equation (3.6). As shown in [68, 87, 88], natural CAB parameters to explain the cluster soft excess are $E_{\mathrm{CAB}} = 200\,\mathrm{eV}$ and $M = 5 \times 10^{12}\,\mathrm{GeV}$ for $\Delta N_{\mathrm{eff}} = 0.5$. We plot the predicted ROSAT signals for these parameters as full sky maps in Figures 3.8 and 3.9. Comparing with [99], we find that the predicted CAB signal is over 3 orders of magnitude smaller than the signal observed by ROSAT. Typical values of the X-ray fluxes observed by ROSAT and predicted by the CAB are shown in table 3.1. The soft X-ray excess can also be explained with a lower E_{CAB} and lower M - in this case the signal in the Milky Way is even lower due to the higher photo-electric absorption at lower energies.

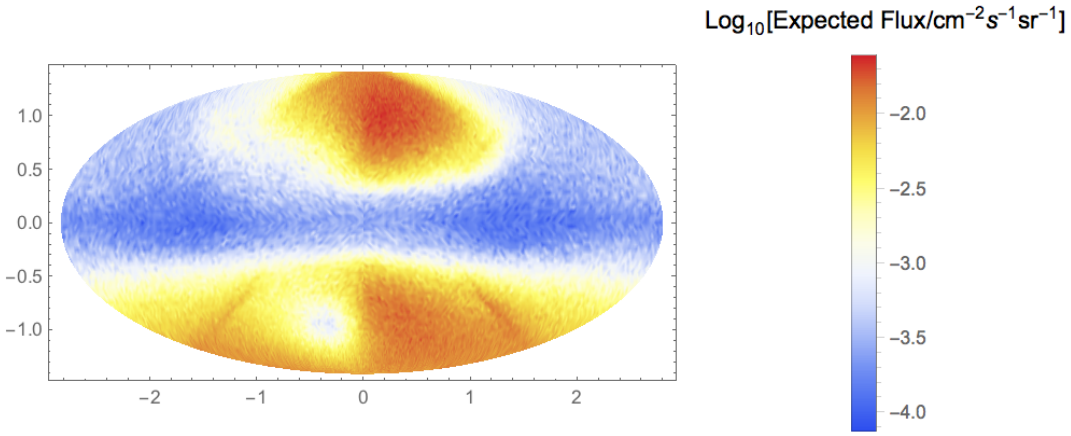

Figure 3.8: The predicted photon flux in the ROSAT 1/4 keV band for $E_{\mathrm{CAB}} = 200\,\mathrm{eV}$, $M = 5 \times 10^{12}\,\mathrm{GeV}$ and $\Delta N_{\mathrm{eff}} = 0.5$

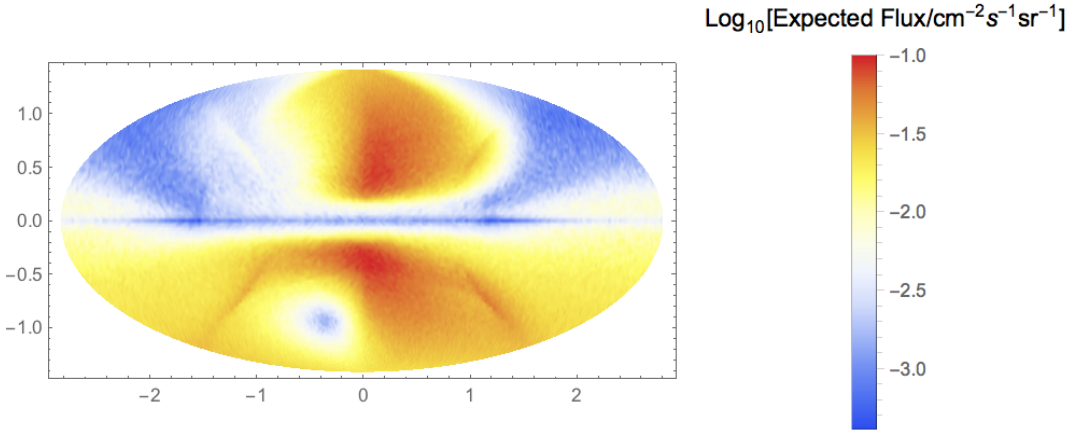

Figure 3.9: The predicted photon flux in the ROSAT 3/4 keV band for $E_{\mathrm{CAB}} = 200\,\mathrm{eV}$, $M = 5 \times 10^{12}\,\mathrm{GeV}$ and $\Delta N_{\mathrm{eff}} = 0.5$

	CAB Prediction	ROSAT observed
1/4 keV band; halo	10^{-2}	10^{2}
1/4 keV band; disk	$10^{-3.5}$	10
3/4 keV band; halo	$10^{-1.5}$	10
3/4 keV band; disk	10^{-3}	10

Table 3.1: Typical fluxes in the Milky Way halo and disk predicted by a CAB with $E_{\mathrm{CAB}} = 200\,\mathrm{eV}$, $M = 5 \times 10^{12}\,\mathrm{GeV}$ and $\Delta N_{\mathrm{eff}} = 0.5$ (see figures 3.8 and 3.9), and observed by ROSAT [99] in the 1/4 and 3/4 keV bands. Fluxes are given in units of $\mathrm{cm}^{-2}\,\mathrm{s}^{-1}\,\mathrm{sr}^{-1}$, and we take the effective area of ROSAT as $100\,\mathrm{cm}^2$.

We might wonder if a CAB with different parameters could contribute significantly to the cosmic X-ray background (quite possibly by ignoring the problem of overproduction in clusters). The cosmic X-ray background is most clearly seen in the Chandra Deep Field (CDF) observations [93]. The observed fluxes, ALP to photon conversion probabilities and predicted fluxes from CAB to photon conversion (with the parameters used above) for the CDF-South and CDF-North observations are shown in table 3.2. To simulate the conversion probabilities here, we did not include the effects of photo-electric absorption, as the CDF pointings are chosen for their low warm neutral medium column density. For any CAB parameter values we expect the CAB signal from CDF-North to be $\mathcal{O}(10)$ times lower than that from CDF-South. However, the cosmic X-ray background intensities from these observations are the same within their errors. Therefore the possibility of a CAB forming the dominant part of the cosmic X-ray background is excluded by the North-South asymmetry of the Milky Way magnetic field.

	(b, l)	$P_{a\to\gamma}$	Predicted Flux	Observed Flux
CDF-South	$(-22.8°, 161°)$	2.4×10^{-6}	2.4×10^{-15}	$(1.1 \pm 0.2) \times 10^{-12}$
CDF-North	$(54.8°, 125.9°)$	2.5×10^{-7}	2.0×10^{-16}	$(9 \pm 3) \times 10^{-13}$

Table 3.2: The ALP to photon conversion probabilities $P_{a\to\gamma}$ (averaged over the energy range), predicted CAB fluxes and observed cosmic X-ray background fluxes after point source subtraction for the Chandra Deep Field pointings. Fluxes are given in units of $\mathrm{ergs\,cm^{-2}\,s^{-1}\,deg^{-2}}$. We also show the galactic latitude b and longitude l of the observations. We use $E_{\mathrm{CAB}} = 200\,\mathrm{eV}$, $M = 5 \times 10^{12}\,\mathrm{GeV}$ and $\Delta N_{\mathrm{eff}} = 0.5$.

We see that a CAB responsible for the cluster soft X-ray excess would currently be unobservable in the Milky Way, and that a CAB cannot contribute significantly to the observed unresolved cosmic X-ray background without giving it a North-South asymmetry ruled out by observations. Ubiquitous features of a CAB Milky Way signal are a prominent North-South asymmetry (as shown in Figures 3.8 and 3.9), and complex spectral shapes from a convolution of the quasi-thermal CAB spectrum and the energy dependent conversion probability as shown in Figures 3.6 and 3.7. In

particular, the conversion probability and therefore the predicted flux oscillates as the energy increases.

3.4 Additional Effects

3.4.1 Milky Way magnetic field

We have used a simplistic model for the random and striated fields with a single coherence length of 100 pc. In reality, we expect these fields to exhibit a range of coherence scales. However, changing the coherence length by a factor of 10 in either direction only results in a factor of $\lesssim 2$ difference in the full conversion probability. Furthermore, we have not considered the field at the very centre of the Milky Way. ALP to photon conversion in the Milky Way centre is discussed in [5] in the context of the 3.5 keV line. Here we simply note that estimates of the magnetic field in the Galactic centre are highly uncertain, ranging from $10\,\mu$G to 1 mG. At the upper end of this field range, we could see conversion probabilities in the Milky Way centre comparable to those in galaxy clusters, and therefore might expect an observable soft X-ray flux from a CAB. However, the high density of the warm neutral medium in the Galactic centre would significantly suppress the signal at low energies. Furthermore, the galactic centre is a highly complex environment so it would be very difficult to pick out a small excess soft X-ray flux.

3.4.2 Clumpiness of the interstellar medium

We recall that the electron density of the surrounding medium suppresses ALP-photon conversion by giving an effective mass to the photon, as shown in equations (1.14), (1.15), (1.20) and (1.21). The electron density model used to simulate ALP-photon conversion describes the smooth, *volume averaged* electron density. In reality, the warm ionized medium (WIM) in galaxies exists in high density clouds with a rather

low intercloud electron density [100]. This structure is characterized by the filling factor f, the fraction of a line of sight occupied by WIM clouds. In principle, by using the clumpy local electron density n_e we might predict a different $P_{a\to\gamma}$ than we would have by naively implementing the smooth volume averaged electron density $\overline{n}_e$. To examine the effect of the local electron density distribution, we consider the role of the electron density in rotating the probability amplitude $A(L) = \langle 1,0,0|f(L)\rangle$ in the complex plane. For simplicity, we consider the case of a constant magnetic field in the x direction, so that only x polarized photons are produced. The relevant equations are then (see equations (1.20) and (1.21)):

$$P_{a\to\gamma}(L) = \left| \int_0^L dz e^{i\varphi(z)} \frac{B_x(z)}{2M} \right|^2 , \tag{3.11}$$

where,

$$\varphi(z) = \int_0^z dz' \Delta_\gamma(z') = -\frac{1}{2\omega} \int_0^z dz' \omega_{pl}^2(z') \,, \tag{3.12}$$

with

$$\omega_{pl}^2 = 4\pi\alpha \frac{n_e}{m_e}. \tag{3.13}$$

We see that the angle of turn in the complex plane is given by $\varphi(z)$, which is linear in $n_e\,(z)$. We first note that whether this turning happens continuously or in steps does not significantly effect $P_{a\to\gamma}$. This is demonstrated in Figure 3.10, where we plot in the complex plane the probability amplitude $A(L) = \int_0^L dz e^{i\varphi(z)} \Delta_{\gamma a i}(z)$ for a propagation distance $L = 0 - 1\,\mathrm{kpc}$ increasing along the line. We use $B_\perp = 1\,\mu\mathrm{G}$, $\overline{n}_e = 0.05\,\mathrm{cm}^{-3}$, cloud size $d_c = 10\,\mathrm{pc}$, $f = 0.1$ and $\omega = 500\,\mathrm{eV}$. In the left hand plot we use the volume averaged electron density, and in the right hand plot implement the electron density in evenly spaced clouds, with an intercloud electron density of $10^{-7}\,\mathrm{cm}^{-3}$. We see that the overall shape of $A(L)$ is the same in each case, although in the volume averaged case the turn is continuous, whereas in the right hand plot we see corners (with a very high rate of turn) where there is a cloud. As expected, the

conversion probability at $L = 1\,\mathrm{kpc}$ is practically the same in each case (4.9×10^{-10} and 5.2×10^{-10} respectively for $M = 10^{13}\,\mathrm{GeV}$).

However, $e^{i\varphi(z)}$ is also *periodic* in $n_e\,(z)$, and it is in this periodicity that we see the effect of the clumpiness of the WIM. For high electron densities, low filling factors and/or low ALP energies it may be that within a single cloud $\varphi(z)$ changes by $\gtrsim 2\pi$. A cycle of $\mathrm{Arg}\left(e^{i\varphi(z)}\right)$ within a cloud that returns to its starting point does not significantly decrease the overall conversion probability. In the regime where this phenomenon occurs, the overall *large scale* turning of A in the complex plane is decreased by the organisation of the WIM into clouds. The significant ($\gtrsim 2\pi$) turning within a cloud essentially gives us a 'free lunch' - the volume averaged electron density is increased, but there is no contribution to the net large scale turning, and so the overall conversion probability is not significantly decreased. The predicted conversion probability is therefore significantly increased by taking into account the cloud structure of the WIM. This effect is demonstrated by Figure 3.11. Here we use the same parameters as in Figure 3.10, but with $\omega = 100\,\mathrm{eV}$ (so that Δ_γ is increased by a factor of 5). We now see the turns within clouds in the right hand plot, allowing $A(L)$ to reach larger radii in the complex plane, and increasing $P_{a\to\gamma}(L)$ from 3.0×10^{-11} with a smooth volume averaged WIM to 9.2×10^{-10} with a more realistic WIM profile. In spite of the very high electron density within clouds $n_c = \frac{\overline{n}_e}{f}$, the low electron density intercloud regions allow $|A(L)|$ to grow in this regime.

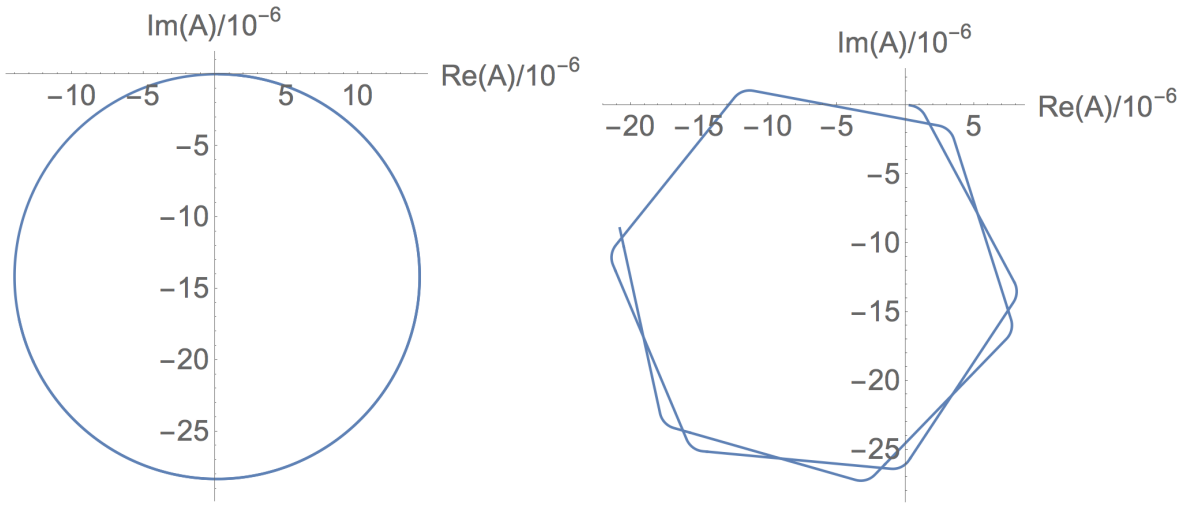

Figure 3.10: $A(L) = \int_0^L dz e^{i\varphi(z)} \Delta_{\gamma a i}(z)$ for $L = 0 - 1\,\mathrm{kpc}$ increasing along the line. In the left hand plot we use the volume averaged electron density, and in the right hand plot implement the electron density in evenly spaced clouds, with an intercloud electron density of $10^{-7}\,\mathrm{cm}^{-3}$. The clouds correspond to the 'corners' in the plot. We see that $P_{a\to\gamma} = |A|^2$ is not significantly effected by the presence of clouds. We use $B_\perp = 1\,\mu\mathrm{G}$, volume average electron density $\overline{n}_e = 0.05\mathrm{cm}^{-3}$, cloud size $d_c = 10\,\mathrm{pc}$, filling factor $f = 0.1$, $M = 10^{13}\,\mathrm{GeV}$ and $\omega = 500\,\mathrm{eV}$. For the volume averaged case, $P_{a\to\gamma}\,(L = 1\,\mathrm{kpc}) = 4.9 \times 10^{-10}$. With clouds, $P_{a\to\gamma}\,(L = 1\,\mathrm{kpc}) = 5.2 \times 10^{-10}$.

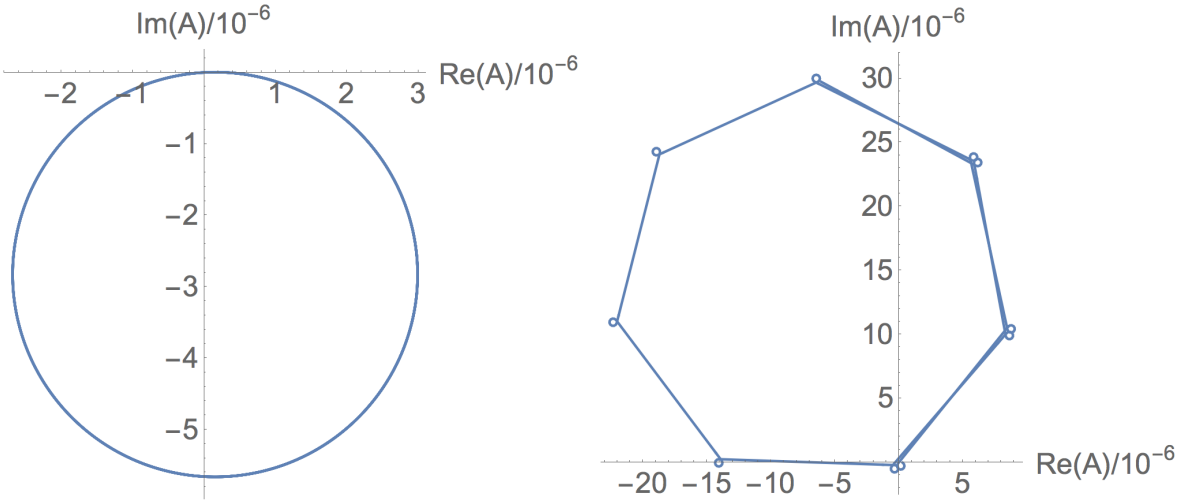

Figure 3.11: $A(L) = \int_0^L dz e^{i\varphi(z)} \Delta_{\gamma ai}(z)$ for $L = 0 - 1\,\mathrm{kpc}$ increasing along the line. In the left hand plot we use the volume averaged electron density, and in the right hand plot implement the electron density in evenly spaced clouds, with an intercloud electron density of $10^{-7}\,\mathrm{cm}^{-3}$. The clouds correspond to the loops in the plot. We see that $P_{a\to\gamma} = |A|^2$ is significantly higher when the cloud structure is taken into account. We use $B_\perp = 1\,\mu\mathrm{G}$, volume average electron density $\overline{n}_e = 0.05\mathrm{cm}^{-3}$, cloud size $d_c = 10\,\mathrm{pc}$, filling factor $f = 0.1$, $M = 10^{13}\,\mathrm{GeV}$ and $\omega = 100\,\mathrm{eV}$. For the volume averaged case, $P_{a\to\gamma}\,(L = 1\,\mathrm{kpc}) = 3.0 \times 10^{-11}$. With clouds, $P_{a\to\gamma}\,(L = 1\,\mathrm{kpc}) = 9.2 \times 10^{-10}$.

We therefore see that the condition for the cloud structure of the WIM to be significant is:

$$\delta = 1.1 \times 10^{-2} \left(\frac{n_c}{10^{-2}\,\mathrm{cm}^{-3}}\right) \left(\frac{\mathrm{keV}}{\omega}\right) \left(\frac{\text{cloud size}}{10\,\mathrm{pc}}\right) \gtrsim 2\pi. \tag{3.14}$$

In Figure 3.10 $\delta = 1.1$, whereas in Figure 3.11 $\delta = 5.5$. This condition is almost never satisfied in the Milky Way, so in this work we simply use the volume averaged electron density given in [64]. However, this effect is significant in high electron density environments such as starburst galaxies. Furthermore, an analogous effect will operate whenever oscillations are suppressed by an effective mass from astrophysical plasmas.

The warm neutral medium responsible for photoelectric absorption also has a

cloud-like structure. We find that using a clumpy rather than homogeneous warm neutral medium for Milky Way densities only has a significant effect (after averaging over cloud positions) on $P_{a\to\gamma}$ for $\omega \lesssim 200\,\mathrm{eV}$. At these energies, we found that photoelectric absorption reduces the expected signal to negligible levels in either case. We therefore simply use the volume averaged warm neutral medium densities.

3.5 Starburst Galaxies

We now consider ALP to photon conversion in starburst galaxies. Starburst galaxies host strong magnetic fields of up to $\mathcal{O}(100\,\mu\mathrm{G})$ in the core regions with somewhat lower fields in the halo [95, 101], making them potentially very good ALP to photon converters. However, the fields in starbust galaxies are largely turbulent with little or no coherent field. Furthermore, the electron density is correspondingly higher at $\mathcal{O}(100 - 1000\,\mathrm{cm}^{-3})$ [102]. Naively, we might expect this high electron density to substantially suppress $P_{a\to\gamma}$. However, in this regime the cloud structure of the WIM becomes highly significant, as shown in section 3.4. The *intercloud* electron density it also crucial here. For example, consider a simplified case with a random field $B = 150\,\mu\mathrm{G}$ over a distance of 3 kpc and coherent over 100 pc, implemented as described in section 3.3. We use a volume averaged electron density $\overline{n}_e = 1000\,\mathrm{cm}^{-3}$. Using $\omega = 1\,\mathrm{keV}$, $M = 5 \times 10^{12}\,\mathrm{GeV}$ and the constant, volume averaged electron density gives $P_{a\to\gamma} \sim 10^{-11}$, averaging over 100 instances of the random field. Now let us assume the WIM exists in 1 pc clouds (for example as in the starburst galaxy M82 [102]) with filling factor $f = 0.1$. In this case, applying equation (3.14) we obtain $\delta = 1100$ and so the presence of clouds is of great importance. If we assume an intercloud electron density of $0.1\,\mathrm{cm}^{-3}$ we obtain $P_{a\to\gamma} \sim 10^{-4}$ - a conversion probability comparable to that in galaxy clusters. However, if we assume that the intercloud electron density is $10\,\mathrm{cm}^{-3}$ we obtain $P_{a\to\gamma} \sim 10^{-7}$, rendering any signal

unobservable (although still 4 orders of magnitude higher than for a volume averaged electron density). It is therefore possible, but certainly not guaranteed, that we might see signals from a CAB in some starburst galaxies. Furthermore, at ALP energies $E \lesssim 500\,\mathrm{eV}$, any signal would by highly suppressed by photoelectric absorption. Starbursts might also be good observation targets for the 3.5 keV line arising from dark matter decay to ALPs discussed in Chapter 4.

3.6 Conclusions

We have simulated ALP to photon conversion probabilities for axion-like particles propagating through the Milky Way to Earth. We find that the cosmic axion background motivated by string models of the early universe and by the cluster soft X-ray excess would be entirely unobservable following ALP-photon conversion in the Milky Way's magnetic field. This is due to low conversion probabilities in the Milky Way relative to galaxy clusters, as well as the high photoelectric absorption cross section for the central CAB energies. Furthermore, the North-South asymmetry in this magnetic field is not reflected in observations of the unresolved cosmic X-ray background, ruling out a significant ALP contribution to the cosmic X-ray background. The smaller size of galaxies compared with galaxy clusters make them in general poorer targets for observation of ALP-photon conversion. One exception might be starburst galaxies, which feature very high magnetic fields and electron densities.

The galactic electron density suppresses conversion by giving an effective mass to the photon component, but in such high density environments the detailed local structure of the plasma must be considered. We have derived a condition for when the cloud structure of a galaxy's electron density is relevant for ALP-photon conversion. We find that in the Milky Way, and other typical spiral and elliptical galaxies, the cloud structure is not relevant. However, the cloud structure *is* relevant in high

electron density environments such as starburst galaxies. We found that when the cloud structure of the electron density is taken into account, the predicted ALP-photon conversion probability in starburst galaxies is increased by up to 8 orders of magnitude, depending on the assumed intercloud electron density.

Chapter 4

The 3.5 keV Line from ALP to Photon Conversion in Galaxies

This chapter is based on [4], written in collaboration with Joseph Conlon.

4.1 Introduction

In February 2014, two groups independently reported the discovery of an anomalous line at ~ 3.5 keV in the spectra of a range of astrophysical targets. They suggested that this line could be caused by the decay of ~ 7 keV sterile neutrino dark matter. Bulbul *et al.* [103] found a line at $3.55-3.57\pm0.03$ keV with the *XMM-Newton* X-ray telescope in a stacked spectrum of 73 galaxy clusters, and in three sub-samples of these clusters (Perseus; Centaurus, Ophiuchus and Coma; and all others). The clusters cover a range of redshifts corresponding to energy shifts from 0 to 1.2 keV. This all but rules out an instrumental origin for the 3.5 keV line, as such an instrumental line would be smeared out by the deredshifting process. The line was found with *XMM-Newton*'s MOS detector in all four samples, and with *XMM-Newton*'s PN detector in the full sample and the "all others" sample. The local significance in each instrument is $4-5\sigma$, and the line flux is around 1% of the background emission. As the line was

detected at consistent energies in two independent instruments, the *global* significance of this discovery is also $4-5\sigma$. The authors double checked their results with the *Chandra* X-ray telescope, finding the line in Perseus but not in Virgo. The upper limit from this non-detection is consistent within the dark matter decay interpretation.

The soft X-ray emission from galaxy clusters is incredibly complex, and the weakness of the 3.5 keV line flux means that any modeling uncertainties must be carefully scrutinized. In particular, the unidentified line is within 50 - 100 eV of several known faint atomic lines, whereas the detectors' energy resolution is $\sim$ 100 eV. The authors of [103] argue that the line is present even when allowing maximal freedom for all thermal emission lines to vary. They fit the cluster emission with a line free multi-temperature *apec* model (a commonly used numerical model for the emission spectrum of a collisionally ionised, diffuse thermal plasma [104]), allowing up to four temperature components. They then add atomic lines individually as Gaussian components. Twenty-eight such atomic lines are included, and their energies were allowed to vary by up to 5 eV. The allowed fluxes of the nearby K and Ar lines were based on temperature estimates from the fluxes of S and Ca lines from a clean part of the spectrum. Relative elemental abundances were assumed to track solar abundances, but allowed to increase to three times this in the fitting process. Conversely, to explain the 3.5 keV line flux with the 3.51 keV K line, the K line flux would need to be a factor of 20 above its predicted value. The results of [103] also show that the 3.5 keV line flux from Perseus is eight times stronger than expected in the dark matter decay interpretation, with a decay rate estimated from the other 72 clusters. Furthermore, approximately half of the signal from Perseus originates from its cool core region within a radius of $\sim$ 20 kpc, whereas the dark matter distribution varies over a few hundred kpc. The signal from the Centaurus and Ophiuchus clusters is also dominated by their cool cores. This morphology is in tension with the 3.5 keV line arising from dark matter decay to photons. [103] suggest that atomic lines near 3.5

keV, such as the Ar XVII dielectric recombination line at 3.62 keV, or the 3.51 keV K line could be anomalously bright in Perseus, leading to an overestimation of the 3.5 keV line flux. However, these lines would have to exceed their predicted emissivities by an order of magnitude. It is also possible that the nearby charge exchange line discussed below could be particularly strong in Perseus' core, similarly leading to an overestimation of the 3.5 keV flux in this region.

The 3.5 keV line was also detected by Boyarsky *et al.* in the *XMM-Newton* spectra of the Perseus galaxy cluster and the Andromeda galaxy (M31) [105]. This line was detected at 3.52 ± 0.02 keV by both the MOS and PN cameras, while not being observed in a blank sky data set. The combined global significance is 4.4σ. In particular, the presence of the line in a galaxy argues against a straight-forward interpretation from a known atomic line, as galaxies host very little hot gas.

Numerous other searches for the 3.5 keV line have been carried out. The highest dark matter decay flux is expected to come from the Milky Way centre. However, this region is also incredibly complex, and therefore accurately modeling the background is very challenging – even more so than in galaxy clusters. The 3.5 keV line has been observed in the galactic centre with *XMM-Newton* [106, 107], but not with *Chandra* [108]. [106] also argue that their 3.5 keV line detection in the galactic centre can be accounted for by a potassium line within systematic uncertainties. [109] found that the 3.5 keV line in the galactic centre traces the (non-trivial) morphology of nearby atomic lines, and is therefore likely to be atomic in origin. However [110] argue that this analysis strongly underestimates the effects of absorption by neutral atoms, and therefore the conclusions are called into question. More generally, the complexity of the galactic centre region makes drawing firm conclusions about the line signal from this source impossible.

Another promising target for observing the 3.5 keV line is dwarf spheroidal galax-

ies, which have a high mass-to-light ratio and no diffuse X-ray emission. [111] searched for the line in stacked observations of dwarf galaxies with *XMM-Newton*. No line was found, excluding the dark matter decay interpretation of Bulbul *et al.* at 4.1σ using standard dark matter column densities, or 3.2σ using minimal column densities. Furthermore, [112] and [113] searched for the line in a dedicated deep observation of the Draco dwarf galaxy. [112] find no evidence of such a line, ruling out the dark matter decay interpretation at the 99% confidence level. However [113] detected the 3.5 keV line at 2.3σ in the PN camera, at 1σ in the MOS2 camera and not at all in the MOS1 camera, which suffers from low statistics after losing two CCDs. Results from all three cameras are consistent within their uncertainties, and the detection is consistent with other detections of the line. The cause of the disagreement between the two groups is unknown. [114] also searched for anomalous emission lines in a stacked spectrum of over 80 galaxies with both *Chandra* and *XMM-Newton*. No anomalous line was found, ruling out a 3.5 keV dark matter decay line at a statistical significance of 11σ. However, their analysis has been questioned by [115,116] who argue that [114] do not account for line-like systematic errors that dominate in long exposures of galaxies, and that after taking this effect into account the non-detection is only in mild tension with a dark matter decay interpretation of the 3.5 keV line discoveries.

Several further line searches have also focused on galaxy clusters. Evidence of an anomalous 3.5 keV line in at least some clusters is found by [109, 110, 116–118], although the authors' interpretation of this result varies. In particular, the line is also detected with a third X-ray telescope, *Suzaku*. No evidence of anomalous line emission was reported by galaxy cluster searches [119, 120], although of these only Tamaru *et al.* [120] find an upper limit inconsistent with previous detections. This disagreement is discussed further below. Further study of the line morphology has also yielded interesting results. [109, 110, 117] reproduce the result that the 3.5 keV line flux in Perseus is anomalously high when a dark matter decay interpretation is assumed, and

that its radial profile is furthermore much too peaked towards the cluster centre. [110] argue that, notwithstanding the high flux from the core, the 3.5 keV line profile in Perseus better fits the dark matter distribution than the profile of the 6.7 keV Fe line, suggesting that its origin is dark rather than baryonic. Interestingly, [118] only detected the line in the *non*-cool core clusters they studied, but did not detect it in their sub-sample of cool core clusters (which did not include Perseus). The non-detection in the cool core clusters was consistent with dark matter decay within the uncertainties. However, it is clear that Perseus in particular is special amoung galaxy clusters for the 3.5 keV line. Our recent discovery of an anomalous *absorption*-like feature at 3.5 keV in the spectrum of Perseus' central AGN is described in chapters 2 and 5.

Recently, the *Hitomi* collaboration argued that their observations of the centre of Perseus rule out the presence of the 3.5 keV line there at the 99% confidence level [74]. However, *Hitomi* only observed Perseus for 7% of the observation time needed to discover the line – the strong inconsistency between the *Hitomi* spectrum and the *XMM-Newton*, *Chandra* and *Suzaku* spectra is in fact driven by a 2σ *dip* at 3.5 keV present in the *Hitomi* spectrum. This dip is present only in the early observations of Perseus, and is not present in observations taken a week later. This suggests it could be either a statistical fluctuation or an instrumental effect which disappeared as the detector cooled. The other key difference between *Hitomi* and the CCD detectors is that *Hitomi*'s angular resolution is insufficient to separate the cluster's emission from the emission of its central AGN. This means that, unlike in other 3.5 keV line searches, *Hitomi* measures the sum of AGN and cluster emission. *Hitomi* would therefore be sensitive to a 3.5 keV line in the cluster emission and our recently discovered 3.5 keV dip in the AGN emission. This is discussed further in chapter 5.

The final target for 3.5 keV line searches is the Milky Way halo. [121] find no evi-

dence for an anomalous line in *Suzaku* observations of the halo, in mild tension with a dark matter decay interpretation of the line. [122] report an 11σ detection of a 3.5 keV line in the Milky Way halo with *NuStar*. Previous analysis of *NuStar* data [123] attributed the line to a solar origin. However, [122] find that the line flux does not disappear or decrease in observations including no solar flux, so this interpretation is unlikely. The lower cut-off of *NuStar*'s energy range is 3 keV, and therefore [122] consider that their 3.5 keV line could be instrumental. [122] also find a line at 4.7 keV at 9.8σ which they are unable to account for. Deep *Chandra* observations of the Milky Way halo also show evidence of a 3.5 keV line at 3σ [124]. This line could also be interpreted as the 6.4 keV Fe line from accretion onto black holes at redshifts $z \sim 0.8$. In summary, there is some evidence for the 3.5 keV line in the Milky Way halo, although it has not been detected as conclusively as in galaxy clusters.

We must carefully consider plausible non-dark matter interpretations of the 3.5 keV line. The line has been observed with 3 different telescopes at a range of redshifts, and so we can rule out an instrumental interpretation. However, the region around 3.5 keV in galaxy clusters is crowded with atomic lines, and mis-modeling this region could generate spurious line-like residuals.

Of particular concern are the K XVIII lines at 3.48 and 3.52 keV. The flux of these lines may be estimated by determining the temperature structure of the intra-cluster medium, using the relative fluxes of other atomic lines, and assuming solar relative abundances of elements. This approach was followed by Bulbul *et al.* in [103], who also allowed the fluxes to vary to up to 3 times their predicted values. However, Jeltama and Profumo [106] argue that Bulbul *et al.*'s modeling is biased towards higher temperatures, where the emissivity of the potassium lines near 3.5 keV is suppressed. They find that all emission at 3.5 keV can be accounted for by potassium with an abundance less than 3 times that expected from solar abundances if the cluster

plasma contains a significant component with $kT < 3$ keV. Further, they point out that the Ca XX to Ca XIX line ratios quoted by Bulbul *et al.* do indeed indicate temperatures $kT < 3$ keV. In [110,125], Bulbul *et al.* point out that they use fluxes of both Ca *and* S lines to estimate the K XVIII emissivity, which ensures that it has not been underestimated. Further, they reiterate that the relative strength of the K XVIII line to the new 3.5 keV line is not the central question, but rather whether the fit indicates the existence of a new line once other atomic lines have been conservatively added. The new line is only not required if the K XVIII line and Ar XVII DR line are allowed to take fluxes much greater than predicted. Conversely, Jeltama and Profumo, as well as Urban *et al.* in [117], argue that our current understanding of the intra-cluster medium does not proclude such variation in atomic emissivities. It is further noted in [126] that the potassium abundance in the solar corona is much higher than that in the photosphere. The mechanism for this amplification is not known, but if a similar mechanism were at play in the intra-cluster medium the potassium abundance could account for the 3.5 keV line. The key disagreement here is in how conservatively we must allow known atomic lines to vary – at the energy resolution of current X-ray telescopes, this question is not resolvable. However, explanations from nearby atomic lines are not good explanations for the possible 3.5 keV line detections in M31, Draco and the Milky Way halo, as these objects do not contain significant hot gas. Furthermore, Hitomi observations of the centre of Perseus [74] show no overabundance in the potassium emissivity, so this explanation is no longer plausible for this region.

Another possible contribution to emission at 3.5 keV is charge exchange with sulphur ions [127, 128]. Charge exchange (CX) is a non-equilibrium process in which neutral atoms may donate electrons to ions. The donated electrons populate high energy levels which are not significantly populated in a thermal plasma, and therefore greatly enhance the flux of lines starting at these high levels. S XVI transitions from

$n \geq 9$ levels to the ground state have energies around 3.45 keV, and may therefore contribute to the 3.5 keV flux. [127] find that these lines appear as a broad excess between 3.4 and 3.6 keV when convolved with the CCD energy resolution. In [103], Bulbul *et al.* argue that, due to its large cross section, CX only occurs in thin sheets, and therefore is not a significant effect. They also predict that CX would create other lines that are not detected. Current modeling of the intra-cluster medium, including that used in 3.5 keV line searches, does not include CX processes - more detailed analysis is needed to ascertain the CX contribution to cluster spectra.

Systematic problems in the fitting process could also give rise to erroneous line detections. For example, Jeltama and Profumo [106] conducted a line search in the Tycho supernova remnant using the same procedure as for the Milky Way centre, and found evidence for a 3.5 keV line. This line cannot have a dark matter origin, as there is not a significant dark matter column density in this direction. This could suggest systematic problems leading to spurious weak line detections. They argue that the line detection in M31 by Boyarsky *et al.* employs too large a fitting range (2 - 8 keV), such that the fit is complicated by astrophysical and instrumental lines, leading to an unphysical residual at 3.5 keV. Using a narrower fitting range (3 - 4 keV), they find only 1σ evidence for the line in M31. Boyarsky *et al.* [129] respond that M31's continuum emission is well fit by a power law in their range, and fitting only over 3 - 4 keV naturally reduced the significance of any line detection due to worse statistics. With regards to modeling the background emission in clusters, Tamura *et al.* [120] note that the area around 3.5 keV contains fewer atomic lines than the rest of the fitting range. They argue that Bulbul *et al.* could have overestimated the contribution of atomic lines to the background flux, and therefore underestimated the normalisation of the continuum thermal emission, leading to a spurious residual at 3.5 keV, in the absence of atomic lines here. The many closely spaced atomic lines cannot by resolved by CCD detectors, and so we cannot rule out this interpretation

with current data. Tamura *et al.* include far fewer atomic lines in their analysis, and do not detect the 3.5 keV line. [110] respond that Tamarua *et al.*'s less complete line modeling results in a much worse reduced chi squared (1.72 vs 1.1) for their fit of *Suzaku*'s spectrum of Perseus. Their fit contains residuals larger than the expected 3.5 keV line flux, and therefore detecting the 3.5 keV line would not be possible.

We summarise in table 4.1 some of the evidence for and against the 3.5 keV in different systems.

Object	Status of 3.5 keV line
Galaxy clusters	Detected with *XMM-Newton*, *Chandra* and *Suzaku* in several galaxy clusters and stacked samples. $4-5\sigma$ significance in stacked cluster sample. Could also be explained by mis-modelling of atomic lines or sulphur charge exchange.
Perseus galaxy cluster core	3.5 keV line flux anomalously strong for DM decay to photons. This is natural in some DM models, and for astrophysical explanations.
Draco dwarf galaxy	A disputed detection at 2.3σ with *XMM-Newton*. The cause of the dispute is unknown.
Andromeda galaxy	Detected at 3.2σ with *XMM-Newton*. This detection is disputed due to disagreement in the appropriate fitting range.
Stacked galaxies	No detection, with the dark matter decay to photons interpretation excluded at 11σ. This exclusion is disputed due possible line-like systematic errors.
Milky Way halo	Detected at 11σ with *NuStar*, although this is assumed to be an instrumental effect. Detected at 3σ with *Chandra*. This could also be interpretation as a redshifted iron line.

Table 4.1: A summary of the status of the 3.5 keV line in different objects.

The complexity of X-ray line searches is greatly heightened by the poor energy resolution of the current generation of X-ray telescopes, $\Delta E \sim 100$ eV. This is far greater than the velocity broadening for both dark and baryonic emission lines. Next generation telescopes such as *Athena* will boast a far superior resolution of order a

few eV, allowing us to resolve the 3.5 keV line exactly, and hence determine its origin.

The possibility that the 3.5 keV line arises from dark matter has generated a colossal model building effort. We focus in this chapter on the possibility considered in [130] that the line arises from dark matter decay to an ALP, which subsequently converts to a photon in astrophysical magnetic fields. This process of DM $\to a \to \gamma$ can explain morphological features of the signal of [103] that are inconsistent with the direct decay of dark matter to photons [130]. For example, in [103] the signal from Perseus was found to be much stronger than for the stacked sample of distant clusters, and within Perseus *XMM-Newton* and *Chandra* and *Suzaku* data show that the signal peaks sharply in the central cool core region of the cluster, whereas the dark matter distribution is much broader. Furthermore, as discussed above, with few exceptions the line has not been found in observations of galaxies. This non-observation is also predicted by the DM $\to a \to \gamma$ scenario.

The underlying physical reason for this is that an $a \to \gamma$ conversion probability is determined by the square of the magnetic field transverse to the direction of travel, and is thus enhanced in regions of high magnetic field. While Faraday Rotation Measure (RM) studies show that clusters generally have magnetic fields of $O(\mu\text{G})$, this can vary by a factor of a few both between clusters and within a cluster. RM studies also show significantly enhanced magnetic fields in the central regions of cool core clusters such as Perseus. This scenario therefore predicts an enhanced signal in the centre of cool core clusters, consistent with the current data. More generally, [130] predicts that in the DM $\to a \to \gamma$ scenario we expect that the inferred dark matter decay rate (if direct decay to photons is assumed) will vary from cluster to cluster, and will be much smaller in galaxies. [130] also discusses possible model building directions for dark matter decaying to ALPs. For example, moduli dark matter Φ can decay to ALPs via the kinetic coupling $\mathcal{L} \supset \frac{\Phi}{\Lambda}\partial_\mu a \partial^\mu a$. The required light moduli can arise, for example, in a LARGE volume scenario string model [131].

In this chapter we calculate the strength and morphology of the resulting 3.5 keV photon line from the Milky Way's dark matter halo decay. As the 3.5 keV line has also been observed in M31, we also discuss the M31 magnetic field and the expected strength of the resulting signal. Finally, we discuss the potential for detecting the 3.5 keV line in stacked samples of galaxies. In sections 4.2 and 4.3 we summarise the relevant properties of ALPs and the Milky Way. In section 4.4 we describe results for both the Milky Way and M31. In section 4.5 we discuss the signal in a general stacked sample of galaxies, and in section 4.6 we conclude.

4.2 The $DM \to a \to \gamma$ Scenario

The model we analyse here assumes that dark matter decays to produce a monoenergetic ALP of energy 3.5 keV [130], and with negligible mass. This can arise either from a decay $\psi \to \chi a$, where ψ is the parent dark matter particle, χ is some daughter particle and a is the axion-like particle, or from a decay to $\psi \to aa$, which produces two ALPs. The expected line signal from ALPs is set by the product τM^2, where τ is the dark matter to ALP decay time.[1] In [130], it was shown that reproducing the observed signal strength of [103] from the sample of stacked galaxy clusters requires:

$$\tau \sim 5 \times 10^{24}\,\mathrm{s} \left(\frac{10^{13}\,\mathrm{GeV}}{M}\right)^2 . \tag{4.1}$$

This assumes that the ALP is produced by a decay $\psi \to \chi a$. The alternative process $\psi \to aa$ simply requires a change in decay time by a factor of two. We also assume that for a typical galaxy cluster and with $E_a = 3.5\,\mathrm{keV}$, $P(a \to \gamma) = 10^{-3}\left(\frac{10^{13}\,\mathrm{GeV}}{M}\right)^2$. These numerical values are extracted from propagation of ALPs through a detailed simulation of the magnetic field for the central $1\,\mathrm{Mpc}^3$ of the Coma cluster [68],

[1] Note that τ is not necessarily the total dark matter lifetime, as there may be additional hidden sector decays.

extending the estimates of [66]. While the conversion probability for the central region of the Coma cluster can clearly only be an approximation for the stacked sample of cluster in the analysis of [103], we use it as an approximate guide to the required dark matter lifetime.

We will set τM^2 from equation (4.1) when calculating the signal strength expected from the Milky Way and M31. However, we re-emphasise that the value in equation (4.1) is based on assuming that the conversion probabilities calculated in [68] for the central region of the Coma cluster is on some level typical of clusters in general. This may in fact be either an over- or under- estimate of the actual conversion probabilities averaged over the stacked cluster sample of [103]. We note in addition that there is a potential systematic error in case the use of RMs to measure cluster magnetic fields is systematically inaccurate.

While the morphological distribution we calculate in section 4.4 below will be robust against variations in τ, the overall line strength we find will inherit this uncertainty. However as the 3.5 keV line signal has also been observed in M31 [105], this bounds this uncertainty to a factor of a few (unless there are additional large systematic errors in the magnetic field determinations in M31).

To compute the ALP to photon conversion probability, we use the density matrix approach given by equations (1.22), (1.23) and (1.24). The damping parameter is $\Gamma = \sigma_{\text{eff}}\,(n_{HI} + 2n_{H_2})$, where $n_{HI} + 2n_{H_2}$ is the density of neutral hydrogen. Photoelectric absorption is conventionally parametrised by the neutral hydrogen density, although at $E \sim 3.5\,\text{keV}$ hydrogen itself is not so important and it is heavier elements that play a dominant role. We also note that the standard values for σ_{eff} assume solar abundances for metals. However, as we will find that absorption only has a relatively small effect on the signal, we can neglect possible changes in abundances away from solar values.

In practice, we discretize the field into domains of length δz so that:

$$\rho_k = e^{-iH_k\delta z}\rho_{k-1}e^{iH_k^\dagger\delta z}, \tag{4.2}$$

where ρ_k is the density matrix in the kth domain and H_k is the Hamiltonian defined using the magnetic field, free electron density and hydrogen density in the centre of the kth domain.

4.3 The Milky Way Dark Matter Halo and Magnetic Field

To determine the strength and morphology of the photon line, we require models for the Milky Way dark matter halo, magnetic field, electron density and neutral hydrogen abundance. For the dark matter profile, we calculate the expected flux based on an NFW profile, using parameters from [132]. The NFW profile is [133]:

$$\rho_{NFW}\left(r\right) = \frac{\rho_s}{\left(\frac{r}{r_s}\right)\left(1+\frac{r}{r_s}\right)^2}, \tag{4.3}$$

where r is the spherical radius from the galactic centre, $r_s = 20\,\mathrm{kpc}$ and ρ_s is implicitly set by requiring the local dark matter density $\rho_{NFW}\left(R_\odot\right) = 0.4\,\mathrm{GeVcm}^{-3}$, with $R_\odot = 8.5\,\mathrm{kpc}$.

For the Milky Way magnetic field, we use the recent model of Jansson and Farrar, given in [62] and illustrated in Figure 4.1, based on 40,000 extragalactic Faraday RMs. The details and numerical parameters of the model are found in [62] and here we simply summarise the field. This model contains both a regular part and a random/striated component. The regular part has structure on the scale of the Milky Way and contains three elements: a disk field, a toroidal halo element and an

out-of-plane X-component. The disk field is directed in the plane of the galaxy and follows the structure of the spiral arms, although with some field reversals between different spirals. The halo field is also purely azimuthal, but extends out of the galaxy and with a greater radial extent to the South of the galaxy than to the North. The X-field component points out of the galactic plane.

We note here that this field model artificially excludes a 1 kpc sphere at the centre of the galaxy (B is set to zero in this region). This is due to the difficulties in determining the magnetic field in this region. However, on physical grounds it is in this region we expect the magnetic field strength to be largest. We therefore expect this model to underestimate the conversion probabilities for ALPs passing directly through the galactic centre.

The random/striated component contains a striated field, which is locally aligned with the regular field but of random sign, and a random field, which is unaligned with the regular component. These components are expected to be inserted into the galaxy through supernova outflows. Although the striated and random field components are actually larger than the coherent field, their coherence length is much less, of order 100 pc. This implies their contribution to $P(a \to \gamma)$ is much smaller than that of the coherent field, and so we can self-consistently neglect these in our calculations.

Let us now justify our neglect of the random and striated fields in our calculations. As above, the coherence lengths of the random and striated fields are expected to be $L \lesssim 100\,\mathrm{pc}$, and the typical value of the random magnetic field in the disk is $\langle B \rangle \sim 3\,\mu G$. Using the small angle approximation described in section 4.2 (note that the low value of L here means we have $\Delta \ll 1$ for most of the galaxy) with $L \sim 100\,\mathrm{pc}$, $R \sim 30\,\mathrm{kpc}$, $B_\perp \sim 3\,\mu\mathrm{G}$ and $M = 10^{13}\,\mathrm{GeV}$, we find the conversion probability due to the random field alone is $P_{rand} \sim 10^{-7}$. This is smaller by an order of magnitude than the conversion probabilities arising from the regular field for a 3.5 keV ALP with $M = 10^{13}\,\mathrm{GeV}$ created at $R \sim 30\,\mathrm{kpc}$ from the Earth. For the lower energy

ALPs considered in Chapter 3, Δ is larger and the random field is potentially more important.

We therefore find that even though the random component of the magnetic field is significantly larger than the regular component, its much shorter coherence length means that it can be self-consistently neglected when considering ALP-to-photon conversion.

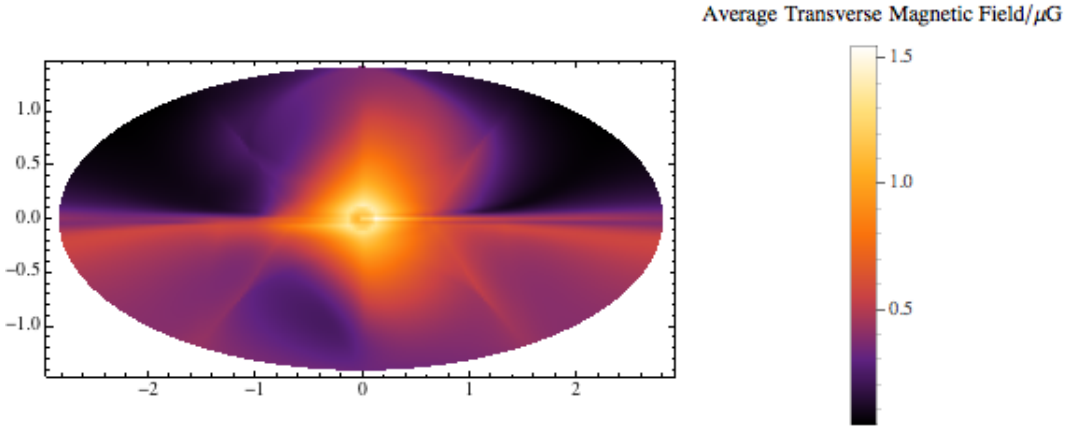

Figure 4.1: The average regular transverse magnetic field experienced by an ALP on a path starting 20 kpc from the Earth and ending at the Earth. Galactic longitude increases to the right and galactic latitude increases vertically. The centre of the plot corresponds to the direction of the galactic centre.

We use a simple model for the electron density n_e, following [134], comprising thick disk and thin disk components with vertical scale heights 1.10 kpc and 0.04 kpc respectively.[2] The behaviour of P is very sensitive to low values of n_e, as $\tan 2\theta$ diverges as $n_e \to 0$, so it is important that we do not allow unrealistically low values of n_e in our calculation. The model given in [134] is based on line of sight integrals and gives extremely low values for n_e at the edge of the Milky Way. For most astrophysical applications, these unphysically small values for n_e have no detrimental effect, but that is not true for us. We therefore set a minimum value for n_e of $10^{-7}\,\mathrm{cm}^{-3}$, the

[2]Strictly this is not entirely self-consistent, as the Jansson and Farrar model for the magnetic field is based on the use of the NE2001 [64] electron densities. However as we are almost always in the small angle approximation for both θ and Δ, the precise expression for the electron densities makes little difference to the results.

approximate value of the intergalactic free electron density. The thick disk component is:

$$n_{\rm thick} = 1.77 \times 10^{-2}\,{\rm cm}^{-3} \times \frac{{\rm sech}^2\left(\frac{\rho}{15.4\,{\rm kpc}}\right)}{{\rm sech}^2\left(\frac{R_\odot}{15.4\,{\rm kpc}}\right)} {\rm sech}^2\left(\frac{z}{1.10\,{\rm kpc}}\right), \tag{4.4}$$

where ρ is the cylindrical galactic radius, and the thin disk component is:

$$n_{\rm thin} = 1.07 \times 10^{-2}\,{\rm cm}^{-3} \times \frac{{\rm sech}^2\left(\frac{\rho}{3.6\,{\rm kpc}}\right)}{{\rm sech}^2\left(\frac{R_\odot}{3.6\,{\rm kpc}}\right)} {\rm sech}^2\left(\frac{z}{0.04\,{\rm kpc}}\right). \tag{4.5}$$

For the total electron density we take

$$n_e = \max\left[n_{\rm thick} + n_{\rm thin}, 10^{-7}\,{\rm cm}^{-3}\right]. \tag{4.6}$$

As discussed above, the observed signal is attenuated by photoelectric absorption on gas in the galaxy. We use the scattering cross sections in [97, 135]. For a 3.5 keV photon, the effective cross section per Hydrogen atom is $\sigma_{\rm eff} \sim 10^{-23}\,{\rm cm}^2$. For neutral hydrogen distributions, we use the density distributions for HI and H_2, n_{HI} and n_{H_2} respectively, given in [98]:

$$n_{HI} = \begin{cases} 0.32\,{\rm cm}^{-3}{\rm exp}\left(-\frac{\rho}{18.24\,{\rm kpc}} - \frac{|z|}{0.52\,{\rm kpc}}\right), & \text{if } \rho \geq 2.75\,{\rm kpc} \\ 0, & \text{otherwise} \end{cases} \tag{4.7}$$

$$n_{H_2} = 4.06\,{\rm cm}^{-3}{\rm exp}\left(-\frac{\rho}{2.57\,{\rm kpc}} - \frac{|\,z\,|}{0.08\,{\rm kpc}}\right). \tag{4.8}$$

4.4 Results and Discussion for the Milky Way and M31

4.4.1 Milky Way

We simulated the propagation of ALPs created at 1 kpc, 2 kpc, ... and 30 kpc from the Earth. Although the dark matter halo extends beyond this distance, the magnetic field at 30 kpc becomes negligible and we therefore assume that ALPs created over 30 kpc from the Earth propagate without conversion up to this point. As the magnetic field has non-trivial structure over these length scales, each of these paths must be simulated separately, rather than simply adding the probabilities. The environment experienced by the ALP, and therefore P, also depends strongly on where in the sky it was created. For each spherical shell, we simulated P for 20000 points in the sky, equally spaced in Earth-centred spherical polar coordinates θ and ϕ (with $\delta\theta = \frac{\pi}{100}$ and $\delta\phi = \frac{\pi}{100}$). We used 4000 domains for each path.

The expected photon flux for each direction in the sky is:

$$F = \frac{1}{\tau}\frac{1}{4\pi}\int_{r=0}^{\infty}\frac{\rho_{DM}\left(r,\theta,\phi\right)}{m_{DM}}P\left(r,\theta,\phi\right)dr\,\mathrm{sr}^{-1}, \tag{4.9}$$

where $P(r,\theta,\phi)$ is the ALP to photon conversion probability for an ALP starting at position (r,θ,ϕ) and travelling to Earth.

We evaluate the integral as a sum for the first 30 spherical shells. For ALPs produced greater than 30 kpc from the Earth, we take $P\left(r > 30\,\mathrm{kpc},\theta,\phi\right) = P\left(30\,\mathrm{kpc},\theta,\phi\right)$ and integrate ρ_{DM} from $r = 30\,\mathrm{kpc}$ to $r = \infty$ numerically.

Figure 4.2 shows the conversion probability for an ALP with $M = 10^{13}\,\mathrm{GeV}$ starting at 30 kpc from the Earth and propagating to Earth. In Figure 4.3, we show the expected flux of the 3.5 keV line from the Milky Way halo in the ALP scenario with $M = \sqrt{\frac{5\times10^{24}\,\mathrm{s}}{\tau}}\times 10^{13}\,\mathrm{GeV}$. For comparison, Figure 4.4 shows the expected

flux assuming the dark matter decays directly to photons, using the sterile neutrino model with the best fit neutrino decay mixing angle $\sin^2(2\theta) \simeq 7 \times 10^{-11}$ given in [103]. Typical fluxes are $10^{-4}\,\mathrm{cm}^{-2}\mathrm{s}^{-1}\mathrm{sr}^{-1}$ for DM $\to a \to \gamma$ and $0.1\,\mathrm{cm}^{-2}\mathrm{s}^{-1}\mathrm{sr}^{-1}$ for DM $\to \gamma$, where the lifetime is normalised to give the same signal strength for each scenario when the dark matter decay occurs in a galaxy cluster.

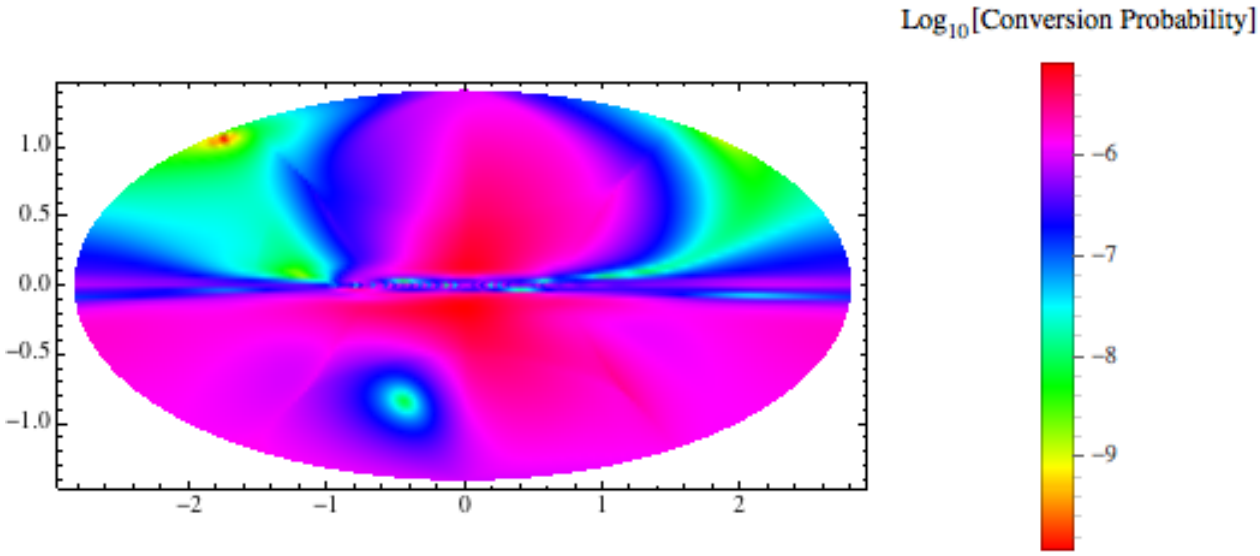

Figure 4.2: The ALP to photon conversion probability for an ALP with $M = 10^{13}\,\mathrm{GeV}$ starting at 30 kpc from the Earth and propagating to Earth. Galactic longitude increases to the right and galactic latitude increases vertically. The centre of the plot corresponds to the direction of the galactic centre.

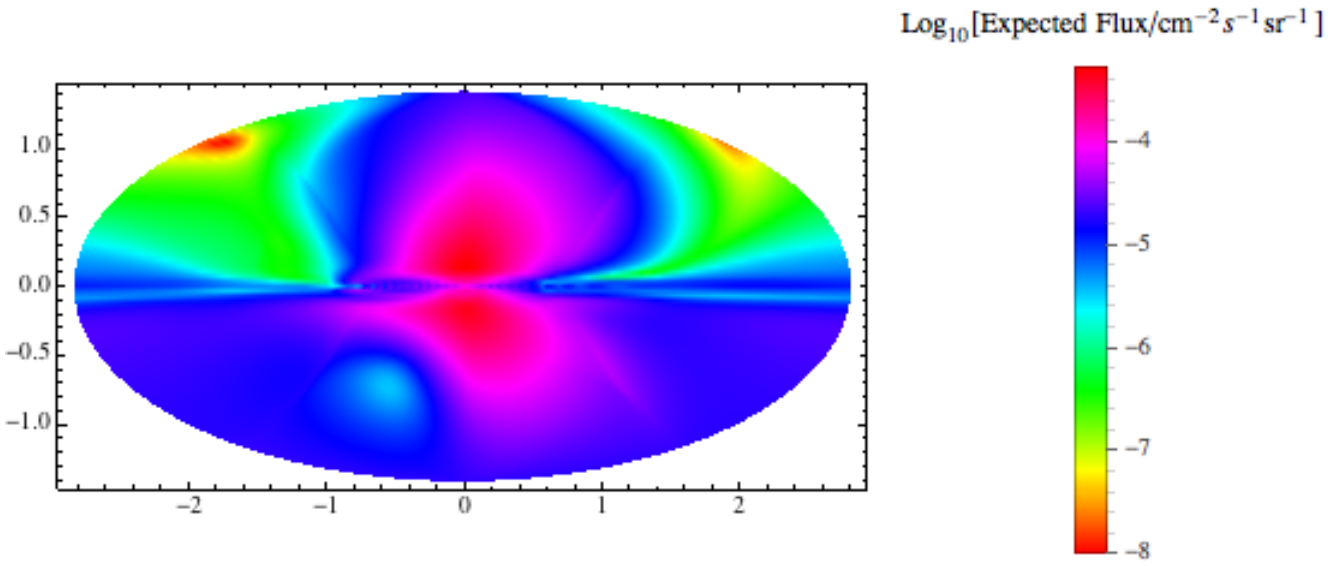

Figure 4.3: The expected 3.5 keV line flux across the sky in the ALP scenario.

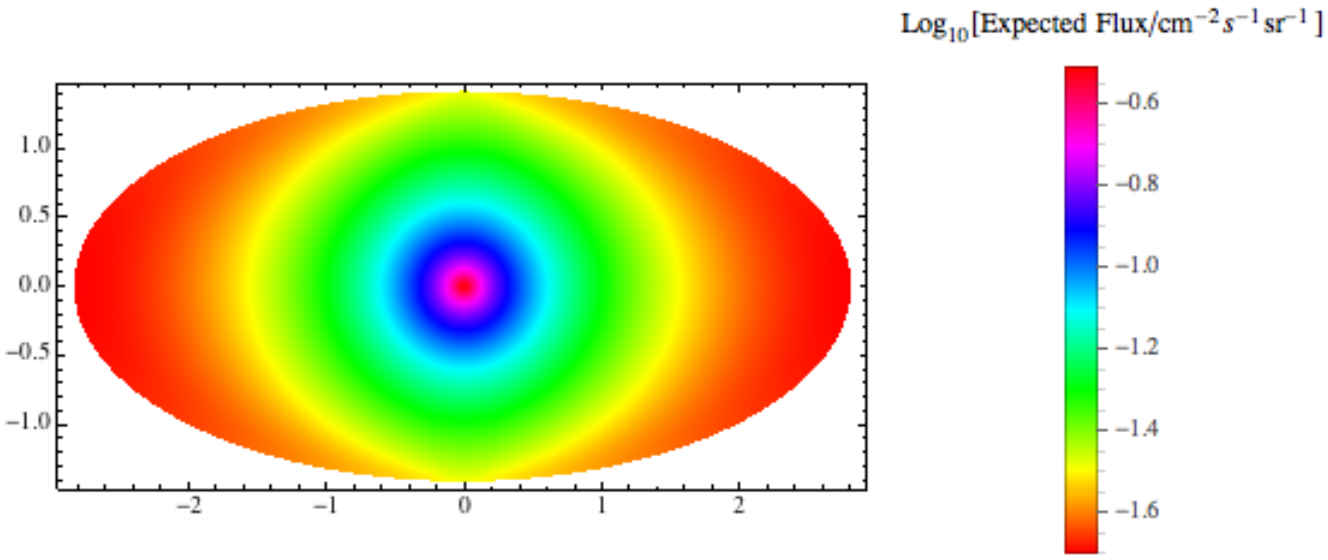

Figure 4.4: The expected 3.5 keV line flux across the sky for direct dark matter decay to photons.

The expected flux in the ALP scenario is almost 1000 times lower than for direct decay. This is because the ALP to photon conversion probability in the Milky Way is much lower than that in galaxy clusters, predominantly due to the Milky Way's

smaller size. As discussed above, this calculation relies on approximating the ALP to photon conversion probability in all the clusters with that for the central region of Coma, and on the model used for the Milky Way's magnetic field. It might therefore be that the actual flux from the Milky Way halo is larger (or even smaller). Nonetheless, we can expect that the flux from the Milky Way in the ALP scenario would be substantially lower than for direct decay to photons.

4.4.2 Andromeda (M31)

Given an observation of a 3.5 keV photon line from M31 [105], it is also important to consider the magnitude of ALP-photon conversion in M31, as M31 is in many ways a similar galaxy to the Milky Way - although twice the size with a diameter of around 70 kpc compared to 30 kpc for the Milky Way, it is also a spiral galaxy. Naively, one would therefore expect a similar suppression of the ALP-photon conversion probabilities in M31. However this appears not to be true, as radio studies [136–138] show that the regular magnetic field in M31 is both significantly larger and significantly more coherent than in the Milky Way.

Let us summarise the results of [136–138]. [137] found that between 6 and 14 kpc from the centre of M31, the M31 magnetic field is a coherent axisymmetric spiral, with a regular magnetic field strength $B_{reg} \sim 5\,\mu$G that showed minimal radial variation over this range. In contrast to the Milky Way, there is also no sign of large-scale field reversals among the spirals. They also found that the vertical scale height of this field was at least 1 kpc. [136] found that the regular magnetic field of M31 probably has a similar structure between radii of 5 and 25 kpc. The random magnetic field of M31 is a similar size to the regular field, $B_{random} \sim 5\,\mu G$. As discussed in [139], the fact that $B_{regular} \sim B_{random}$ in M31 is quite an unusual property, as generally $B_{regular} \sim \frac{B_{random}}{3}$ (as holds in the Milky Way).

The central magnetic field in M31 is also rather large. For example, based on

measurements in the central kiloparsec the authors of [138] estimate a central field $B \simeq 50\,\mu$G. Another key point is that the plane of the M31 disk is at an inclination angle of 77.5° (where 90° corresponds to an entirely edge-on spiral galaxy). This is close to edge on, and implies ALPs originating from dark matter decay in M31 pass through a large coherent transverse magnetic field on their way to Earth. These are optimal conditions for $a \to \gamma$ conversion. This would not be true if M31 had an inclination angle close to zero.

Given the above, we use the single domain small angle approximation to obtain a rough estimate of the conversion probability for a 3.5 keV ALP created at the centre of M31 and propagating to Earth. We take parameters appropriate for propagation directly along the disk. This approximation is an overestimate based on a fall-off in the magnetic field both out of the plane of the disk and with radius, and an underestimate based on neglecting the strong central magnetic field and any halo or out-of-plane components of the M31 magnetic field. Taking $B_\perp \sim 5\,\mu$G, and $L \sim 20\,$kpc, we estimate

$$P_{a\to\gamma,M31} \sim 2.3 \times 10^{-4} \left(\frac{10^{13}\,\mathrm{GeV}}{M}\right)^2, \tag{4.10}$$

which is two orders of magnitude higher than typical conversion probabilities for the Milky Way. The difference arises from the greater magnitude and coherence length of the M31 magnetic field compared to that of the Milky Way, coupled to the close to edge on nature of M31. In fact, the above conversion probability is only smaller by a factor of four than that found for a 1 Mpc path through the central region of the Coma cluster. This shows that in this scenario the observed signal strength from M31 can be comparable to that from clusters, consistent with the results of [105].

We also note that the spiral regular magnetic field in M31 implies that for observations offset from the centre we expect a rapid falloff in the signal. As we move

away from the centre, the field lines of the regular spirals will become parallel to the observational line of sight rather than transverse to the line of sight. As ALP-photon conversion only occurs for transverse magnetic fields, this will rapidly reduce the signal strength. ALP-photon conversion will still occur due to the random component of the M31 magnetic field. However, as the coherence scale L of the random field is expected to be similar to the Milky Way at $\sim$ 100pc, and the ALP-photon conversion probability scales as $P(a \to \gamma) \sim L^2$, we expect that conversion due to the random field will be negligible compared to that due to the regular field. This is consistent with the absence, albeit at low statistics, of an observed off-centre M31 line in [105].

We note that - within the DM $\to a \to \gamma$ scenario - the above points make M31 an unusually favourable galaxy for observing a 3.5 keV line. For general galaxies in this scenario the signal strength of the 3.5 keV line would be much lower than for galaxy clusters, and the fact that for M31 these can be comparable is rather uncommon.

4.5 Searching for the 3.5 keV Line in other Galaxies

In this section, we discuss the search for the 3.5 keV X-ray line in galaxies other than the Milky Way and the inferred constraints on dark matter models. We describe the predictions of the DM$\to a \to \gamma$ scenario, and compare them with the current observational situation. The first search for the 3.5 keV line in a galaxy was that of [105], who detected the line in the combined XMM-Newton spectrum of the central region of M31. As described above, this is entirely consistent with the DM$\to a \to \gamma$ scenario, based on recent estimates of M31's magnetic field. Subsequent studies have failed to detect the line in galaxy targets [111, 112, 114], while others have reported weak detections in the Draco dwarf galaxy [113] and the Milky Way halo [124]. While the line has been detected unambiguously in galaxy clusters (although its origin is

still unclear), the picture in galaxies is more murky. In the DM$\rightarrow a \rightarrow \gamma$ scenario, we generically expect no observable 3.5 keV line signal in galaxies. In particular, the detections in Draco and the Milky Way halo, if confirmed, are completely inconsistent with this model. Furthermore, dwarf spheroidal galaxies do not host any significant magnetic fields [95], and therefore would source negligible 3.5 keV line flux. However the DM$\rightarrow a \rightarrow \gamma$ scenario naturally predicts the non-detections of [111, 112, 114].

In the DM$\rightarrow a \rightarrow \gamma$ scenario, we expect spiral galaxies to be better 3.5 keV line targets, although their flux would still be significantly lower than that of galaxy clusters. Spiral galaxies tend to support ordered (regular and striated) fields. The ordered fields are strongest between spiral arms where typical values are $B_{\rm ordered} \sim$10–15 μG [95]. Note that this value includes the contribution from both the regular and the striated fields, while we are typically only concerned with the regular field. Within the spiral arms, the magnetic field is mostly tangled and randomly oriented. M31 is unusual in that it has a particularly coherent regular magnetic field $B_{\rm reg} \sim 6\,\mu$G whose strength remains constant across the spiral arms. Spiral galaxies, like the Milky Way, may also support magnetic fields in the halo surrounding the disc. Star burst galaxies can support very strong magnetic fields, however, these tend to be tangled over short scales.

In the DM$\rightarrow a \rightarrow \gamma$ scenario, we expect no line to be observable from elliptic, irregular and dwarf galaxies, which lack large-scale regular magnetic fields [130]. Spiral magnetic fields may in principle give rise to an observable signal if the regular magnetic field is sufficiently strong along the path of an ALP arising from dark matter decay. As ALP-photon conversion is suppressed by the plasma frequency, a stronger signal is expected from regions with small electron density and significant regular magnetic field. This suggests the inter-arm regions of typical spiral galaxies will typically contribute more to the photon line than the arm regions. Moreover, edge-on

Object	3.5 keV line predicted in the DM$\rightarrow a \rightarrow \gamma$ scenario?
Galaxy clusters	Yes. Galaxy clusters have large magnetic fields over Mpc distances. The cores of cool-core clusters host particularly strong fields, so a particularly strong 3.5 keV signal is expected here.
Dwarf and elliptical galaxies	No, due to very low magnetic fields.
Face-on spiral galaxies	No, as in general the halo field of a spiral galaxy is weak.
Edge-on spiral galaxies	Maybe, as the ALPs would pass through the stronger disk field. However, the signal would still likely be weaker than in galaxy clusters.
Milky Way Disk and Halo	No, as shown above.
M31	Yes, as shown above.
Milky Way centre	Maybe, depending on the (unknown) magnetic field strength.
Starburst galaxies	Maybe, depending on the electron density structure, as discussion in Chapter 3.

Table 4.2: A summary of the predictions of the DM$\rightarrow a \rightarrow \gamma$ scenario.

galaxies for which a large fraction of the ALPs travel through a significant fraction of the disc magnetic field should yield a larger signal than face-on spiral galaxies. The magnetic field direction follows the direction of the spiral arms. Therefore, for paths within a few kpc of the centre the field is generally transverse to the line of sight, whereas for paths further from the centre the field becomes parallel to the line of sight and so does not contribute to conversion. We therefore predict that the line flux is much stronger for on-centre observations, but may indeed be unobservable off-centre. The predictions of the DM$\rightarrow a \rightarrow \gamma$ scenario for different observational targets are summarised in table 4.2.

To quantify this, we simulated the expected signal for hypothetical galaxies with electron density and magnetic field such as those of the Milky Way and M31, observed at inclination angle θ_i. We will refer to these models as 'Milky Way-like' and 'M31-like'. We assumed that these galaxies were located at 1 Mpc from Earth and observed with a circular field of view with a $15'$ radius pointed at the centre of a galaxy (so that the central 4.4 kpc of the galaxy are included in the observation).

For the Milky Way-like galaxy we used the recent magnetic field model by [62] with the central 1 kpc sphere (not considered in [62]) filled in with a $5\,\mu$G poloidal field with an exponential vertical scale height of 1 kpc. We use the electron density given in the thick and thin disc components of [64] (imposing a minimum value of $n_e = 10^{-7}\,\mathrm{cm}^2$) and a NFW dark matter distribution [133] with the parameters given in [132]. We note that the Milky Way magnetic field includes a significant halo component in addition to the disk component, whereas there is no evidence for such a halo component in M31.

For the M31-like galaxy, based on [137] we assume a constant azimuthal field of $5\,\mu$G in the disk cut off at a cylindrical radius of 20 kpc. We assume an exponential fall off above and below the disk with a scale height of 2 kpc. This is clearly a vastly simplified representation of the true field in M31, underestimating the field in the centre and overestimating the field on the outskirts, but is sufficient to predict the qualitative relationship between inclination angle and flux. We use the electron density

$$n_e = 0.09\,\mathrm{cm}^{-3} \times \mathrm{e}^{-\frac{(\mathrm{r}-3.7\,\mathrm{kpc})^2}{160\,\mathrm{kpc}^2}} \times \mathrm{sech}^2\left(\frac{\mathrm{z}}{0.14\,\mathrm{kpc}}\right). \tag{4.11}$$

This is an adapted version of the thin disk component of [64], chosen by considering the electron density values given in [137]. For the Milky Way-like case, we impose a minimum electron density of $n_e = 10^{-7}\,\mathrm{cm}^2$. We assume an NFW dark matter distribution with parameters from [140].

For the M31-like galaxy in Figure 4.5, the peak flux is expected at inclination angle $\theta_i = 90°$ (edge-on). The flux for such an edge-on galaxy is over 10 times the flux for an equivalent galaxy with $\theta_i = 0°$ (face-on). Note that in this case the magnetic field model used is symmetric above and below the disc, and so the expected flux will be symmetric around $\theta_i = 90°$. For the Milky Way-like galaxy in Figure 4.6, the expected flux is lower primarily due to the smaller and less coherent field. Furthermore, rotating the galaxy from $\theta_i = 0°$ to $\theta_i = 90°$ only increases the

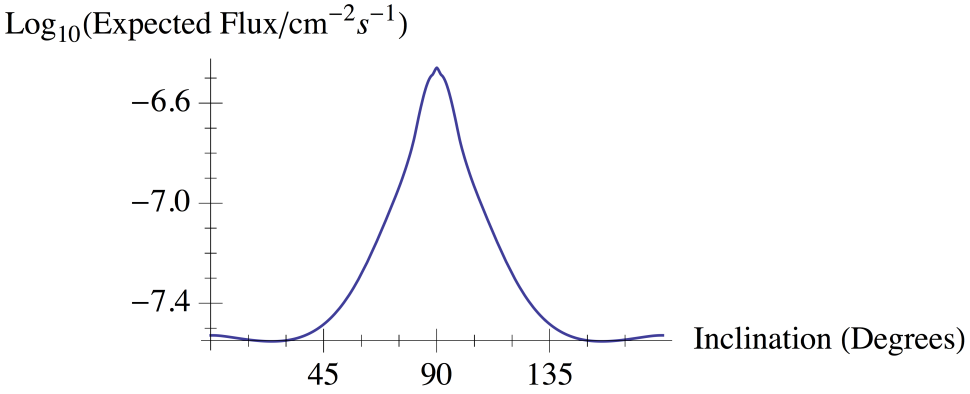

Figure 4.5: Expected flux vs inclination angle for an M31-like Galaxy

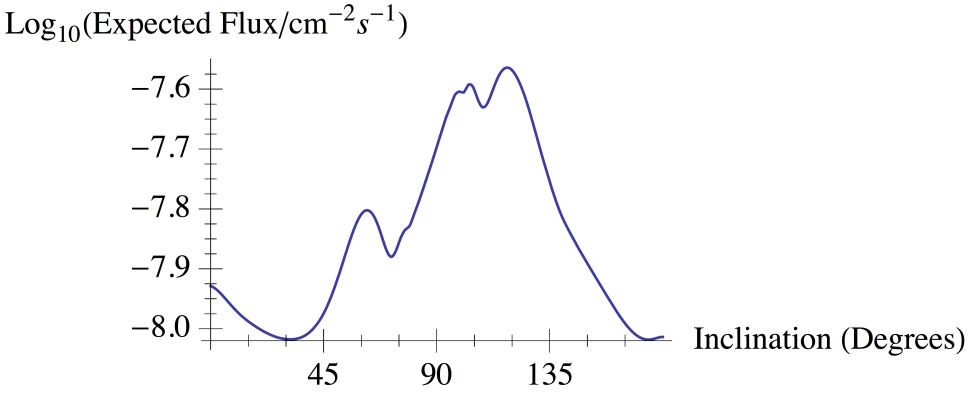

Figure 4.6: Expected flux vs inclination angle for a Milky Way-like galaxy

flux by a factor of ~ 3. This is due to the significant halo component of the Milky Way field. The halo component of the Milky Way field is not symmetric above and below the disc, and so the expected flux is not symmetric about $\theta_i = 90°$, and in fact the maximum flux occurs at an inclination angle somewhat above $\theta_i = 90°$.

In a search for the DM$\rightarrow a \rightarrow \gamma$ model, Figures 4.5 and 4.6 make it clear that we should consider a stacked sample of close to edge-on spiral galaxies. Existing X-ray data in the XMM-Newton and Chandra archives may be used to perform such a search. The strength of the signal from the DM$\rightarrow a \rightarrow \gamma$ model depends on the magnitude and the coherence of the galactic magnetic field, as well as the dark matter column density within the field of view. For distant galaxies, the whole galaxy might fit in the field of view, whereas we only expect an observable signal from the central region. In our case, the outer regions of galaxies should be masked and observations instead focused on the central regions. If it were observationally possible, galaxies with high regular magnetic fields should be preferred. However, we note that the lack of precise knowledge on the galactic magnetic fields imply that one cannot decisively rule out the model based on such a search; a definitive exclusion would require knowledge of the magnetic fields.

In sum, stacked samples of the central regions of close to edge-on spiral galaxies provide a potentially highly interesting target for searches of signals from the DM$\rightarrow$ $a \rightarrow \gamma$ model. The long total exposures of such regions in the XMM-Newton and Chandra archives suggests that such a search may be feasible with existing data, but the magnitude of the potential signal depends on astrophysical parameters that are poorly known, thus precluding a definite prediction of the signal strength. Two other potentially appealing targets are the Milky Way centre and starburst galaxies. The Milky Way centre's magnetic field is very poorly determined, with estimates varying by 2 orders of magnitude. For the highest estimates, an observable 3.5 keV line flux is possible. As discussed in Chapter 2, starburst galaxies could offer large ALP to

photon conversion probabilities, and therefore significant 3.5 kev line flux. However, both of these targets are highly complex environments, making detection of a very weak line challenging.

4.6 Conclusions

In this chapter we have studied the expected signal from the process DM $\rightarrow a \rightarrow \gamma$ in the Milky Way halo, assuming that the same process is responsible for the 3.5 keV line observed in both galaxy clusters and M31. We have also studied the same process in M31.

In doing so we have used the recent model of [63] for the magnetic field of the Milky Way. We note that this model artificially excludes the magnetic field within 1 kpc of the galactic centre, which may be significantly higher than the bulk of the Milky Way. Our results therefore apply clearly to the Milky Way halo as a whole, but only apply for sightlines passing close to the galactic centre on the (strong) assumption that the magnetic field in that region is not significantly stronger than in the Milky Way as a whole.

We can therefore make the following predictions for a 3.5 keV photon line from the Milky Way halo and other galaxies in the case that the dark matter decays to an ALP:

1. In this scenario, the flux from the Milky Way halo will be significantly lower than for the case of direct dark matter decay to photons. This arises as the ALP to photon conversion probability in the Milky Way is much lower than in galaxy clusters. This is due to both the relatively small magnetic field and relatively small coherence length in the Milky Way.

2. Although M31 is in some ways similar to the Milky Way, the conversion probabilities for DM $\rightarrow a \rightarrow \gamma$ for M31 are larger by approximately two orders of

magnitude. This is because M31 is close to edge on to us, with a large regular magnetic field coherent over a large distance. In fact the $a \to \gamma$ conversion probabilities for ALPs travelling through M31 to us are comparable to those for clusters.

3. We have also considered samples of distant galaxies, and have further quantified the qualitative statement in [130] that edge-on spiral galaxies are the most attractive galaxies for dark matter searches in this scenario.

Chapter 5

3.5 keV Emission and Absorption Lines from Fluorescent Dark Matter

This chapter is based on [6] written in collaboration with Joseph Conlon, Nicholas Jennings, Sven Krippendorf and Markus Rummel.

5.1 Introduction

In this chapter we jointly consider the anomalies at 3.5 keV in galaxy clusters - the 3.5 keV line introduced in Chapter 4, and the 3.5 keV dip found in our analysis of NGC1275 in Chapter 2. In particular, we consider the recent *Hitomi* observations of the centre of Perseus [74], which are reported to rule out the 3.5 keV line found in [103] at 99% significance. We show that that there is no incompatibility and that the overall observational picture is consistent. While the *XMM-Newton* and *Chandra* spectra involve only diffuse cluster emission, the *Hitomi* spectrum contains the sum of diffuse and AGN emission. The *Hitomi* spectrum is therefore sensitive to features in the AGN spectrum as well as in the diffuse spectrum. We show that the anomaly in

the AGN spectrum is well described by an absorption feature located at (3.54 ± 0.02) keV in the cluster frame. In this case, the combination of this dip together with the previously observed diffuse excess results overall in a mild dip at 3.54 keV, as observed in the *Hitomi* spectrum.

5.2 Observational Sensitivity

The micro-calorimeters on *Hitomi* provide unprecedented energy resolution, $\Delta E \sim 5\,\text{eV}$, and also have a rapid readout time of $\mathcal{O}(10^{-5})$s ensuring the absence of pileup. However, *Hitomi*'s angular resolution is poor compared to *Chandra* and *XMM-Newton*, with a half-power diameter of $1.2'$. *Hitomi*'s observations of the Perseus cluster [74, 141] covered an (almost) $3' \times 3'$ region at the centre of the Perseus cluster, including the central cluster AGN at the core of the galaxy NGC1275. It is reported in [74] that the AGN contributes 15% of the total counts to the 3-4 keV spectrum. The poor angular resolution of *Hitomi* makes it impossible to isolate and remove the AGN as a point source, as can be done for *Chandra* and *XMM-Newton* data. As a result, the *Hitomi* data reported in [74] is sensitive to the sum of any 3.5 keV features in the diffuse emission *plus* any 3.5 keV features in the AGN spectrum. In contrast, *XMM-Newton* and *Chandra* both use CCD technology with $\Delta E \sim 100\,\text{eV}$, but have far superior optics to *Hitomi* (half-power diameters of $17''$ and $1''$ respectively). In this case, it is possible to analyse just the diffuse emission, as the central AGN can be isolated and subtracted as a point source (through e.g. *wavdetect*), as was done in the 3.5 keV line searches with these telescopes. Such point source removal is performed as a matter of course in extended source analyses with *Chandra* and *XMM-Newton*.

5.3 Data Analysis

We will now present further analysis of the 3.5 keV dip found in Chapter 2. The spectrum of NGC1275 shows two $\sim 10\%$ residuals - a bump at 2.2 keV and a dip at 3.5 keV. As discussed in Chapter 2, the 2.2 keV feature could be caused by instrumental effects. In this chapter we focus only on the 3.5 keV dip. *Chandra* has no effective area feature at 3.5 keV, and so this feature cannot be easily attributed as instrumental. To remove any contamination from the 2.2 keV bump, we refit from 0.8 - 5 keV, but excluding the 1.8 - 2.3 keV region. The recent *Hitomi* observations have provided a highly accurate characterisation of the thermal emission in the core of the Perseus cluster. In particular, as determined in [74] the *Hitomi* spectrum for the thermal emission is well fit by a single-component *bapec* thermal plasma with a temperature of $kT = (3.48 \pm 0.07)$keV, an abundance of $Z = (0.54 \pm 0.03)$ and a velocity dispersion of $179 \pm 16 \mathrm{km\,s^{-1}}$. *bapec* is a numerical model for the spectrum of a collsionally ionised, diffuse thermal plasmal, including possible velocity broadening of the atomic lines in addition to their thermal broadening. We take advantage of this characterization to model rather than subtract the background continuum emission in this fit. (Subtracting the background yields very similar results.)

The AGN spectrum is modeled as a power law, and both the AGN and thermal emission is absorbed by neutral hydrogen in the Milky Way. Our approach is therefore to fit our extracted spectrum with the (absorbed) sum of power-law and thermal emission, *xswabs* $\times$ (*powlaw1d* + *xsbapec*). We use the *chi2datavar* statistic of the Sherpa fitting package. We freeze the parameters of the *bapec* model to be those determined by [74], allowing only the amplitude to float. Given the very high brightness of the source, there is negligible contamination from any of the local hot bubble, the diffuse cosmic X-ray background or instrumental background. This overall fit is good, with a χ^2 of 273 for 250 degrees of freedom. We show this fit in Figure 5.1.

This fit clearly shows a deficit around 3.5 keV. To characterise the location and

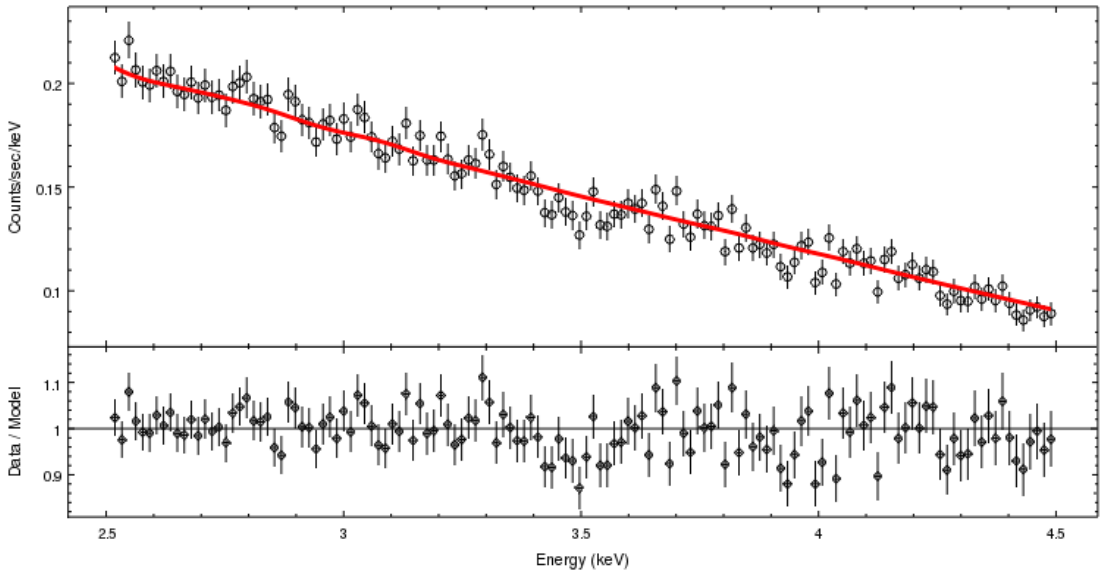

Figure 5.1: The spectrum around 3.5 keV prior to the inclusion of a negative Gaussian. The fit is from 0.8 to 5 keV using a *xswabs* × (*powlaw1d* + *xsbapec*) model, excluding the region from 1.8 to 2.3 keV containing a sharp effective area dip.

significance of this deficit precisely, we then include a negative Gaussian *xswabs* × (*powlaw1d* + *xsbapec* - *xszgauss*). We allow the energy of the Gaussian to float between a range of 3.3 and 3.7 keV in the frame of the Perseus cluster (the observed energy is redshifted by $z = 0.0176$). For definiteness we assign the line an intrinsic broadening of 10 eV, but in practice any width significantly smaller than the instrumental broadening of ~ 100 eV is equivalent in the fit.

The resulting fit is plotted in Figure 5.2 and we see that the additional negative Gaussian is an excellent model for the deficit. The best fit energy is $E = (3.54 \pm 0.02)$ keV, with an improvement of $\Delta\chi^2 = 20.0$ for an additional 2 degrees of freedom. The best fit strength for the deficit is (-7.8 ± 1.7) photons cm^{-2} s^{-2}.

For this fit, we show in Figure 5.3 a contour plot of the energy and strength of the negative Gaussian. As a check on the significance implied by the $\Delta\chi^2$ value, we generated 20,000 fake spectra[1] using Sherpa's *fakepha* command and the response files for the off-centre observations. We fit the fake data sets over the same energy

[1]At 4-sigma one in 16,000 spectra is an outlier, i.e. a 4-sigma dip would occur statistically at this rate.

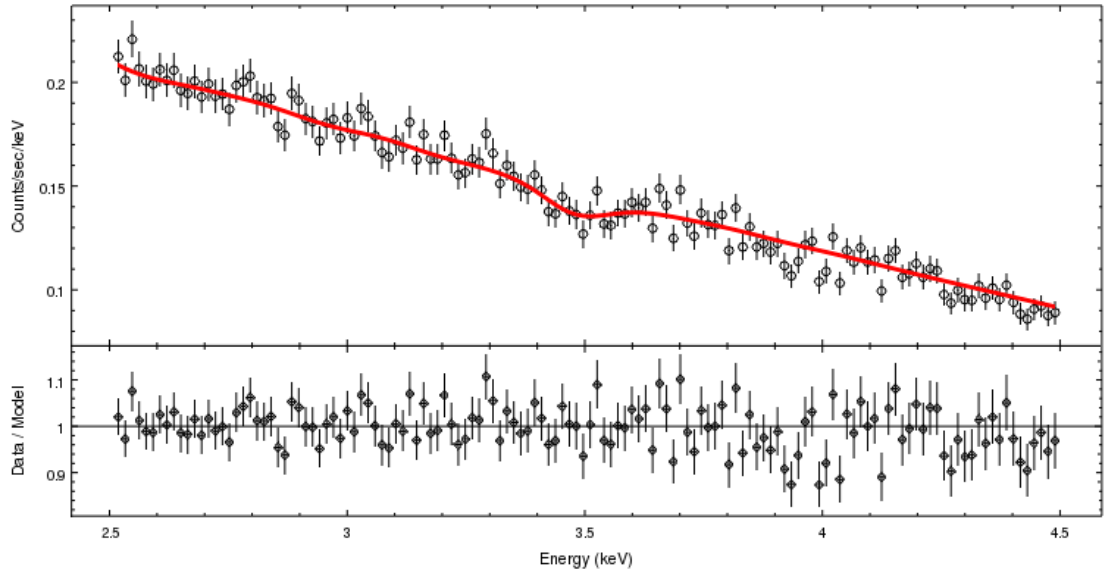

Figure 5.2: The spectrum around 3.5 keV, now fitting the same region with *xswabs* × (*powlaw1d* + *xsbapec* - *xszgauss*). The redshift of the Gaussian is fixed to $z = 0.0176$ and its intrinsic line width fixed to 10 eV, with the norm and energy allowed to float.

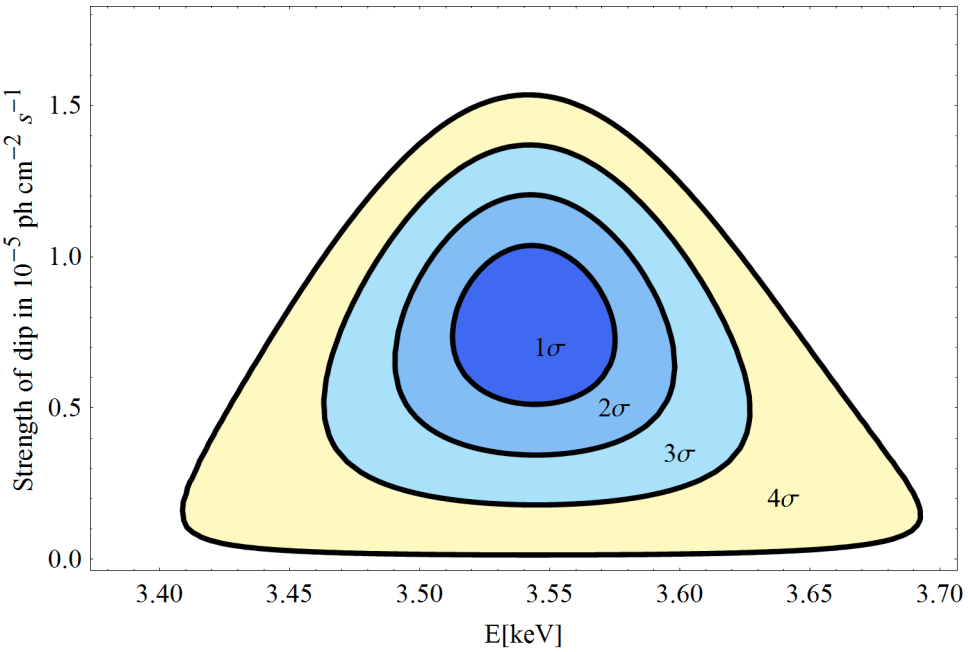

Figure 5.3: The location and strength of the best-fit dip in the AGN spectrum, derived from stacked *Chandra* observations 11713, 12025, 12033 and 12036.

range and in the same manner as for the real data, first with *xswabs* × (*powlaw1d* + *xsbapec*) and then with *xswabs* × (*powlaw1d* + *xsbapec* - *xszgauss*), allowing the energy of the Gaussian to float between 3.3 and 3.7 keV. However, for none of these fake data sets was an additional negative Gaussian able to produce an improvement in the χ^2 greater than that seen in the real data.

The above analysis focused on the four *Chandra* observations in which the AGN is highly off-axis, and therefore not significantly affected by pile-up [74]. As a side comment, we note that there were also four further observations taken in 2009 (*Chandra* obsids 11714, 11715, 11716, 12037) where the AGN is a few arcminutes off-axis. Pileup remains a serious contaminant for these observations. Nonetheless, we can exclude the central piled-up parts of the AGN image to extract a 'clean' spectrum. To clean the spectrum, we analyse the images and count rates of each observation using the image software `ds9`. The precise method of central exclusion is somewhat arbitrary; the method used to produce the spectra was as follows. We set the `ds9` binning such that the `ds9` pixels are essentially the same size as the physical *Chandra* pixels (half an arc-second across). We then create an extraction region manually excluding all `ds9` pixels which are neighbours (either side-by-side or diagonally) to any pixel with total counts greater than 1% of the overall exposure time. Using the `pileup_map` tool, this results in almost all retained pixels having a pile-up fraction lower than 5%.

We fit this in an identical fashion, working from 0.8 to 5 keV excluding 1.8 to 2.3 keV with a *xswabs* × (*powlaw1d* + *xsbapec* - *xszgauss*) model. Doing so, there is a mild preference ($\Delta\chi^2 = 1.5$) for a dip in the AGN spectrum at a best-fit energy of (3.55 ± 0.10) keV. If the overall fitted amplitude of the AGN spectrum in these observations is rescaled to be the same as that for the highly off-centre observations, the amplitude of this dip would then correspond to $(-5.1 \pm 4.2) \times 10^{-6}\,\mathrm{ph\,cm^{-2}\,s^{-1}}$. While insignificant by itself, this is consistent with the earlier result using the highly

off-axis observations.

It is striking that the dip in the AGN spectrum occurs at an identical energy to the excess from the diffuse cluster emission discussed in Chapter 4. We discuss possible physical models for this below. First though, we note that if such a dip is present in the AGN spectrum – and it is over 4σ significant in the only clean observations of the AGN – then it contributes to the *Hitomi* data, which sums the AGN and cluster emission.

To determine the magnitude of its effect there, we also require the overall AGN normalisation, as on physical grounds such a dip only makes sense as a fractional reduction in the AGN spectrum. The AGN luminosity is highly variable; its lightcurve since 1970 is described in [142]. Although still much dimmer than its 1980s peak, it has been brightening since 2001. The clean 2009 *Chandra* observations give a best-fit normalisation of $4.7 \times 10^{-3}\,\mathrm{ph\,cm^{-2}\,s^{-1}\,keV^{-1}}$ at 1 keV, while it is reported in [74] that the 2016 *Hitomi* data give a normalisation of $9.0 \times 10^{-3}\,\mathrm{ph\,cm^{-2}\,s^{-1}\,keV^{-1}}$ at 1 keV, an approximate doubling of the strength since 2009.

Based on this, we now rescale the 2009 result into an expected 2016 dip of $(-14.9 \pm 3.3) \times 10^{-6}\,\mathrm{ph\,cm^{-2}\,s^{-1}}$ in the AGN spectrum at $E = (3.54 \pm 0.02)$ keV. In [74] it is reported that the expected diffuse excess emission in the 2016 *Hitomi* data, based on *XMM-Newton* observations restricted to the SXS field of view, was $(9.0 \pm 2.9) \times 10^{-6}\,\mathrm{ph\,cm^{-2}\,s^{-1}}$ at $E = 3.54^{+0.03}_{-0.04}$ keV. Summing these two results then leads us to expect a *dip* in the 2016 *Hitomi* data at 3.54 keV of $(-5.9 \pm 4.4) \times 10^{-6}\,\mathrm{ph\,cm^{-2}\,s^{-1}}$.

And indeed this is precisely what is observed: from Figure 3 in [74], we see that for broadening by the dark matter velocity dispersion of $1300\,\mathrm{km\,s^{-1}}$ the *Hitomi* data shows a best-fit dip of $(-8 \times 10^{-6})\,\mathrm{ph\,cm^{-2}\,s^{-1}}$ at $E = (3.55 \pm 0.02)$ keV (the error is estimated from Figure 3 in [74]), at a significance of ~ 2.3. *Hitomi* observations of other sources (Crab and G21.5-0.9) show no such deficit, and rule out an unmodeled effective area feature at 3.5 keV. To further test the dip's origin, [74] divide their

data into two subsets, 'early' observations and 'late' observations. These subsets are separated in observation time by a week. The dip appears only in the 'early' subset, although the two subsets are only $\sim 2\sigma$ apart at 3.5 keV, as shown in Figure 5.4 reproduced from [74]. This is not necessarily inconsistent with the a dip in the AGN spectrum, as the AGN's luminosity may vary on a time-scale of days, and therefore contribute less of the flux in the 'late' observations. Furthermore, our predicted dip strength in the *Hitomi* spectrum is consistent with zero within 1.5σ.

The data sets are therefore consistent; *XMM-Newton* data shows an excess in the diffuse cluster emission at $3.54^{+0.03}_{-0.04}$keV, *Chandra* data on the AGN shows a strong dip in the spectrum at the same energy, and *Hitomi* data (sensitive to both cluster and AGN) gives a dip at (3.55 ± 0.02)keV of the expected magnitude once these two effects are combined.

5.4 Fluorescent Dark Matter

In the previous section, we saw that the various datasets on 3.5 keV photons from Perseus are remarkably consistent and contain a variety of high-significance features at $E \simeq 3.54$ keV. The discovery of the 3.5 keV dip leads us to consider a different model for the 3.5 keV line to that presented in Chapter 3. We focus on ways to obtain deficits in the AGN spectrum; there are many ways, both astrophysical and exotic, to generate excesses, but fewer that can give rise to spectral deficits. Instrumental explanations are also less plausible here; the 3.5 keV dip is not on an effective area feature, and is proportionally quite large. Indeed, the AGN deficit has an equivalent width of ~ 15eV compared to ~ 1eV for the diffuse excess. (The equivalent width of a feature is the width of the background spectrum required to achieve the same number of photons as compose the feature.) We might seek to explain the 3.5 keV dip as an atomic absorption line, requiring no new physics. However, the large equivalent width of the

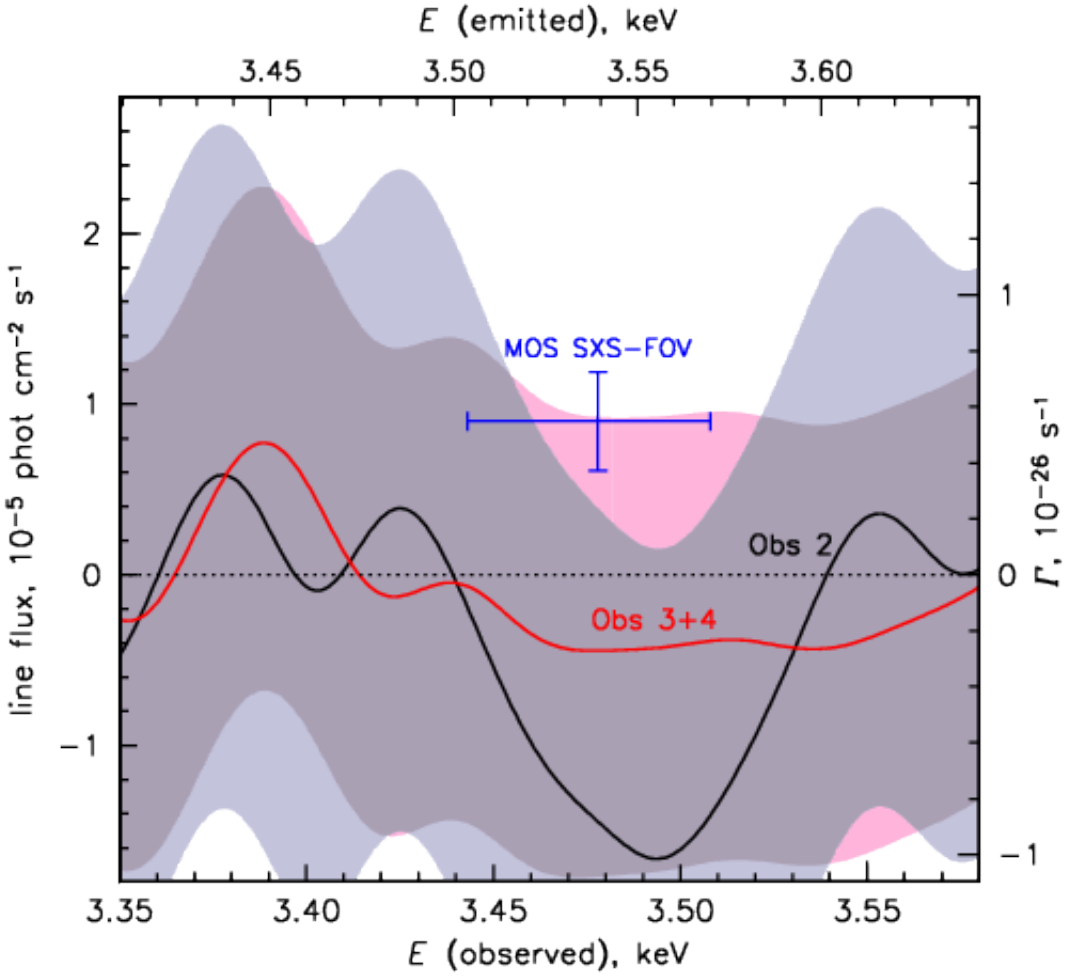

Figure 5.4: The best fit dip or line flux in the early and late Hitomi data sets vs the dip or line energy, for a line broadened by the dark matter velocity 1300 ms^{-1}. Observation 2 was taken a week earlier than observations 3 and 4. The shaded bands show $\pm 3\sigma$ limits on the best fit flux.The blue cross shows the expected 3.5 keV line flux and energy with 1σ errors based on its observation in *XMM-Newton*'s MOS detector [103], and assuming no additional 3.5 keV feature in NGC1275. Reproduced from [74].

dip makes this unlikely. The average baryonic velocity broadening along the line of sight through Perseus to NGC1275 is 2.4 eV, making it very difficult to achieve a 15 eV equivalent width feature from baryonic physics. One way round this problem would be to explain the dip with baryonic physics taking place in the AGN itself, where velocities are much higher. However, there is no apparent mechanism to generate such a strong absorption line with no other line-like features. The average dark matter velocity broadening towards NGC1275, however, is $\sim$ 15 eV. It is therefore possible to interpret the dip as a dark sector absorption line.

We therefore look for models where the same underlying mechanism is responsible for both the deficit in the AGN spectrum and the excess in the diffuse spectrum at 3.54 keV (3.48 keV in the observer frame). A simple scenario involves a 2-state dark matter model (χ_1 and χ_2). The lower state χ_1 makes up the majority of the dark matter, and absorbs a 3.54 keV photon to enter the excited state χ_2, which then decays by re-emission of the photon. A sample Lagrangian is

$$\mathcal{L} \supset \frac{1}{M}\bar{\chi}_2\sigma_{\mu\nu}\chi_1 F^{\mu\nu}, \tag{5.1}$$

and this type of resonant absorption is analysed in greater detail in [143]. The AGN dip at $E = 3.54$ keV would then be a dark sector analogue of e.g. Lyman-α absorption, with the diffuse excess at the same energy the result of fluorescent re-emission.

To explain both the 3.5 keV deficit and excess in this way, the states χ_1 and χ_2 must be massive enough that they can be treated as non-relativistic – otherwise, the line arising from the decay $\chi_2 \to \chi_1\gamma$ would be Doppler shifted, and so appear at a different energy than for the absorption process $\chi_1 + \gamma \to \chi_2$. As the energy of the dip (3.54 ± 0.02)keV is consistent at the per cent level with the 3.5 keV emission line, this requires $m_{\chi_1} > 1$MeV. For the rest of this chapter we shall assume that this holds, so that the particles χ_1 and χ_2 can be treated for the purposes of emission and

absorption as extremely heavy and non-relativistic.

If we treat the absorption of 3.54 keV photons as a Breit-Wigner resonance and assume a 100% branching ratio for $\chi_2 \to \chi_1\gamma$, we can determine the width Γ of the process $\chi_2 \to \chi_1\gamma$ using the observed photon deficit from the AGN. The cross section for $\chi_1\gamma \to \chi_1\gamma$ has a resonance at photon energy $E_0 = \frac{m_2^2 - m_1^2}{2m_1} \stackrel{!}{=} 3.54\,\mathrm{keV}$ in the rest frame of the dark matter, where m_1 and m_2 are the masses of χ_1 and χ_2 respectively. Near the resonance, the cross section is described by the relativistic Breit-Wigner formula:

$$\sigma_{\mathrm{BW}}(E) = \frac{2\pi}{p_{CM}^2} \frac{(m_2\Gamma_{\chi_2})^2}{(s - m_2^2)^2 + (m_2\Gamma_{\chi_2})^2} \ , \tag{5.2}$$

where $p_{CM}^2 = \frac{m_1^2 E^2}{m_1^2 + 2m_1 E}$ is the squared magnitude of the momentum in the centre of mass frame; Γ_{χ_2} is the total decay rate of χ_2 and $\sqrt{s}$ is the centre of mass energy.

For the dark matter column density along the line of sight to NGC1275, we use an NFW profile appropriate to the Perseus cluster

$$\rho_{DM}(r) = \frac{\rho_0}{\frac{r}{r_s}\left(1 + \left(\frac{r}{r_s}\right)^2\right)} \ , \tag{5.3}$$

with $r_s = 0.477$ Mpc and $\rho_0 = 7.35 \times 10^{14} M_\odot\,\mathrm{Mpc}^3$ [144]. As the AGN is the dynamical centre of the cluster, the integrated column density is formally divergent, and we cut off the integral at 0.01 and 2 Mpc.

However, there is a significant uncertainty attached to the exact column density towards NGC1275. There are two main factors.

First, the actual Perseus cluster profile may be cored instead of the cusp present in NFW. For low-mass galaxies, the profile is known to have a core rather than a cusp. This may arise merely from baryonic feedback on a cuspy cold dark matter profile, but alternatively may require a more substantial modification such as warm dark matter. If the Perseus cluster profile is indeed cored, it will reduce the column

density from the value inferred above.

Secondly, the profile is only that for the cluster. The line of sight originates at the very centre of NGC1275, the supergiant central elliptical galaxy of the cluster. The NGC1275 dark matter profile is not known but is expected to give a significant contribution to the dark matter column density (for example, given the size of NGC1275 it should be much larger than that towards Sgr A*).

The dark matter-photon interaction cross section is broadened from equation (5.2) by the dark matter velocity, to a resonance with a width of ~ 15 eV. We require that the integrated cross section in this range is sufficient to produce the observed photon deficit in the 3.5 keV dip. Given that the dip strength has equivalent width of 15 eV, we can then derive (assuming $m_{DM} \gg 3.5\text{keV}$)

$$\Gamma \gtrsim \left(\frac{m_{DM}}{\text{GeV}}\right) \times (1-10) \times 10^{-10}\,\text{keV}\ . \tag{5.4}$$

We give a broad range to allow for the significant uncertainty in the actual dark matter column density along the line of sight to NGC1275. The inequality arises because the equivalent width of the dip strength is very similar to that expected to be induced by dark matter broadening. Once absorption within this region is saturated, an increase in Γ will not significantly increase the overall strength of the dip.

In our Fluorescent Dark Matter Model (5.1), the decay width of the excited state is given by:

$$\Gamma = \frac{4}{\pi M^2}\frac{(m_2^2 - m_1^2)^3}{m_2^3} \simeq \frac{4}{\pi M^2}(m_2 - m_1)^3, \tag{5.5}$$

where we have assumed $\frac{m_2 - m_1}{m_1} \ll 1$. Based on equation (5.4), we then require $M \lesssim 10$ GeV to explain all of the observed 3.5 keV dip. However, the contribution of (5.1) to the running of α_{em}, and therefore to the electron's anomalous magnetic moment,

constrains $M \gtrsim 100$ GeV [145]. We would require either new physics to cancel this contribution, or a higher dark matter column density to evade this bound. The running of $\alpha_{\rm em}$ gives the leading bound on M for $m_1 \lesssim 1$ GeV. For $m_1 \gtrsim 1$ GeV, Fluorescent Dark Matter would be observable in direct detection experiments, and so this parameter range is excluded [145].

5.5 Morphological Features

We now consider the morphological distribution of the 3.5 keV emission. We consider the simplest case, where all 3.5 keV emission in $\chi_2 \to \chi_1\gamma$ arises after initial absorption of a real 3.5 keV photon. More generally, one could also consider cases where the absorbed photon is virtual and arises from scattering off protons, electrons [145] or other particles. Real photon absorption is dominant for the magnetic dipole interaction shown in equation (5.1) [145].

For this simplest case, the most basic feature of fluorescent dark matter is that the total number of 3.5 keV photons is conserved: the total excess emission, integrated across a cluster, must be precisely balanced by the integrated deficit. This result is independent of the detailed dark matter profile. As all absorbed photons are subsequently re-emitted, it follows that there is no net production of 3.5 keV photons in this model. Fluorescent dark matter merely resonantly *scatters* 3.5 keV photons.

Applying this to the Perseus cluster, this would require the time-averaged *deficit* in 3.5 keV photons from the central AGN, measured in units of $\mathrm{ph\,cm^{-2}\,s^{-1}}$, to precisely equal the *excess* in 3.5 keV photons from diffuse emission across the entire cluster. The 2009 *Chandra* dip is $-7.8 \times 10^{-6}\,\mathrm{ph\,cm^{-2}\,s^{-1}}$, while the total excess reported in [103] across the *XMM-Newton* field of view is $52^{+24}_{-15} \times 10^{-6}\,\mathrm{ph\,cm^{-2}\,s^{-1}}$ (given the large field of view of *XMM-Newton*, we take this value as a proxy for the total emission of the cluster).

For a time-varying AGN luminosity, the photon density at radius r depends on the luminosity at time $(t_{now} - \frac{r}{c})$. The observations of the 3.5 keV excess are based on fields of view extending over $\mathcal{O}(10-100\text{kpc})$ regions. In this scenario, the magnitude of the excess then requires effectively averaging the AGN luminosity over periods of $10^4 - 10^6$ years. Given our (limited) knowledge of the time-variability of the AGN, these values are consistent. For example, from 1970 - 1988 the AGN luminosity was 5-8 times greater than its 2009 value [142]. Its variability on larger timescales is unknown. In fluorescent dark matter, the magnitude of the diffuse emission is set by the product of the dark matter density and the 3.5 keV photon density. We first consider only the photons originating from the AGN and approximate the AGN emission as spherically symmetric and with constant luminosity. In this case $\rho_\gamma(r, \theta, \phi, t) \propto r^{-2}$. We assume that Γ is close to its lower limit, such that the 3.5 keV photons undergo only $\mathcal{O}(1)$ dark matter interactions as they exit the cluster, and therefore their distribution is not significantly affected by their interaction with the dark matter. For an NFW profile, the 3.5 keV emissivity is then

$$\mathcal{L}_{3.5\text{keV}} \propto \rho_{DM}(r)\rho_\gamma(r) \propto \frac{\rho_0}{r^3\left(1+\left(\frac{r}{r_s}\right)\right)^2} \ .$$

This has a much sharper central peaking than either decaying ($\propto \rho_{DM}(r)$) or annihilating dark matter ($\propto \rho_{DM}(r)^2$). This is interesting as a sharp central peaking is preferred by the results of [103, 110, 117] (indeed [103] found that approximately half the 3.5 keV diffuse emission was contained within $1'$ of the cluster centre).

Using an NFW dark matter profile for simplicity, we plot in Figure 5.5 the resulting radial emission profile. For comparison, we also plot the radial profile of a 3.5 keV line from direct dark matter decay to photons normalised to give the same total flux integrated over the cluster. In the direct decay case, the flux is proportional to the dark matter column density.

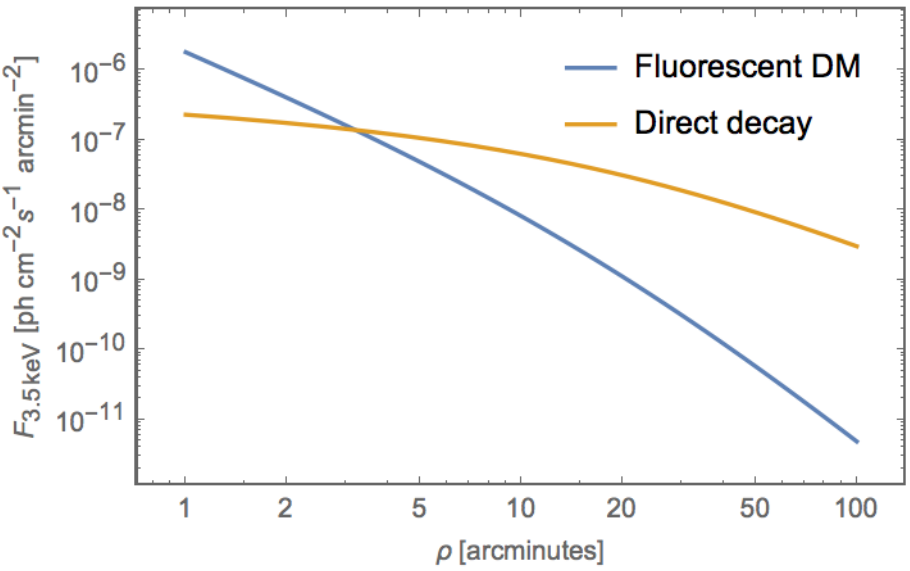

Figure 5.5: The radial profile of the 3.5 keV line flux for the Fluorescent Dark Matter model presented here and for dark matter decay. The flux is normalised to match the overall flux in [103].

This result will be modified as a consequence of absorption and re-emission of the diffuse thermal 3.5 keV photons present from the thermal bremsstrahlung spectrum. As the overall number of photons is conserved, this will not affect the overall magnitude of the diffuse excess but will modify the radial profile. Another modification of the radial profile could arise if the dark matter profile is cored rather than cuspy as for NFW; in this case the central peaking of the excess would be $\propto r^{-2}$ rather than $\propto r^{-3}$.

A further modification would be due to the angular anisotropy of the AGN flux. The jets have preferred orientations, and in this scenario we would expect the excess to be preferentially generated near to the axes of the jets. Given high-statistics evidence for the diffuse 3.5 keV excess, one could search for an angular anisotropy in the flux correlated with the direction of the jet. However, as currently there is only approximately 4σ evidence for the line from the entirety of the Perseus cluster, there are insufficient statistics to do a detailed morphological analysis.

In the fluorescent dark matter scenario, there is no net production of 3.5 keV

photons. Note that this does not lead to a contradiction with the observation of a net excess from the stacked cluster sample of [103]. A general feature of this model is that it leads to deficits in 3.5 keV photons from point sources and excesses from the diffuse emission; in the stacked analysis, however, all point sources are removed from the analysis *ab initio* (using *wavdetect*) and the spectrum only contains the diffuse emission. A possible signal of this model could be found by observing a deficit at 3.54 keV in stacked analyses of point sources, weighted by the line-of-sight dark matter column density.

5.6 Conclusions

We have argued that *Hitomi*, *XMM-Newton* and *Chandra* observations of the Perseus cluster at $E \sim 3.5\,\mathrm{keV}$ show a remarkable degree of consistency. In particular, the Hitomi spectrum around 3.5 keV can be understood as the sum of a dip in the AGN spectrum at $E = (3.54 \pm 0.02)$ keV (observed by *Chandra*) with an excess in the diffuse cluster emission at an identical energy (observed by *XMM-Newton* and *Chandra*). We have described dark matter models that can give rise to this phenomenology.

Sadly *Hitomi* is no longer able to contribute to observational efforts to understand the 3.5 keV line. We have emphasised that an accurate and clean spectrum of the NGC1275 AGN is crucial for understanding this phenomenon. Significant improvements on this can be made using operating satellites and with existing CCD technology. The best current spectrum was taken in 2009 by *Chandra* with the nominal frame time of 3 seconds. Given the AGN is now twice as bright, a further dedicated off-axis observation of NGC1275, operating with reduced frame time to minimise pileup, would give a substantial improvement over the 2009 data.

Chapter 6

Conclusions

This thesis analyses X-ray observations through the lenses of ALP phenomenology and of dark matter signals. ALPs are ultra-light scalar particles motivated by string compactifications and by the strong CP problem. In a background magnetic field, ALPs and photons interconvert, leading to a wide array of astrophysical effects. X-rays are the ideal wavelength to search for ALP-photon conversion, as the photon's effective mass in the plasma of a galaxy or galaxy cluster leads to distinctive pseudo-sinusoidal oscillations at X-ray energies. This method has the advantage of searching simply for the existence of the ALP, even if it does not make up a significant dark matter or dark radiation. We use this effect to place leading bounds on the strength of the ALP-photon interaction for ultra-light ALPs.

We also consider line-like anomalies in X-ray observations at 3.5 keV that, if confirmed, could point to physics beyond the Standard Model. The cause of these anomalies is still unknown, and an astrophysical or instrumental explanation may yet be found. The 3.5 keV features are nonetheless a compelling hint of potential BSM physics, particularly as line features are harder to generate from known physics than are broad excesses.

In Chapter 2 we search for ALP induced modulations in the spectra of four point sources in or behind galaxy clusters. The large scale magnetic fields of galaxy clusters make them ideal photon to ALP converters. In three of the sources, no such modulations are observed. However, in NGC1275 we find an upward modulation at 2.2 keV at $> 5\sigma$ and a downward modulation at 3.5 keV at $> 4\sigma$. The upward modulation is at the energy of an effective area edge, and so we attribute it to instrumental effects. The downward modulation is at the same energy as the 3.5 keV line discussed below. Its cause is unknown, but even amongst explanations from new fundamental physics ALPs are not the most likely given this coincidence in energy. We therefore conclude that there are no modulations from ALP-photon interconversion in the sources studied. We use this null result to bound the ALP-photon coupling, achieving bounds that exceed those of even next generation ALP search experiments.

In Chapter 3 we consider a string-motivated primordially generated cosmic ALP background (CAB). The CAB could explain the long-standing excess of soft X-rays observed in galaxy clusters, as CAB ALPs convert into photons in the cluster's magnetic field. We study possible signatures in galaxies via conversion to photons in their magnetic fields. We find that this effect would be unobservable in the Milky Way but could be observable in starburst galaxies.

In Chapter 4, we study the anomalous line at 3.5 keV observed in galaxy clusters and the Andromeda galaxy. Many authors have speculated that this line arises from dark matter decay to photons. We show that a scenario in which dark matter decays to ALPs which subsequently convert to photons in astrophysical magnetic fields is preferred by the observed morphology of the line. We predict that in this model the 3.5 keV line would not be observed in the Milky Way halo or in a generic sample of stacked galaxies, due to the ALP to photon conversion probability in these objects being much lower than in galaxy clusters. However, we predict the line could be observed in a stacked sample of edge-on spiral galaxies.

In Chapter 5 we combine the two anomalies at 3.5 keV - the line observed in clusters and the dip we find in NGC1275. This motivates an alternative interpretation in which the 3.5 keV line and 3.5 keV dip are both signals from a two state fluorescent dark matter model. We show that this model is consistent with recent X-ray observations from the *Hitomi* telescope. In fluorescent dark matter, we predict an absorption feature at 3.5 keV in the spectra of point sources shining through large dark matter column densities. Conversely, we predict a 3.5 kev line in the diffuse emission surrounding the point source.

Further observation and analysis is required to confirm or refute a fundamental physics origin of the anomalies at 3.5 keV. Future telescopes such as Athena will offer far superior energy resolution, allowing us to fully resolve both the 3.5 keV line and ALP-photon conversion oscillations. This will allow us to determine the origin on the 3.5 keV line, and to place far superior bounds on the ALP-photon interaction. Such astrophysical searches provide an excellent complement to the substantial ground-based efforts to detect dark sector interactions with the Standard Model. The current and future X-ray archive provides extensive information on the most extreme structures in the universe, and so is a natural place to search for new physics. X-ray observations over the next few decades will undoubtedly have profound implications for fundamental physics.

More broadly, uncovering the nature of dark matter could provide the key to determining the UV physics behind the Standard Model. A priori, signals from dark matter could manifest at any wavelength, and next generation telescopes across the spectrum offer strong discovery potential for new physics. Furthermore, we have now begun to observe the universe in neutrinos and in gravitational waves. By combining these channels, we can hope to uncover any deviation of astrophysical systems from the SM expectations. In particular gravitational waves will allow us to probe regimes

of gravity that have thus far not been tested. Unification of gravity and the SM is a crucial problem in fundamental physics, and therefore these tests are an extremely promising direction to search for new physics. The complexity of astrophysical systems makes them highly challenging targets for discovering new effects. However, we expect astrophysical simulations and models to improve over the coming years, increasing their reach for ruling out additional physics. Furthermore, by combining observations of different systems, and perhaps at different wavelengths, compelling evidence for new physics could emerge.

Bibliography

[1] M. Berg, J. P. Conlon, F. Day, N. Jennings, S. Krippendorf, A. J. Powell, and M. Rummel, *Searches for Axion-Like Particles with NGC1275: Observation of Spectral Modulations*, arXiv:1605.0104.

[2] J. P. Conlon, F. Day, N. Jennings, S. Krippendorf, and M. Rummel, *Constraints on Axion-Like Particles from Non-Observation of Spectral Modulations for X-ray Point Sources*, arXiv:1704.0525.

[3] F. V. Day, *Cosmic axion background propagation in galaxies*, *Phys. Lett.* **B753** (2016) 600–611, [arXiv:1506.0533].

[4] J. P. Conlon and F. V. Day, *3.55 keV photon lines from axion to photon conversion in the Milky Way and M31*, *JCAP* **1411** (2014) 033, [arXiv:1404.7741].

[5] P. D. Alvarez, J. P. Conlon, F. V. Day, M. C. D. Marsh, and M. Rummel, *Observational consistency and future predictions for a 3.5 keV ALP to photon line*, *JCAP* **1504** (2015), no. 04 013, [arXiv:1410.1867].

[6] J. P. Conlon, F. Day, N. Jennings, S. Krippendorf, and M. Rummel, *Consistency of Hitomi, XMM-Newton and Chandra 3.5 keV data from Perseus*, arXiv:1608.0168.

[7] J. R. Ellis, M. K. Gaillard, and G. G. Ross, *Search for Gluons in e+ e- Annihilation*, *Nucl. Phys.* **B111** (1976) 253. [Erratum: Nucl. Phys.B130,516(1977)].

[8] R. Brandelik *et al*, *Evidence for planar events in e+e annihilation at high energies*, *Physics Letters B* **86** (1979), no. 2 243 – 249.

[9] J. R. Ellis and I. Karliner, *Measuring the Spin of the Gluon in e+ e- Annihilation*, *Nucl. Phys.* **B148** (1979) 141–147.

[10] **TASSO** Collaboration, R. Brandelik *et. al.*, *Evidence for a Spin One Gluon in Three Jet Events*, *Phys. Lett.* **97B** (1980) 453–458.

[11] **Particle Data Group** Collaboration, K. A. Olive *et. al.*, *Review of Particle Physics*, *Chin. Phys.* **C38** (2014) 090001.

[12] P. Bagnaia *et al*, *Evidence for z0e+e at the cern pp collider*, *Physics Letters B* **129** (1983), no. 1 130 – 140.

[13] G. Arnison *et al*, *Experimental observation of lepton pairs of invariant mass around 95 gev/c2 at the cern sps collider*, *Physics Letters B* **126** (1983), no. 5 398 – 410.

[14] M. Banner *et al*, *Observation of single isolated electrons of high transverse momentum in events with missing transverse energy at the cern pp collider*, *Physics Letters B* **122** (1983), no. 5 476 – 485.

[15] G. Arnison *et al*, *Experimental observation of isolated large transverse energy electrons with associated missing energy at s=540 gev*, *Physics Letters B* **122** (1983), no. 1 103 – 116.

[16] **SLD Electroweak Group, DELPHI, ALEPH, SLD, SLD Heavy Flavour Group, OPAL, LEP Electroweak Working Group, L3**

Collaboration, S. Schael *et. al.*, *Precision electroweak measurements on the Z resonance*, *Phys. Rept.* **427** (2006) 257–454, [hep-ex/0509008].

[17] **ATLAS** Collaboration, G. Aad *et. al.*, *Observation of a new particle in the search for the Standard Model Higgs boson with the ATLAS detector at the LHC*, *Phys. Lett.* **B716** (2012) 1–29, [arXiv:1207.7214].

[18] **CMS** Collaboration, S. Chatrchyan *et. al.*, *Observation of a new boson at a mass of 125 GeV with the CMS experiment at the LHC*, *Phys. Lett.* **B716** (2012) 30–61, [arXiv:1207.7235].

[19] **Planck** Collaboration, P. A. R. Ade *et. al.*, *Planck 2015 results. XIII. Cosmological parameters*, *Astron. Astrophys.* **594** (2016) A13, [arXiv:1502.0158].

[20] V. C. Rubin, W. K. Ford, Jr., and N. Thonnard, *Rotational properties of 21 SC galaxies with a large range of luminosities and radii, from NGC 4605 /R = 4kpc/ to UGC 2885 /R = 122 kpc/*, *ApJ* **238** (June, 1980) 471–487.

[21] Y. Sofue and V. Rubin, *Rotation curves of spiral galaxies*, *Annual Review of Astronomy and Astrophysics* **39** (2001), no. 1 137–174, [https://doi.org/10.1146/annurev.astro.39.1.137].

[22] F. Zwicky, *On the Masses of Nebulae and of Clusters of Nebulae*, *ApJ* **86** (Oct., 1937) 217.

[23] A. B. Newman, T. Treu, R. S. Ellis, and D. J. Sand, *The Density Profiles of Massive, Relaxed Galaxy Clusters: II. Separating Luminous and Dark Matter in Cluster Cores*, *Astrophys. J.* **765** (2013) 25, [arXiv:1209.1392].

[24] D. Clowe, A. Gonzalez, and M. Markevitch, *Weak lensing mass reconstruction of the interacting cluster 1E0657-558: Direct evidence for the existence of dark matter*, *Astrophys. J.* **604** (2004) 596–603, [astro-ph/0312273].

[25] A. Refregier, *Weak gravitational lensing by large scale structure*, *Ann. Rev. Astron. Astrophys.* **41** (2003) 645–668, [astro-ph/0307212].

[26] G. Jungman, M. Kamionkowski, and K. Griest, *Supersymmetric dark matter*, *Phys. Rept.* **267** (1996) 195–373, [hep-ph/9506380].

[27] J. Preskill, M. B. Wise, and F. Wilczek, *Cosmology of the Invisible Axion*, *Phys. Lett.* **120B** (1983) 127–132.

[28] D. J. E. Marsh, *Axion Cosmology*, *Phys. Rept.* **643** (2016) 1–79, [arXiv:1510.0763].

[29] T. Marrodn Undagoitia and L. Rauch, *Dark matter direct-detection experiments*, *J. Phys.* **G43** (2016), no. 1 013001, [arXiv:1509.0876].

[30] J. M. Gaskins, *A review of indirect searches for particle dark matter*, *Contemp. Phys.* **57** (2016), no. 4 496–525, [arXiv:1604.0001].

[31] O. Buchmueller, C. Doglioni, and L. T. Wang, *Search for dark matter at colliders*, *Nature Phys.* **13** (2017), no. 3 217–223.

[32] M. Bauer, M. Neubert, and A. Thamm, *Collider Probes of Axion-Like Particles*, arXiv:1708.0044.

[33] **Supernova Cosmology Project** Collaboration, M. Kowalski *et. al.*, *Improved Cosmological Constraints from New, Old and Combined Supernova Datasets*, *Astrophys. J.* **686** (2008) 749–778, [arXiv:0804.4142].

[34] C. Vafa and E. Witten, *Parity conservation in quantum chromodynamics*, *Phys. Rev. Lett.* **53** (Aug, 1984) 535–536.

[35] R. D. Peccei and H. R. Quinn, *CP conservation in the presence of pseudoparticles*, *Physical Review Letters* **38** (June, 1977) 1440–1443.

[36] J. E. Kim, *Light pseudoscalars, particle physics and cosmology*, *Physics Reports* **150** (1987), no. 1 1 – 177.

[37] E. Witten, *Some Properties of O(32) Superstrings*, *Phys. Lett.* **149B** (1984) 351–356.

[38] P. Svrcek and E. Witten, *Axions In String Theory*, *JHEP* **06** (2006) 051, [hep-th/0605206].

[39] A. Arvanitaki, S. Dimopoulos, S. Dubovsky, N. Kaloper, and J. March-Russell, *String Axiverse*, *Phys. Rev.* **D81** (2010) 123530, [arXiv:0905.4720].

[40] T. Damour and J. F. Donoghue, *Equivalence Principle Violations and Couplings of a Light Dilaton*, *Phys. Rev.* **D82** (2010) 084033, [arXiv:1007.2792].

[41] G. Raffelt and L. Stodolsky, *Mixing of the Photon with Low Mass Particles*, *Phys. Rev.* **D37** (1988) 1237.

[42] C. Deffayet, D. Harari, J.-P. Uzan, and M. Zaldarriaga, *Dimming of supernovae by photon pseudoscalar conversion and the intergalactic plasma*, *Phys. Rev.* **D66** (2002) 043517, [hep-ph/0112118].

[43] A. G. Dias, A. C. B. Machado, C. C. Nishi, A. Ringwald, and P. Vaudrevange, *The Quest for an Intermediate-Scale Accidental Axion and Further ALPs*, *JHEP* **06** (2014) 037, [arXiv:1403.5760].

[44] A. Ayala, I. Domnguez, M. Giannotti, A. Mirizzi, and O. Straniero, *Revisiting the bound on axion-photon coupling from Globular Clusters*, *Phys. Rev. Lett.* **113** (2014), no. 19 191302, [arXiv:1406.6053].

[45] **CAST** Collaboration, M. Arik *et. al.*, *New solar axion search using the CERN Axion Solar Telescope with ^{4}He filling*, *Phys. Rev.* **D92** (2015), no. 2 021101, [arXiv:1503.0061].

[46] **OSQAR** Collaboration, R. Ballou *et. al.*, *New exclusion limits on scalar and pseudoscalar axionlike particles from light shining through a wall*, *Phys. Rev.* **D92** (2015), no. 9 092002, [arXiv:1506.0808].

[47] F. Della Valle, A. Ejlli, U. Gastaldi, G. Messineo, E. Milotti, R. Pengo, G. Ruoso, and G. Zavattini, *The PVLAS experiment: measuring vacuum magnetic birefringence and dichroism with a birefringent Fabry?Perot cavity*, *Eur. Phys. J.* **C76** (2016), no. 1 24, [arXiv:1510.0805].

[48] **ADMX** Collaboration, S. J. Asztalos *et. al.*, *An Improved RF cavity search for halo axions*, *Phys. Rev.* **D69** (2004) 011101, [astro-ph/0310042].

[49] D. Grin, G. Covone, J.-P. Kneib, M. Kamionkowski, A. Blain, and E. Jullo, *A Telescope Search for Decaying Relic Axions*, *Phys. Rev.* **D75** (2007) 105018, [astro-ph/0611502].

[50] M. T. Ressell, *Limits to the radiative decay of the axion*, *Phys. Rev.* **D44** (1991) 3001–3020.

[51] M. A. Bershady, M. T. Ressell, and M. S. Turner, *Telescope search for multi-eV axions*, *Phys. Rev. Lett.* **66** (1991) 1398–1401.

[52] J. W. Brockway, E. D. Carlson, and G. G. Raffelt, *SN1987A gamma-ray limits on the conversion of pseudoscalars*, *Phys. Lett.* **B383** (1996) 439–443, [astro-ph/9605197].

[53] J. A. Grifols, E. Masso, and R. Toldra, *Gamma-rays from SN1987A due to pseudoscalar conversion*, *Phys. Rev. Lett.* **77** (1996) 2372–2375, [astro-ph/9606028].

[54] A. Payez, C. Evoli, T. Fischer, M. Giannotti, A. Mirizzi, and A. Ringwald, *Revisiting the SN1987A gamma-ray limit on ultralight axion-like particles*, *JCAP* **1502** (2015), no. 02 006, [arXiv:1410.3747].

[55] **H.E.S.S.** Collaboration, P. Brun and D. Wouters, *Constraints on axion-like particles with H.E.S.S. from observations of PKS 2155-304*, in *Proceedings, 33rd International Cosmic Ray Conference (ICRC2013): Rio de Janeiro, Brazil, July 2-9, 2013*, p. 0949, 2013. arXiv:1307.6068.

[56] M. Meyer, D. Horns, and M. Raue, *First lower limits on the photon-axion-like particle coupling from very high energy gamma-ray observations*, *Phys. Rev.* **D87** (2013), no. 3 035027, [arXiv:1302.1208].

[57] M. Giannotti, I. Irastorza, J. Redondo, and A. Ringwald, *Cool WISPs for stellar cooling excesses*, *JCAP* **1605** (2016), no. 05 057, [arXiv:1512.0810].

[58] N. Banik, A. J. Christopherson, P. Sikivie, and E. M. Todarello, *New astrophysical bounds on ultralight axionlike particles*, *Phys. Rev.* **D95** (2017), no. 4 043542, [arXiv:1701.0457].

[59] A. Cavaliere and A. Lapi, *The Astrophysics of the Intracluster Plasma*, *Phys. Rept.* **533** (2013) 69–94, [arXiv:1308.6673].

[60] L. Feretti, G. Giovannini, F. Govoni, and M. Murgia, *Clusters of galaxies: observational properties of the diffuse radio emission*, *Astron. Astrophys. Rev.* **20** (2012) 54, [arXiv:1205.1919].

[61] A. C. Fabian, *Cluster cores and cooling flows*, astro-ph/0210150. [Rev. Mex. Astron. Astrof. Ser. Conf.17,303(2003)].

[62] R. Jansson and G. R. Farrar, *A New Model of the Galactic Magnetic Field*, *Astrophys. J.* **757** (2012) 14, [arXiv:1204.3662].

[63] R. Jansson and G. R. Farrar, *The Galactic Magnetic Field*, *Astrophys. J.* **761** (2012) L11, [arXiv:1210.7820].

[64] J. M. Cordes and T. J. W. Lazio, *NE2001. 2. Using radio propagation data to construct a model for the galactic distribution of free electrons*, astro-ph/0301598.

[65] C. Burrage, A.-C. Davis, and D. J. Shaw, *Active Galactic Nuclei Shed Light on Axion-like-Particles*, *Phys. Rev. Lett.* **102** (2009) 201101, [arXiv:0902.2320].

[66] J. P. Conlon and M. C. D. Marsh, *Excess Astrophysical Photons from a 0.1?1 keV Cosmic Axion Background*, *Phys. Rev. Lett.* **111** (2013), no. 15 151301, [arXiv:1305.3603].

[67] D. Wouters and P. Brun, *Constraints on Axion-like Particles from X-Ray Observations of the Hydra Galaxy Cluster*, *Astrophys. J.* **772** (2013) 44, [arXiv:1304.0989].

[68] S. Angus, J. P. Conlon, M. C. D. Marsh, A. J. Powell, and L. T. Witkowski, *Soft X-ray Excess in the Coma Cluster from a Cosmic Axion Background*, *JCAP* **1409** (2014), no. 09 026, [arXiv:1312.3947].

[69] J. P. Conlon, M. C. D. Marsh, and A. J. Powell, *Galaxy cluster thermal x-ray spectra constrain axionlike particles*, *Phys. Rev.* **D93** (2016), no. 12 123526, [arXiv:1509.0674].

[70] D. Wouters and P. Brun, *Irregularity in gamma ray source spectra as a signature of axionlike particles*, *Phys. Rev.* **D86** (2012) 043005, [arXiv:1205.6428].

[71] **Fermi-LAT** Collaboration, M. Ajello *et. al.*, *Search for Spectral Irregularities due to Photon?Axionlike-Particle Oscillations with the Fermi Large Area Telescope*, *Phys. Rev. Lett.* **116** (2016), no. 16 161101, [arXiv:1603.0697].

[72] M. C. D. Marsh, H. R. Russell, A. C. Fabian, B. P. McNamara, P. Nulsen, and C. S. Reynolds, *A New Bound on Axion-Like Particles*, arXiv:1703.0735.

[73] A. Bonafede, L. Feretti, M. Murgia, F. Govoni, G. Giovannini, D. Dallacasa, K. Dolag, and G. B. Taylor, *The Coma cluster magnetic field from Faraday rotation measures*, *Astron. Astrophys.* **513** (2010) A30, [arXiv:1002.0594].

[74] **Hitomi** Collaboration, F. A. Aharonian *et. al.*, *Hitomi constraints on the 3.5 keV line in the Perseus galaxy cluster*, *Astrophys. J.* **837** (2017), no. 1 L15, [arXiv:1607.0742].

[75] A. Fruscione, J. C. McDowell, G. E. Allen, N. S. Brickhouse, D. J. Burke, J. E. Davis, N. Durham, M. Elvis, E. C. Galle, D. E. Harris, D. P. Huenemoerder, J. C. Houck, B. Ishibashi, M. Karovska, F. Nicastro, M. S. Noble, M. A. Nowak, F. A. Primini, A. Siemiginowska, R. K. Smith, and M. Wise, *CIAO: Chandra's data analysis system*, in *Society of Photo-Optical Instrumentation Engineers (SPIE) Conference Series*, vol. 6270 of *Proc. SPIE*, p. 62701V, June, 2006.

[76] P. Freeman, S. Doe, and A. Siemiginowska, *Sherpa: a mission-independent data analysis application*, in *Astronomical Data Analysis* (J.-L. Starck and F. D. Murtagh, eds.), vol. 4477 of *Proc. SPIE*, pp. 76–87, Nov., 2001. astro-ph/0108426.

[77] G. B. Taylor, N. E. Gugliucci, A. C. Fabian, J. S. Sanders, G. Gentile, and S. W. Allen, *Magnetic fields in the center of the perseus cluster*, *Mon. Not. Roy. Astron. Soc.* **368** (2006) 1500–1506, [astro-ph/0602622].

[78] E. Churazov, W. Forman, C. Jones, and H. Bohringer, *Xmm-newton observations of the perseus cluster I: the temperature and surface brightness structure*, *Astrophys. J.* **590** (2003) 225–237, [astro-ph/0301482].

[79] V. Vacca, M. Murgia, F. Govoni, L. Feretti, G. Giovannini, R. A. Perley, and G. B. Taylor, *The intracluster magnetic field power spectrum in A2199*, *Astron. Astrophys.* **540** (2012) A38, [arXiv:1201.4119].

[80] T. A. Ensslin, P. L. Biermann, U. Klein, and S. Kohle, *Cluster radio relics as a tracer of shock waves of the large - scale structure formation*, *Astron. Astrophys.* **332** (1998) 395, [astro-ph/9712293].

[81] H. V. Klapdor-Kleingrothaus and I. V. Krivosheina, eds., *Dark Matter in Astrophysics and Particle Physics - Proceedings of the 7th International Heidelberg Conference on Dark 2009*, 2010.

[82] J. P. Ge and F. N. Owen, *Faraday rotation in cooling flow clusters of galaxies. I - Radio and X-ray observations of Abell 1795*, *AJ* **105** (Mar., 1993) 778–787.

[83] S. Ettori, *Beta-model and cooling flows in x-ray clusters of galaxies*, *Mon. Not. Roy. Astron. Soc.* **318** (2000) 1041, [astro-ph/0005224].

[84] T. J. Dennis and B. D. G. Chandran, *Turbulent Heating of Galaxy-Cluster Plasmas*, *ApJ* **622** (Mar., 2005) 205–216.

[85] E. Armengaud *et. al.*, *Conceptual Design of the International Axion Observatory (IAXO)*, *JINST* **9** (2014) T05002, [arXiv:1401.3233].

[86] J. P. Conlon and M. C. D. Marsh, *The Cosmophenomenology of Axionic Dark Radiation*, *JHEP* **10** (2013) 214, [arXiv:1304.1804].

[87] D. Kraljic, M. Rummel, and J. P. Conlon, *ALP Conversion and the Soft X-ray Excess in the Outskirts of the Coma Cluster*, *JCAP* **1501** (2015), no. 01 011, [arXiv:1406.5188].

[88] A. J. Powell, *A Cosmic ALP Background and the Cluster Soft X-ray Excess in A665, A2199 and A2255*, *JCAP* **1509** (2015), no. 09 017, [arXiv:1411.4172].

[89] M. Simet, D. Hooper, and P. D. Serpico, *The Milky Way as a Kiloparsec-Scale Axionscope*, *Phys. Rev.* **D77** (2008) 063001, [arXiv:0712.2825].

[90] D. Horns, L. Maccione, M. Meyer, A. Mirizzi, D. Montanino, and M. Roncadelli, *Hardening of TeV gamma spectrum of AGNs in galaxy clusters by conversions of photons into axion-like particles*, *Phys. Rev.* **D86** (2012) 075024, [arXiv:1207.0776].

[91] D. Wouters and P. Brun, *Anisotropy test of the axion-like particle Universe opacity effect: a case for the Cherenkov Telescope Array*, *JCAP* **1401** (2014) 016, [arXiv:1309.6752].

[92] M. Fairbairn, *Axionic Dark Radiation and the Milky Way's Magnetic Field*, *Phys. Rev.* **D89** (2014), no. 6 064020, [arXiv:1310.4464].

[93] R. C. Hickox and M. Markevitch, *Resolving the unresolved cosmic X-ray background in the Chandra Deep Fields*, *Astrophys. J.* **661** (2007) L117–L121, [astro-ph/0702556].

[94] D. B. Henley and R. L. Shelton, *An XMM-Newton Survey of the Soft X-ray Background. III. The Galactic Halo X-ray Emission*, *Astrophys. J.* **773** (2013) 92, [arXiv:1306.2312].

[95] R. Beck, *Magnetic Fields in Galaxies*, *Space Science Rev.* **166** (May, 2012) 215–230.

[96] M. C. Beck, A. M. Beck, R. Beck, K. Dolag, A. W. Strong, and P. Nielaba, *New constraints on modelling the random magnetic field of the MW*, *JCAP* **1605** (2016), no. 05 056, [arXiv:1409.5120].

[97] R. Morrison and D. McCammon, *Interstellar photoelectric absorption cross sections, 0.03-10 keV*, *ApJ* **270** (July, 1983) 119–122.

[98] A. Misiriotis, E. M. Xilouris, J. Papamastorakis, P. Boumis, and C. D. Goudis, *The distribution of the ISM in the Milky Way A three-dimensional large-scale model*, *Astron. Astrophys.* **459** (2006) 113, [astro-ph/0607638].

[99] S. L. Snowden, M. J. Freyberg, P. P. Plucinsky, J. H. M. M. Schmitt, J. Truemper, W. Voges, R. J. Edgar, D. McCammon, and W. T. Sanders, *First Maps of the Soft X-Ray Diffuse Background from the ROSAT XRT/PSPC All-Sky Survey*, *ApJ* **454** (Dec., 1995) 643.

[100] E. M. Berkhuijsen, D. Mitra, and P. Mueller, *Filling factors and scale heights of the dig in the milky way*, *Astron. Nachr.* **327** (2006) 82, [astro-ph/0511172].

[101] B. Adebahr, M. Krause, U. Klein, M. Wezgowiec, D. J. Bomans, and R. J. Dettmar, *M82 - A radio continuum and polarisation study I. Data reduction and cosmic ray propagation*, *Astron. Astrophys.* **555** (2013) A23, [arXiv:1209.5552].

[102] M. S. Westmoquette, J. S. Gallagher, L. J. Smith, G. Trancho, N. Bastian, and I. S. Konstantopoulos, *The Optical Structure of the Starburst Galaxy M82. II. Nebular Properties of the Disk and Inner-Wind*, *Astrophys. J.* **706** (2009) 1571–1587, [arXiv:0907.3162].

[103] E. Bulbul, M. Markevitch, A. Foster, R. K. Smith, M. Loewenstein, and S. W. Randall, *Detection of An Unidentified Emission Line in the Stacked X-ray spectrum of Galaxy Clusters*, *Astrophys. J.* **789** (2014) 13, [arXiv:1402.2301].

[104] A. R. Foster, L. Ji, R. K. Smith, and N. S. Brickhouse, *Updated Atomic Data and Calculations for X-ray Spectroscopy*, *Astrophys. J.* **756** (2012) 128, [arXiv:1207.0576].

[105] A. Boyarsky, O. Ruchayskiy, D. Iakubovskyi, and J. Franse, *Unidentified Line in X-Ray Spectra of the Andromeda Galaxy and Perseus Galaxy Cluster*, *Phys. Rev. Lett.* **113** (2014) 251301, [arXiv:1402.4119].

[106] T. E. Jeltema and S. Profumo, *Discovery of a 3.5 keV line in the Galactic Centre and a critical look at the origin of the line across astronomical targets*, *Mon. Not. Roy. Astron. Soc.* **450** (2015), no. 2 2143–2152, [arXiv:1408.1699].

[107] A. Boyarsky, J. Franse, D. Iakubovskyi, and O. Ruchayskiy, *Checking the Dark Matter Origin of a 3.53 keV Line with the Milky Way Center*, *Phys. Rev. Lett.* **115** (2015) 161301, [arXiv:1408.2503].

[108] S. Riemer-Srensen, *Constraints on the presence of a 3.5 keV dark matter emission line from Chandra observations of the Galactic centre*, *Astron. Astrophys.* **590** (2016) A71, [arXiv:1405.7943].

[109] E. Carlson, T. Jeltema, and S. Profumo, *Where do the 3.5 keV photons come from? A morphological study of the Galactic Center and of Perseus*, *JCAP* **1502** (2015), no. 02 009, [arXiv:1411.1758].

[110] J. Franse *et. al.*, *Radial Profile of the 3.55 keV line out to R_{200} in the Perseus Cluster*, *Astrophys. J.* **829** (2016), no. 2 124, [arXiv:1604.0175].

[111] D. Malyshev, A. Neronov, and D. Eckert, *Constraints on 3.55 keV line emission from stacked observations of dwarf spheroidal galaxies*, *Phys. Rev.* **D90** (2014) 103506, [arXiv:1408.3531].

[112] T. E. Jeltema and S. Profumo, *Deep XMM Observations of Draco rule out at the 99% Confidence Level a Dark Matter Decay Origin for the 3.5 keV Line*, *Mon. Not. Roy. Astron. Soc.* **458** (2016), no. 4 3592–3596, [arXiv:1512.0123].

[113] O. Ruchayskiy, A. Boyarsky, D. Iakubovskyi, E. Bulbul, D. Eckert, J. Franse, D. Malyshev, M. Markevitch, A. Neronov, and I. Dmytro, *Searching for decaying dark matter in deep XMM?Newton observation of the Draco dwarf spheroidal*, *Mon. Not. Roy. Astron. Soc.* **460** (2016), no. 2 1390–1398, [arXiv:1512.0721].

[114] M. E. Anderson, E. Churazov, and J. N. Bregman, *Non-Detection of X-Ray Emission From Sterile Neutrinos in Stacked Galaxy Spectra*, *Mon. Not. Roy. Astron. Soc.* **452** (2015), no. 4 3905–3923, [arXiv:1408.4115].

[115] D. Iakubovskyi, *New emission line at 3.5 keV - observational status, connection with radiatively decaying dark matter and directions for future studies*, arXiv:1410.2852.

[116] D. Iakubovskyi, E. Bulbul, A. R. Foster, D. Savchenko, and V. Sadova, *Testing the origin of 3.55 keV line in individual galaxy clusters observed with XMM-Newton*, arXiv:1508.0518.

[117] O. Urban, N. Werner, S. W. Allen, A. Simionescu, J. S. Kaastra, and L. E. Strigari, *A Suzaku Search for Dark Matter Emission Lines in the X-ray Brightest Galaxy Clusters*, *Mon. Not. Roy. Astron. Soc.* **451** (2015), no. 3 2447–2461, [arXiv:1411.0050].

[118] E. Bulbul, M. Markevitch, A. Foster, E. Miller, M. Bautz, M. Loewenstein, S. W. Randall, and R. K. Smith, *Searching for the 3.5 keV Line in the Stacked Suzaku Observations of Galaxy Clusters*, *Astrophys. J.* **831** (2016), no. 1 55, [arXiv:1605.0203].

[119] F. Hofmann, J. S. Sanders, K. Nandra, N. Clerc, and M. Gaspari, *7.1 keV sterile neutrino constraints from X-ray observations of 33 clusters of galaxies with Chandra ACIS*, *Astron. Astrophys.* **592** (2016) A112, [arXiv:1606.0409].

[120] T. Tamura, R. Iizuka, Y. Maeda, K. Mitsuda, and N. Y. Yamasaki, *An X-ray Spectroscopic Search for Dark Matter in the Perseus Cluster with Suzaku*, *Publ. Astron. Soc. Jap.* **67** (2015) 23, [arXiv:1412.1869].

[121] N. Sekiya, N. Y. Yamasaki, and K. Mitsuda, *A Search for a keV Signature of Radiatively Decaying Dark Matter with Suzaku XIS Observations of the X-ray Diffuse Background*, *Publ. Astron. Soc. Jap.* (2015) [arXiv:1504.0282].

[122] A. Neronov, D. Malyshev, and D. Eckert, *Decaying dark matter search with NuSTAR deep sky observations*, *Phys. Rev.* **D94** (2016), no. 12 123504, [arXiv:1607.0732].

[123] D. R. Wik *et. al.*, *NuSTAR Observations of the Bullet Cluster: Constraints on Inverse Compton Emission*, *Astrophys. J.* **792** (2014), no. 1 48, [arXiv:1403.2722].

[124] N. Cappelluti, E. Bulbul, A. Foster, P. Natarajan, M. C. Urry, M. W. Bautz, F. Civano, E. Miller, and R. K. Smith, *Searching for the 3.5 keV Line in the Deep Fields with Chandra: the 10 Ms observations*, arXiv:1701.0793.

[125] E. Bulbul, M. Markevitch, A. R. Foster, R. K. Smith, M. Loewenstein, and S. W. Randall, *Comment on "Dark matter searches going bananas: the*

contribution of Potassium (and Chlorine) to the 3.5 keV line", arXiv:1409.4143.

[126] K. J. H. Phillips, B. Sylwester, and J. Sylwester, *THE X-RAY LINE FEATURE AT 3.5 KeV IN GALAXY CLUSTER SPECTRA*, *Astrophys. J.* **809** (2015) 50.

[127] L. Gu, J. Kaastra, A. J. J. Raassen, P. D. Mullen, R. S. Cumbee, D. Lyons, and P. C. Stancil, *A novel scenario for the possible X-ray line feature at 3.5 keV: Charge exchange with bare sulfur ions*, *Astron. Astrophys.* **584** (2015) L11, [arXiv:1511.0655].

[128] C. Shah, S. Dobrodey, S. Bernitt, R. Steinbrgge, J. R. C. Lpez-Urrutia, L. Gu, and J. Kaastra, *Laboratory measurements compellingly support charge-exchange mechanism for the 'dark matter' ∼3.5 keV X-ray line*, *Astrophys. J.* **833** (2016), no. 1 52, [arXiv:1608.0475].

[129] A. Boyarsky, J. Franse, D. Iakubovskyi, and O. Ruchayskiy, *Comment on the paper "Dark matter searches going bananas: the contribution of Potassium (and Chlorine) to the 3.5 keV line" by T. Jeltema and S. Profumo*, arXiv:1408.4388.

[130] M. Cicoli, J. P. Conlon, M. C. D. Marsh, and M. Rummel, *3.55 keV photon line and its morphology from a 3.55 keV axionlike particle line*, *Phys. Rev.* **D90** (2014) 023540, [arXiv:1403.2370].

[131] M. Cicoli, J. P. Conlon, and F. Quevedo, *General Analysis of LARGE Volume Scenarios with String Loop Moduli Stabilisation*, *JHEP* **10** (2008) 105, [arXiv:0805.1029].

[132] **Fermi-LAT** Collaboration, M. Ackermann *et. al.*, *Search for Gamma-ray Spectral Lines with the Fermi Large Area Telescope and Dark Matter Implications*, *Phys. Rev.* **D88** (2013) 082002, [arXiv:1305.5597].

[133] J. F. Navarro, C. S. Frenk, and S. D. M. White, *The Structure of cold dark matter halos*, *Astrophys. J.* **462** (1996) 563–575, [astro-ph/9508025].

[134] G. C. Gomez, R. A. Benjamin, D. P. Cox, and P. Donald, *A re-examination of the distribution of galactic free electrons*, *Astron. J.* **122** (2001) 908, [astro-ph/0105416].

[135] R. L. Brown and R. J. Gould, *Interstellar Absorption of Cosmic X Rays*, *Phys.Rev.* **D1** (1970) 2252–2256.

[136] J. L. Han, R. Beck, and E. M. Berkhuijsen, *New clues to the magnetic field structure of m31*, *Astron. Astrophys.* **335** (1998) 1117, [astro-ph/9805023].

[137] A. Fletcher, E. M. Berkhuijsen, R. Beck, and A. Shukurov, *The Magnetic field of M 31 from multi-wavelength radio polarization observations*, *Astron. Astrophys.* **414** (2004) 53–67, [astro-ph/0310258].

[138] A. E. Egorov and E. Pierpaoli, *Constraints on dark matter annihilation by radio observations of M31*, *Phys. Rev.* **D88** (2013), no. 2 023504, [arXiv:1304.0517].

[139] R. Giebel, G. Heald, and R. Beck, *Polarized synchrotron radiation from the Andromeda Galaxy M31 and background sources at 350 MHz*, *Astron. Astrophys.* **559** (2013) A27, [arXiv:1309.2539].

[140] J. J. Geehan, M. A. Fardal, A. Babul, and P. Guhathakurta, *Investigating the Andromeda Stream. 1. Simple analytic bulge-disk-halo model for M31*, *Mon. Not. Roy. Astron. Soc.* **366** (2006) 996–1011, [astro-ph/0501240].

[141] **Hitomi** Collaboration, F. Aharonian *et. al.*, *The Quiescent Intracluster Medium in the Core of the Perseus Cluster*, *Nature* **535** (2016) 117–121, [arXiv:1607.0448].

[142] A. C. Fabian, S. A. Walker, C. Pinto, H. R. Russell, and A. C. Edge, *Effects of the variability of the nucleus of NGC 1275 on X-ray observations of the surrounding intracluster medium*, *Mon. Not. Roy. Astron. Soc.* **451** (2015), no. 3 3061–3067, [arXiv:1505.0375].

[143] S. Profumo and K. Sigurdson, *The Shadow of Dark Matter*, *Phys. Rev.* **D75** (2007) 023521, [astro-ph/0611129].

[144] M. A. Sanchez-Conde, M. Cannoni, F. Zandanel, M. E. Gomez, and F. Prada, *Dark matter searches with Cherenkov telescopes: nearby dwarf galaxies or local galaxy clusters?*, *JCAP* **1112** (2011) 011, [arXiv:1104.3530].

[145] F. D'Eramo, K. Hambleton, S. Profumo, and T. Stefaniak, *Dark matter inelastic up-scattering with the interstellar plasma: A new source of x-ray lines, including at 3.5 keV*, *Phys. Rev.* **D93** (2016), no. 10 103011, [arXiv:1603.0485].